NMR imaging of curing processes in alkyd coatings

Please check the document version of this publication:

• A submitted manuscript is the version of the article upon submission and before peer-review. There can be important differences between the submitted version and the official published version of record. People interested in the research are advised to contact the author for the final version of the publication, or visit the DOI to the publisher's website.
• The final author version and the galley proof are versions of the publication after peer review.
• The final published version features the final layout of the paper including the volume, issue and page numbers.
Link to publication

NMR imaging of curing processes in alkyd coatings

Sebastiaan Joannes Franciscus Erich

NMR imaging of curing processes in alkyd coatings

PROEFSCHRIFT

ter verkrijging van de graad van doctor aan de
Technische Universiteit Eindhoven, op gezag van
de Rector Magnificus, prof.dr.ir. C.J. van Duijn,
voor een commissie aangewezen door het College
voor Promoties in het openbaar te verdedigen op
woensdag 24 mei 2006 om 16.00 uur

door

Sebastiaan Joannes Franciscus Erich

geboren te Best

Dit proefschrift is goedgekeurd door de promotoren:

prof.dr.ir. K. Kopinga
en
prof.dr. G. de With

Copromotor:
dr.ir. L. Pel

Contents

1. Introduction

Nothing is as dull as watching paint dry
English saying

1.1 History

Paints appeared about approximately 30,000 years ago. Cave dwellers used crude paints to make images of their daily lives, showing pictures of animals and pictures of them hunting animals. The oldest known cave painting is that of Chauvet near Vallon-Pont-d'Arcin in southern France. It is about 32,000 years old and was discovered in 1994. Other cave paintings are found in Lascaux, France and Altamira, Spain. The paintings were drawn in black red, and yellow, created by various pigments available from their natural habitat, such as iron oxides, manganese oxides, chalk, and charcoal.

The Egyptians (3000 to 600 BC) were one of the first to further develop paint. Although many of the pigments they used were also available from their natural surroundings, they were the first to develop a synthetic pigment. This pigment is known today as Egyptian Blue ($CaCuSi_4O_{10}$) and was produced from a calcium compound (carbonate (chalk), sulfate or hydroxide), a copper compound (oxide or malachite) and quartz or silica. The Egyptians used two types of paints; encaustic paint and tempera. Encaustic paint, also called "hot wax painting", involves heated beeswax to which colored pigments were added. Tempera (or egg tempera) is a paint made by binding pigments in an egg medium.

The Greeks and Romans (600 BC – 400 AD) understood that paint could not only be used to decorate objects but also to preserve objects. Varnishes based on drying oils were introduced. The varnish was made by combining natural resins with drying oils, such as, linseed, hempseed, or walnut oil. It was not until the middle ages (about 400 – 1500) that the protective value of drying oils was recognized in Europe.

Since the Renaissance (about 1400 – 1600), siccative (drying) oil paints, primarily linseed oil, have been the most commonly used paint in fine art applications. Oil paint is still commonly used today for works of art.

The Industrial Revolution (about 1700 – 1900) had a major effect on the development of the paint industry. The amount of iron and steel used for construction purposes increased and had to be protected. Lead- and zinc-based paints were developed by dispersing these metals in linseed oil. These developments required an increasing amount of paint factories. These paint factories remained decentralized, because the weight of prepared paint made transportation too expensive. During and after the industrial revolution the newly developed industrial products required paints or coatings, thereby increasing

1
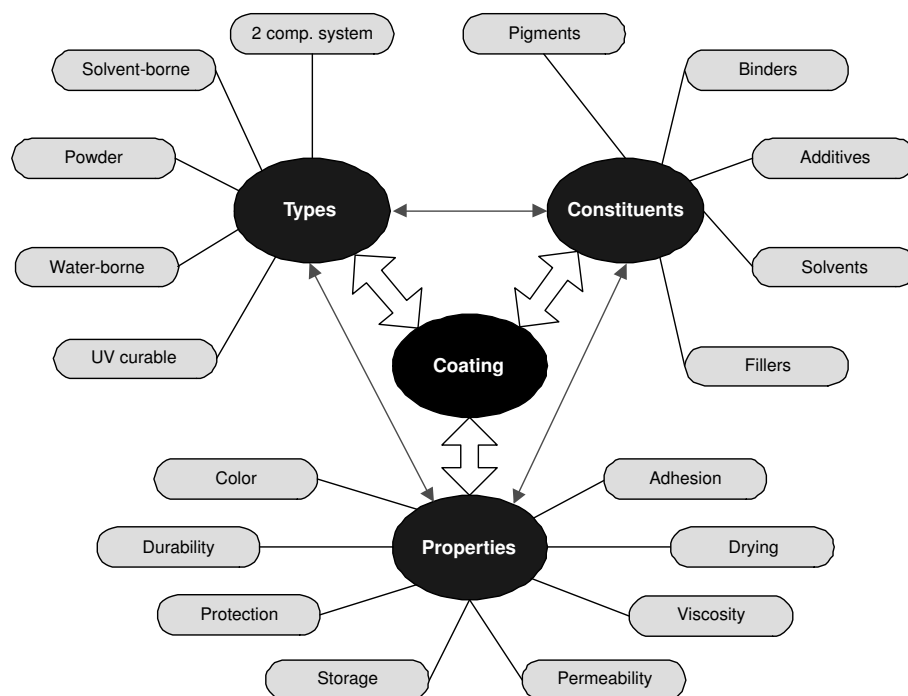
Fig. 1.1: Overview of the relations between the types, properties and constituents of coatings. The arrows indicate the many relations that exists, for example selecting a specific type has consequences for both the coating constituents and coating properties.

the paint market.

Around 1920 the paint industry was confronted with an environmental issue. Lead-based paint, containing high amounts of lead as a whitening pigment ($2PbCO_3 \cdot Pb(OH)_2$), had become widely used and appeared to be toxic. After the toxicity of lead became clear, the amount of lead used started to diminish and around 1970 was totally replaced by titanium dioxide, that became available as an affordable alternative pigment. However, still lead remained to be used as a drier (catalyst) in low concentrations. Today lead driers are almost completely replaced in all paints [1, 2].

Nowadays paints and coatings can be found everywhere, e.g. on building materials, on cars, aircrafts, solar cells, plastics, steel and wires. The purpose of these coatings differs, e.g. for protection against the environment and/or for esthetic reasons. Many materials require protection against environmental attacks, such as UV-radiation, heat, moisture, chemicals, and acid rain. Different types of coatings exists for each specific application, and are illustrated in figure 1.1. These types are water-borne, solvent-borne, powder, 2-component, and UV-curable coatings. Each of these types has its specific constituents and properties, which are all inter related. This makes the coating industry a broad, complex and a challenging field. Water-borne coatings were the largest in volume around 1994 and this volume was expected to grow considerably [3].

Western Europe produces about 5 million tonnes of coatings per year, which accounts for approximately 22% of the world production. In 1996 the European coating industry consumed 1.8 million tonnes of binders for the production of paints, of which 25% were
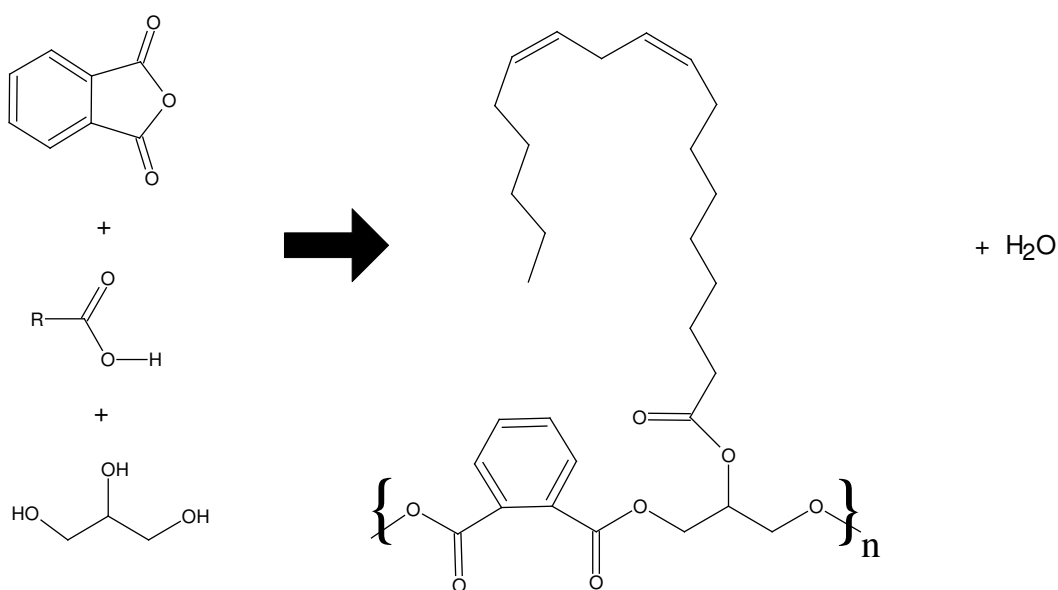
Fig. 1.2: Typical example of an alkyd resin polymerized from phthalic anhydride, fatty acid (RCOOH), and glycerol.

alkyds. In 2002 alkyd resins accounted for 26.2% of the total use in Europe. About 90,000 tonnes of additives were used by the European paint industries in the same period. Of these approximately 26,000 tonnes (28.5%) were driers and 6,300 tonnes (7.1%) anti-skinning agents. The consumed amounts of driers and anti-skinning agents within the coating industry are directly related to the produced amount of air-drying coating system. World wide the total paint and coatings industry is over the 50 billion euro's, and the European market is over 13 billion euro [1, 3, 4].

The focus in this thesis will be on alkyd resins, being one of the very widely used types. Alkyd resins are based on polymeric resins developed in the 1920's [5] and first produced commercially by General Electric. The term "alkyd" originally comes from "al", referring to alcohol, and "kyd", refereing to acid. Nowadays, the term alkyd refers to polyesters modified with fatty acids. Alkyds are prepared via condensation polymerization of three types of monomers: polyalcohols, polybasic acids, and fatty acids or triglyceride oils to obtain fatty-acid containing polyesters [3]. A simple example is given in figure 1.2. The double bonds present in the fatty acid side chains of the alkyd molecules will cross-link using oxygen from the air to form the final rigid coating. Variations in the amounts and types of components give the resin and thus the final coating different properties. Alkyd resins are frequently classified by the oil type and oil length. The latter is defined as the weight percent of oil present in the resin. If the oil content is less than about 45% it is defined as a short oil, between 45% and 60% as a medium oil, or when greater than 60% as a long oil. This oil length changes the average distance between cross-links points of the polymer, and thereby the properties of the coating, such as hardness and permeability.

1.2   Developments in coatings technology

The general knowledge about coatings has increased considerably over the years and, additionally, one slowly became aware of the environmental risks of several coating ingredients. Not only the constituents affect the environment or health, but also the acquisition of the raw materials damages the environment. Therefore renewable resources as raw materials for the coating, like plant oils, have gained interest. The European community and the local governments force coating manufactures to produce less environmental demanding coatings by legislation. The most important environmental issues and legislatorial changes that had or will have a major impact on the coating industry are discussed below.

One development is the strict legislation concerning the emission and usage of volatile organic components (VOC). Not only the environment is affected by these VOC's, but long term exposure to these chemicals leads to the so called Psycho-Organic Syndrome (POS). The effects of solvents on the health was extensively researched and clear effects were established [6–12]. Since January 2000 the Dutch government has changed the legislation concerning the use of VOC's, forcing professional painters to use products with low amount of VOC's ($<$ 125 g VOC's per liter of product) for indoor application [13, 14]. The change in legislation has driven coating manufactures to look for alternatives or alternative solutions, such as changing to other types of coatings (see also figure 1.1). New technical developments have resulted in an increase of the production of more water-borne coatings (for indoor applications) and high solids coating (for outdoor applications). Obviously, the market demands that the properties of these reformulated coatings should at least meet or should be better than their predecessors. Although water-borne systems have already been improved considerably, they still suffer from a variety of shortcomings, such as faster biological degradation, less water repellency, longer open times, and high surface tension, resulting in bad flow and in low gloss. Water-borne coatings also have several advantages, next to a reduced amount of VOC's, such as less fire hazard and the fact that existing equipment can still be used.

Another recent development that will have a major impact on the coating industry is the European Commission's (EC) White Paper for a new Chemical Strategy. This White Paper published in 2001, has led to a proposal concerning the Registration, Evaluation and Authorization of CHemicals (REACH) [15]. It is now expected that REACH will be approved by the European Parliament and Council this year and will enter into force in the spring of 2007. The central element is a completely new system of registration, evaluation, and authorisation/restriction for new and existing chemical substances marketed in quantities of more than 1 tonne per enterprize per year. This new system will have a major impact on the coating industry, by increasing the cost of registration, and research and development to find suitable alternatives when required.

In addition, recent studies have shown that cobalt, commonly used as a catalyst in (water-borne) alkyd coatings, is potentially carcinogenic [16–18]. In Germany coatings containing cobalt catalysts no longer hold the blue angel label, which is an eco-label. Hence, there is a tendency to replace this traditional catalyst by more environmental friendly ones in the near future [19].

Summarizing, the coating industry is a dynamic industry striving for environmental

friendly coatings, while increasing the performance and durability of the products and additionally decreasing the development time and costs. This process will benefit from a deeper understanding of the relation between composition, structure, and properties of a coating. Especially knowledge of the spatial and temporal evolution of the coating structure in time will be of great value [20, 21].

1.3   NMR imaging as a potential coating research tool

However, the problem of most standard testing equipment for coatings is that no information (both chemical or physical) as a function of depth can be obtained. For different types of coatings it is known that inhomogeneities exist and that these play an important role. For instance, in UV-curable systems inhomogeneities, are present that are induced by oxygen inhibitions [22] or UV-light absorption [23, 24]. For alkyds systems it is known that skin-layers are formed, which sometimes result in wrinkling [25].

Fortunately, during the last decade new measurement techniques have become available with the ability to obtain detailed spatially resolved information of the coating structure. One technique to probe the drying process of coatings as a function of depth is Confocal Raman Microscopy (CRM), which allows chemical changes to be followed with a resolution of about 5 μm [26]. However, this technique can only be used for optically transparent coatings.

Recently a new NMR setup has been developed that can probe the structure of a coating with a spatial resolution of approximately 5 μm as a function of depth [27]. Additionally, this setup can follow a drying process of a typical coating (200 μm) with a temporal resolution of approximately 10 min. The first development towards higher resolutions NMR imaging was stray field imaging [28], in which the magnetic field gradient just outside the bore of a superconducting magnet is used to achieve a high spatial resolution or to probe small-scale displacements (e.g. diffusion). Another is the development of a single-sided NMR setup, the so-called NMR MOUSE (Mobile Universal Surface Explorer) [29]. This has finally lead to the Gradient-At-Right-angles-to-Field (GARField) design [27], which combines a high gradient with single-sided NMR.

1.4   Aim of this thesis

The goal of the research reported in this thesis is to explore the curing (chemical drying) process inside alkyd coatings using a high spatial resolution NMR setup, based on the GARField design [27]. The outline of this thesis is as follows. A brief discussion of the drying processes of alkyd coatings is presented in chapter 2, and the research tools used in the subsequent chapters are introduced. In chapter 3 the design of the NMR setup will be considered in detail. In chapter 4 the drying of two typical alkyd coatings (a solvent-borne and a water-borne) is investigated by comparing the results of NMR and Confocal Raman Microscopy (CRM) experiments. This study allowed to relate chemical changes observed with CRM to the changes in signal decay observed with NMR. In chapter 5 we will discuss the role of oxygen in the curing process of alkyd coatings with cobalt as a

drier. A model was developed to describe the observed curing behavior. In chapter 6 the effect of so-called secondary driers on the curing behavior is investigated. Furthermore, the curing behavior in the deeper layers of the coating is investigated and modelled. The secondary driers used are Ca and Zr, next to Co as the primary drier. Manganese based alternatives for cobalt are investigated in chapter 7. The models presented in the previous two chapters no longer apply when the curing of manganese is investigated. So these results are interpreted using simulations based on a reaction-diffusion model. In chapter 8 the effect of the substrate on the curing of alkyd coatings is investigated, which is very relevant for the product performance in daily practice. In chapter 9 some general conclusions based on the results reported in the previous chapters are presented. Finally, an outlook is given, in which possible applications of the NMR setup for future coating research will be considered.

2. Alkyd coatings, drying and characterization

Life is a great big canvas, throw all the paint on it you can.
Danny Kaye, US actor and singer (1913 - 1987)

2.1   Drying of alkyd coatings

The drying process of an alkyd coating can be divided into two stages. The first stage is a physical drying stage in which the solvent evaporates. The second stage is a curing stage (chemical drying or oxidative drying) in which the resin of the coating reacts and forms a network by the formation of cross-links. These two stages involve different time scales: The evaporation stage takes minutes up to several hours, whereas the curing process takes place over several hours up to days, or even months. In fact the last stage can continue for years, which is often called aging. During this chemical aging the coating or painting finally becomes brittle and cracks appear, which can be observed in many historic oil based paintings on display in museums [30]. This aging process is beyond the scope of this thesis and we will mainly focus on the initial part of the curing process.

The evaporation stage has been studied extensively. During this stage the solvent evaporates while the resin remains behind. The speed of this process is very important in daily practice. The film should dry fast enough, but not too fast. The time characterizing this process is often referred to as open time. The open time is the time during which the coating layer flows enough to remove small irregularities. The evaporation process, together with the deformation of the particles in water-borne systems, determines the gloss and flow of the coating, making it an important topic for research. For water-borne systems the interactions between the emulsified droplets and their deformation were studied by Visschers et al. [31, 32, 33]. Using a high spatial resolution NMR setup the evaporation stage of coatings was studied [34–36]. Also the lateral drying of thin coating layers was studied using magnetic resonance imaging [37, 38].

During the curing (chemical drying) stage the double bonds of the fatty acid side chains present in the alkyd molecules (see Fig. 1.2) react with oxygen, which results in cross-links. This curing process is a complex oxidative process, which will be explained in more detail in section 2.2. The research on oxidative drying of alkyds can be subdivided in two research topics. The first topic concerns the chemical reactions taking place during oxidation of model systems. These model system are mostly oils or fatty acid esters, which still have a low viscosity after oxidation. The second research topic focusses on the curing process inside alkyd coatings films monitored as a function of depth. Not much research is performed on this topic, because the number of analytical techniques to probe the coating structure as a function of depth is limited. Compared to model systems
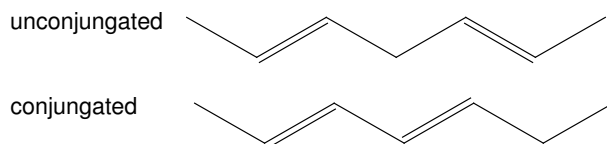
Fig. 2.1: Two possible configurations of double bonds in the fatty acid side chains of the alkyd
resin.

the curing of alkyd coating films is more complex, because physical aspects like diffusion
of oxygen or diffusion of radicals play a significant role. The fact that oxygen diffusion
plays an important role was already mentioned in 1954 [39]. Oxygen diffusion might
limit the curing reaction, which requires oxygen, resulting in an oxygen gradient. Such a
limitation of the curing reaction is demonstrated by the many examples of inhomogeneous
curing, e.g., the formation of a skin-layer at the surface of the coating which can cause
wrinkling [25]. Until recently little or no research was performed on the diffusion and
reaction as a function of depth inside alkyd coatings. Only recently the depletion of
double bonds inside alkyd coatings was followed using CRM and described in terms of a
reaction-diffusion model [40, 41].

2.2 Alkyd resins

2.2.1 Autoxidation

The curing of alkyds is an autoxidation process, in which oxygen reacts with unsaturated
oils or the unsaturated fatty acid side chains of alkyd resins. This process has been stud-
ied in great detail, as it is an important process in food science and biology. In case
of alkyd coatings the autoxidation process is necessary to form a cross-linked network.
The autoxidation mechanism of fatty acids is a complex process, in which many inter-
mediate species can be formed. For alkyd resins and model systems the autoxidation
process was studied extensively [42–50]. The model systems used in that research vary in
the amount of double bonds and have two configurations of double bonds, conjugated
and unconjugated, see figure 2.1. The configuration of the double bonds influences the
preferential cross-linking path [48, 51]. The autoxidation process is generally divided in
6 stages [39, 52–54]. The stages are:

- Induction

- Initiation

- Hydroperoxide formation

- Hydroperoxide decomposition

- Cross-linking

- Degradation or side-reactions

Induction

The induction period exists because of to the presence of natural anti-oxidants (α-, δ- tocopherols and β-carotene) or added anti-oxidants inside the coating. These anti-oxidants trap radicals, thereby inhibiting the oxidative reactions [55]. Oxidation reactions are also inhibited via quenching of singlet oxygen to the triplet state by carotenoids, e.g. β-carotene [56, 57]. In this triplet state direct addition of oxygen to the double bonds is spin-forbidden.

Initiation

This step is the least understood step of the autoxidation process. A certain free radical (X·) for initiation of the oxidation reaction is required. After H-atom abstraction from the unsaturated fatty acid (R-H) a radical R· remains. The energetically most favorable position of hydrogen abstraction in case of unconjungated double bonds (Fig. 2.1) is one of the two hydrogens positioned between the double bonds [58]. These radicals are the radicals that can be inhibited during the induction period. The hydrogen abstraction speeds up when a radical generating species is added.

$$\text{R-H} + \text{X·} \rightarrow \text{R·} + \text{X-H} \tag{2.1}$$

Hydroperoxide formation

The radical (R·) reacts instantaneously with oxygen to form a hydroperoxide radical. By abstracting another H-atom from the unsaturated fatty acid it forms a hydroperoxide.

$$\text{R} + \text{O}_2\text{·} \rightarrow \text{R-O-O·} \tag{2.2}$$
$$\text{R-O-O·} + \text{R-H} \rightarrow \text{R·} + \text{R-O-O-H} \tag{2.3}$$
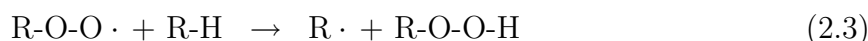
Hydroperoxide decomposition

In this stage, the hydroperoxides are decomposed into radical species and/or radical species are formed, reactions 2.4 and 2.5. The decomposition of hydroperoxides is a very slow process, but can be accelerated by adding metal catalysts. During the decomposition the amount of radicals increases, increasing the chance of hydrogen abstraction (reaction 2.6 and 2.7) and hydroperoxide formation.

$$\text{R-O-O-H} \rightarrow \text{R-O·} + \text{·O-H} \tag{2.4}$$
$$2\,\text{R-O-O-H} \rightarrow \text{R-O·} + \text{R-O-O·} + \text{H}_2\text{O} \tag{2.5}$$

$$\text{R-O·} + \text{R-H} \rightarrow \text{R·} + \text{R-O-H} \tag{2.6}$$
$$\text{H-O·} + \text{R-H} \rightarrow \text{R·} + \text{H}_2\text{O} \tag{2.7}$$
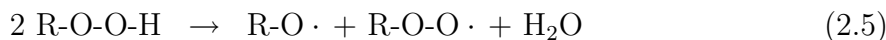
Cross-linking

Because the amount of radicals increases, the probability to form a cross-link by recombination increases. Different kind of bonds are formed; alkoxy (COC), peroxide (COOC) and carbon-carbon (CC) bonds.

$$2\,\text{R·} \quad \rightarrow \quad \text{R-R} \tag{2.8}$$
$$2\,\text{R-O·} \quad \rightarrow \quad \text{R-O-O-R} \tag{2.9}$$
$$2\,\text{R-O-O·} \quad \rightarrow \quad \text{R-O-O-R} + \text{O}_2 \tag{2.10}$$
$$\text{R·} + \text{R-O·} \quad \rightarrow \quad \text{R-O-R} \tag{2.11}$$
$$\text{R·} + \text{R-O-O·} \quad \rightarrow \quad \text{R-O-O-R} \tag{2.12}$$
$$\text{R-O·} + \text{R-O-O·} \quad \rightarrow \quad \text{R-O-R} + \text{O}_2 \tag{2.13}$$
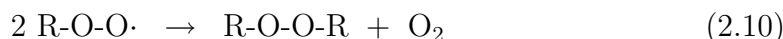
In the case of conjungated double bonds (see figure 2.1), the cross-linking predominantly proceeds via direct addition of radicals to the double bonds [48, 51].

$$\text{R·} + \text{C=C} \quad \rightarrow \quad \text{R-C-C·} \tag{2.14}$$
$$\text{R-O·} + \text{C=C} \quad \rightarrow \quad \text{R-O-C-C·} \tag{2.15}$$
$$\text{R-O-O·} + \text{C=C} \quad \rightarrow \quad \text{R-O-O-C-C·} \tag{2.16}$$
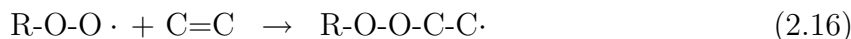
Degradation or side-reactions

The typical smell of alkyd coatings originates from the formation of volatile byproducts. Many side reactions occur during the autoxidation process. One of those side-reactions, β-scission, cleaves the linoleate molecule into aldehydes, such as hexanal, pentanal and propanal [48]. This β-scission also produces luminescence allowing it to be monitored [59–61]. Other typical byproducts are alcohols, ketones, carboxylic acids, epoxides, and endoperoxides.

2.2.2   Drier influence

The additives to speed up the drying of alkyd coatings are called driers. Driers are organometallic compounds which are soluble in organic solvents and binders. Chemically, driers belong to the class of soaps. The organic compounds can be altered to make the metal soluble in the solvent used. Drier metals can be divided in two categories: primary driers (active driers) and secondary driers (through driers). The first category, the primary driers, promote rapid surface drying with limited through drying properties. The term through drying means the drying takes place in deeper regions of the coating. The second category, the secondary driers or auxiliary driers, are assumed to have two effects. The first is the increase of the stability of the primary drier. The second is the promotion of the through drying. An overview of the different metals divided into the two categories based on their function is given in table 2.1 [19, 54, 62–64].

The most commonly used primary drier in commercially available alkyd paints is cobalt based. Although manganese and iron are also primary driers, they are considered

Primary driers	Secondary driers
Cobalt	Barium
Manganese	Zirconium
Iron	Bismuth
Cerium	Aluminium
Vanadium	Strontium
	Lead
	Calcium
	Potassium
	Lithium
	Zinc

Table 2.1: Drier metals divided into two categories based on their function; the primary driers and secondary driers.

to be less effective. The most important function of the primary driers is to speed up (or catalyze) the decomposition of hydroperoxides. However, in the literature other roles are also suggested as well, such as acceleration of oxygen absorption and peroxide formation [39, 53, 54]. The decomposition of hydroperoxides is often referred to as the Haber-Weiss cycle (in this example cobalt is used as the catalytic metal) [65–68]:

$$\text{R-O-O-H} + \text{Co}^{2+} \quad \rightarrow \quad \text{R-O} \cdot + \text{OH}^- + \text{Co}^{3+}$$
$$\text{R-O-O-H} + \text{Co}^{3+} \quad \rightarrow \quad \text{R-O-O} \cdot + \text{H}^+ + \text{Co}^{2+}$$
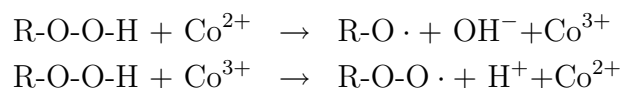
This cycle generates a high amount of radicals necessary to speed up the autoxidation process.

The effect of the primary driers (or catalysts) has been and is still an important research topic. In the last decade many alkyd coatings have been reformulated to water-borne systems, and as a consequence, the catalyst has been reformulated as well [69]. Nowadays, the search for new alternative for cobalt, which has been reported to be carcinogenic, has increased the research on the effects of driers even further. This can be clearly seen from the amount of recent work that has been published and was recently reviewed [70]. Many alternatives have been researched and reported [19], a new manganese based catalyst [71–73] and a new iron based catalyst [74]. The activity of these new catalyst was measured mainly in model systems. However, when these catalysts are used in real alkyd coatings oxygen transport becomes an additional variable in the curing process. The effects of these new catalysts should therefore be monitored in an alkyd coating using a spatial resolving technique.

The most commonly used secondary driers (auxiliary driers) are calcium and zirconium. Calcium containing driers are said to improve hardness and gloss and to reduce skin-formation [19]. Zirconium containing driers are believed to improve the through-drying, mainly by the formation of coordination bonds with hydroxyl- and carboxylic groups, available from the resin or formed during the drying process. Although the macroscopic effect on the drying has been studied, the precise way in which the secondary driers affect the drying process in an alkyd coating has remained unclear. Therefore, in the rest

of this thesis the term drier will be used for secondary driers. But for the primary driers the term catalyst will be used. The only research on curing of alkyd coatings for different drier combinations as a function of depth was performed by Mallegol et al. [68] for Co, Ca and Zr. In that paper the influence of drier combinations on the through-drying in water-borne alkyd emulsions was investigated by analyzing the T_2-relaxation times at three depths inside the coating measured using a NMR profiling setup.

2.3   Coating research tools

For each specific application coating properties have to be optimized, requiring many characterization tools. These properties concerns the durability and the appearance. Durability is determined by the protective properties, such as chemical resistance as well as mechanical performance. The appearance of the coating is determined by properties like transparency, color, and gloss, which have to be retained. Different substrates and the specific drying behavior on these substrates influence the durability and appearance. Therefore, techniques are required to measure the drying process of coatings as a function of depth and time. In this section we will discuss several techniques to characterize the drying of coatings. First, confocal Raman microscopy (CRM) and differential scanning calorimetry (DSC) are discussed; both techniques are used in this thesis. Next, some alternative techniques to probe the drying process, with more or less depth resolving capability, are discussed. In the next chapter the new NMR setup to measure the drying process as a function of depth will be discussed.

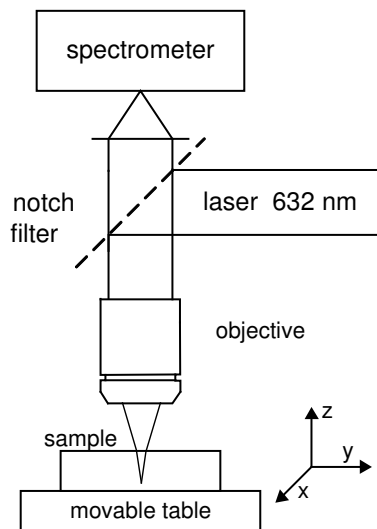### 2.3.1   Confocal Raman Microscopy

Fig. 2.2: Experimental confocal Raman setup.

The chemical composition of a thin coating layer can be measured by Confocal Raman Microscopy (CRM). In CRM a laser is focussed on a sample, see figure 2.2. By changing

the focus of the Raman microscope to a given depth, the Raman spectra of the corresponding volume element can be obtained. With Raman spectroscopy the saturation of double bonds can be measured, allowing the oxidation process to be followed.

The measurement principle is based on scattering of laser light; the scattered radiation has a frequency shifted from the frequency of the incident radiation. Only specific types of molecular vibrations can be measured using Raman scattering, depending on the selection rules for molecular transitions. To be able to interact with an electromagnetic field, a molecule should have an oscillating dipole at the right frequency. When during molecular vibration the polarizability is changed the vibration is Raman active. If the dipole moment is changing during the vibration, the vibration is infrared active. Since anti-symmetric vibration will change the dipole moment it is infrared active. Since symmetric vibration will change the polarizability it is Raman active. In the case of double bonds (C=C), the polarizability is changed because of symmetric stretching of this bond.

The ability of CRM to obtain chemical information as a function of depth and time makes it a valuable tool to follow the chemical changes during the curing process. However, it has some disadvantages. No information concerning the cross-linked network structure can be obtained, since CRM only measures the disappearance of double bonds, not the actual formation of a cross-link. Another disadvantage is the inability to probe nontransparent coatings. Even in transparent coatings there are some problems concerning a shift of the focus due to light refraction [26]. As a result the nominal position within the film should be corrected by a factor between 1.5 and 2.0 to get the actual position inside the coating. A recent study also indicates that the spatial resolution is less in deeper regions of the coating [41]. Studies of coatings applied on wood are impossible, because of the fluorescence caused by the substrate. This limits the use of CRM for studying the effects of the substrate on the drying of coatings.

2.3.2 Differential Scanning Calorimeter

A differential scanning calorimeter (DSC) measures the heat flux relative to the heat flux of a reference sample over a large temperature range. With a DSC heat capacity, heat of transition, kinetic data, and glass transition temperature can be determined. The latter, the glass transition temperature, is an important parameter for coating research, because it indicates the mobility of the polymer. This mobility is related to the final hardness of the coating.

At low temperatures, the polymers in the coatings exist in a glassy state. Upon heating of the sample the heat capacity c_p changes. Above the glass transition the polymer enters a rubbery state with more degrees of freedom, which translates in a higher heat capacity value c_p. During heating and cooling the systems passes through a sequence of non-equilibrium states. The history of cooling and heating influences the thermal behavior. The rate of heating and cooling causes a shift in the measured glass transition temperature (T_g). Therefore, the best procedure to measure T_g is to heat the sample to about 15 K to 30 K above T_g, followed by a short period 5 to 10 min of annealing to establish a thermodynamic equilibrium [75]. Afterwards the sample is cooled rapidly to a temperature of about 50 K below the expected glass transition temperature, followed by

the measurement of the T_g of the sample. For further details on the working principles of the DSC setup and the interpretation of the data, see Hohne et al. [75].

The DSC measures the coating as a whole, giving always an average. The relation between network properties, dangling ends, type of polymer, and the glass transition temperature is unclear. This complicates interpretation of the results.

2.3.3 Confocal Laser Scanning Microscopy

Another confocal imaging method is Confocal Laser Scanning Microscopy (CLSM). This confocal optical setup can even be used to image a 3D volume, because of the decreased scanning time compared to CRM. The laser focus scans a 3D volume while measuring the fluorescence or reflection intensity. Also two photon laser scanning microscopy exists, in which two photons of longer wavelength (800 nm) are simultaneously absorbed using the ultrahigh peak intensity of a femtosecond laser. A disadvantage of this technique over confocal Raman microscopy is the inability to obtain chemical information [24, 76].

2.3.4 Photoacoustic spectroscopy
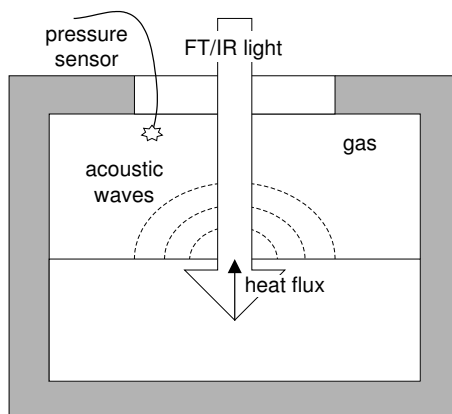
Fig. 2.3: Photoacoustic Fourier transform infrared spectroscopy.

Photoacoustic Fourier Transform InfraRed spectroscopy (PA/FT-IR) [77–79] can be used to depth profile a coating film. By changing the mirror velocity of a Michelson interferometer, the infrared spectrum is modulated. Subsequent Fourier transformation of the detected signal gives the absorption of the complete spectrum. The absorbed radiation will modulate the pressure of the coupling gas above the sample, because of the heat transport to the surface of the sample. The pressure inside the closed box is monitored by a pressure sensor. The amount of absorbed IR energy corresponds to the distribution of IR active functional groups throughout the specimen. The conversion of IR energy to heat is fast, so absorbed energy is immediately released as heat, which is transported to the surface. The physics of this process has been mathematically addressed by Rosencwaig and Gersho [80]. The thermal diffusion length μ_{th} can be varied by changing the modulation

frequency of the Michelson interferometer. By altering this frequency, μ_{th} will change, providing different penetration depths, ranging from 0 to 150 μm.

2.3.5 BK-drying test

The Beck-Koller drying test is the standard technique to determine drying times of a coating. Brass weights, each weighing 5 g, are used to apply pressure on several needles, which are slowly moved over the coating film applied on a long glass plate (about 1 m). The stages of drying can be observed from the prints of the needles on the coating:

1. A pear-shaped impression corresponds to the time involved with evaporation of solvent.

2. The cutting of a continuous track corresponds to a sol-gel transition.

3. An interrupted track corresponds to the surface-dry time.

4. When the needle no longer penetrates the film, the film is believed to be completely dry.

3. High spatial resolution NMR setup

Il n'existe pas de sciences appliquées, seulement des application de la science.
Louis Pasteur French biologist and bacteriologist (1822 - 1895)

3.1 Introduction

In 1924 Pauli demonstrated the existence of hyperfine splitting in atomic spectra [81]. He suggested that this splitting was the result of a coupling between the nuclear magnetic moments and the magnetic moments of the electrons. The existence of a nuclear spin was more clearly demonstrated by Bloch [82, 83] and Purcell [84] when they measured Nuclear Magnetic Resonance (NMR). They received the Nobel Prize for physics for this work in 1952.

In 1973 a short paper on imaging was published in Nature by Lauterbur [85]. In this paper he described a new imaging technique, a back projection method to produce an image of two test tubes. This experiment yielded information in two dimensions instead of a single dimension, and is therefore considered as the foundation of Magnetic Resonance Imaging (MRI). In 2003 the Nobel Prize in Physiology and Medicine was awarded to Paul C. Lauterbur and Peter Mansfield for their discoveries concerning "Magnetic Resonance Imaging (MRI)".

Over the years the technical development of NMR has increased further and further, towards higher resolution, faster imaging sequences, higher fields and higher field gradients. Nowadays, NMR is used in many fields of research and science. MRI is used in the medical and biological science. Chemists mostly use NMR for spectroscopy, which is very suitable for structure determination. NMR or MRI is also used for material science, e.g., rubbers, polymers, and porous materials. This latter field is the field of research presented in this thesis. We will now briefly discuss the developments that have led to the high resolution NMR imaging setup presented in this chapter.

When NMR is used for research on materials with high spatial resolution, spectroscopic information can no longer be obtained. The interpretation of the material properties have to be based on the acquired NMR signal decay. Since the article of Bloembergen et al. [86] relaxation effects are explained fundamentally from the interactions between nuclear spins. The mobility of the molecules together with the inter- and intra-molecular interactions, is used to explain the relaxation effects in fluids and solids. However, in polymers the interactions and mobility are much more complicated. As a result the influence of polymer mobility [87] and/or the network structure on NMR relaxation or diffusion is still researched extensively [88–96].

Stray field imaging is one of the first examples of high spatial resolution NMR. In this case the high spatial resolution is achieved by using the fringe field of a super conducting magnet [93, 97]. The NMR MOUSE (Mobile Universal Surface Explorer) [29, 98–100], a one sided NMR setup was reported in 1996, allowing the surface layer of many materials to be explored. Its high magnetic field gradient allows depth information to be obtained along the surface of rubber [101–103]. In 1999 Glover et al. [27] reported a new type of magnet pole tips to generate a high field gradient in which a horizontal plane has a constant magnetic field strength. This setup, can be viewed as a combination of STRAFI and the NMR mouse, which has the possibility to obtain high resolution (5 μm) spatial information in the vertical direction (1D).

In this chapter we will discuss the working principles of NMR and our changes to this design. For further detailed information on NMR we refer to [104–106].

3.2   *NMR*

The principle of NMR is based on the fact that nuclei (e.g. H, F, Na, Cl, P) resonate at a specific frequency in a certain magnetic field. In this thesis we will mainly focus on hydrogen nuclei, which is the most commonly studied nucleus in NMR. The resonance frequency, at which resonance occurs, depends on the strength of the applied magnetic field. If the field strength is varied in space, information about nuclei at different positions can be gathered. In general, the signal intensity is proportional to the spin density and the signal decay depends on interaction of the spins with their surroundings [86]. By manipulation of the main magnetic field using field gradients, images or profiles can be obtained.
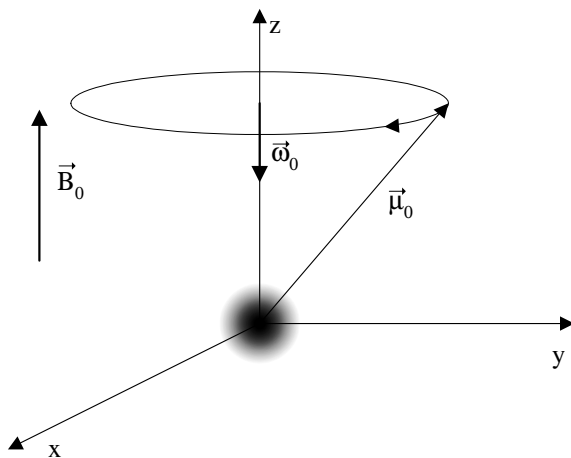
3.2.1   *Larmor precession*

Fig. 3.1: Larmor precession.

Many nuclei possess a magnetic moment $\vec{\mu}$. When such a nucleus is positioned in a magnetic field $\vec{B}_0$ the magnetic moment will precess around $\vec{B}_0$. This precession movement is described by, see e.g. [104]

$$\frac{d\vec{\mu}}{dt} = \gamma\vec{\mu} \times \vec{B}_0, \tag{3.1}$$

where γ is the gyromagnetic ratio. This motion is called Larmor precession, which is shown in figure 3.1. This equation is the classical equation for the precession, but, it also holds for the quantum mechanical description. Because in NMR measurements many nuclei are measured, the expectation value $\langle\vec{\mu}\rangle$ is equal to $\vec{\mu}$ in the classical description [105]. The rate of precession depends on the strength of the magnetic field, and is given by:

$$f_L = \frac{\omega_0}{2\pi} = \frac{\gamma}{2\pi}B_0. \tag{3.2}$$

In this equation B_0 represents the strength of the main magnetic field, and f_L is the Larmor frequency. Each isotope has an unique gyromagnetic ratio, for ^{1}H or a proton $\gamma/2\pi = 42.58$ MHz/T. The sensitivity and the natural abundance determine whether other nuclei can be measured easily. For ^{19}F the gyromagnetic ratio $\gamma/2\pi = 40.05$ MHz/T and its sensitivity relative to hydrogen is 0.83.

3.2.2 Excitation of the nuclear magnetic moments

If a small magnetic field B_1 is applied perpendicular to the main magnetic field (B_0) a precession movement around the resulting magnetic field will occur. This gives the possibility to manipulate the magnetic moment of the nucleus. This manipulation is only effective if a time-varying $B_1(t)$ field is applied with a frequency equal to the Larmor frequency. In a frame rotating with a frequency equal to the Larmor frequency, the magnetic moment $\vec{\mu}$ is stationary if B_1 equals zero. From now on we will describe the behavior only within this frame of reference. In NMR experiments the nuclear magnetization vector $\vec{M} = (M_x, M_y, M_z)$ is measured. This is the sum over all magnetic moments present inside the sample:

$$\vec{M} = \sum_i \vec{\mu}_i. \tag{3.3}$$

At the start of the experiment the transverse components M_x, M_y are zero, because in equilibrium $\vec{M}$ is directed along the z-axis: $\vec{M} = (0, 0, M_0)$. A field $B_1(t) \perp B_0$ varying at the Larmor Frequency will be stationary within the xy-plane of the rotating frame. Application of such a radio frequency (RF) field B_1, will cause the magnetization to rotate away from the z-axis. In figure 3.2 the magnetization is initially along the z-axis, the excitation (rotation) is performed around the x-axis. A rotation over an angle θ is achieved by applying B_1 a time t_p:

$$\theta = \gamma B_1 t_p. \tag{3.4}$$

The rotation around the x-axis can be described using the following rotation matrix:

$$R_\theta = \begin{pmatrix} 0 & 0 & 0 \\ 0 & \cos\theta & -\sin\theta \\ 0 & \sin\theta & \cos\theta \end{pmatrix}, \tag{3.5}$$
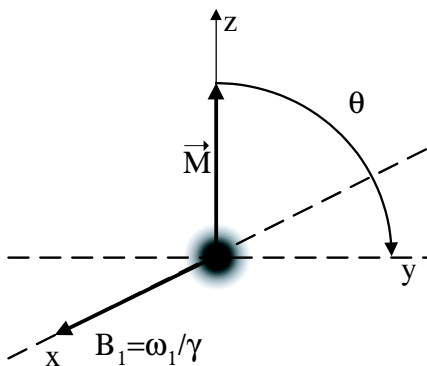
Fig. 3.2: Rotation of the magnetization around the x-axis, caused by a RF-excitation.
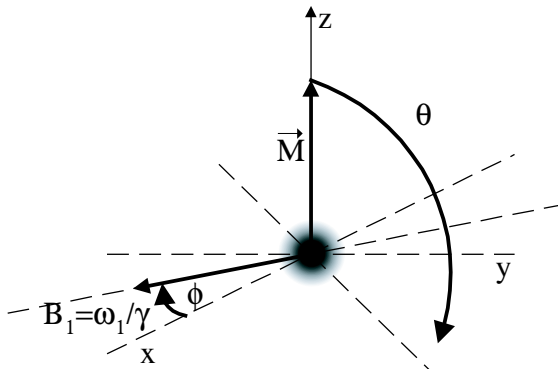
Fig. 3.3: Rotation of the magnetization around an arbitrary axis in the xy-plane, caused by RF-excitation.

Pulse sequences like the Carr-Purcell-Meiboom-Gill (CPMG) or Ostroff-Waugh (OW) sequence contain RF pulses with different phases. The matrix describing an excitation pulse with an arbitrary phase ϕ, see figure 3.3, can be calculated from a rotation to the x-axis ($R_{-\phi}$), then an excitation around the x-axis ($R_{-\theta}$) followed by rotation back to the arbitrary phase (R_ϕ):

$$R_{\theta\phi} = R_\phi R_\theta R_{-\phi}, \tag{3.6}$$

in which R_ϕ is a rotation around the z-axis and is described by

$$R_\phi = \begin{pmatrix} \cos\phi & -\sin\phi & 0 \\ \sin\phi & \cos\phi & 0 \\ 0 & 0 & 1 \end{pmatrix}. \tag{3.7}$$

Combining equations 3.5, 3.6, and 3.7 the excitation can be fully described by

$$
\begin{aligned}
R_{\phi,\theta} &= R_\phi R_\theta R_{-\phi} \\[2mm]
&= \begin{pmatrix}
\cos\phi^2 + \cos\theta\sin\phi^2 & (1-\cos\theta)\cos\phi\sin\phi & \sin\theta\sin\phi \\
(1-\cos\theta)\cos\phi\sin\phi & \cos\theta\cos\phi^2 + \sin\phi^2 & -\cos\phi\sin\theta \\
-\sin\theta\sin\phi & \cos\phi\sin\theta & \cos\theta
\end{pmatrix}.
\end{aligned}
\tag{3.8}
$$

This rotation matrix is only valid for an on-resonance system with arbitrary phase ϕ of the RF pulse, exciting over an angle of θ in xyz-coördinate system. On-resonance means that the applied RF pulse is exactly matched to the Larmor frequency. This is not the case when performing measurements in a high gradient NMR setup, due to the finite frequency bandwidth of the excitation pulse. For further details on off-resonance excitation, see Appendix A. We will return to this point in section 3.2.6, where we will discuss the effect of slice selection by the applied RF pulse.

3.2.3 Relaxation

After the nuclear magnetization vector is rotated, it will restore to its original position along the main magnetic field. This is caused by two relaxation effects [86]. The first

is longitudinal or spin-lattice relaxation. The corresponding relaxation time T_1 reflects the rate at which the component of the magnetization vector $\vec{M}$ parallel to the main magnetic field $\vec{B}_0$ is restoring. The second is the transverse or spin-spin relaxation time. The corresponding relaxation time T_2 reflects the rate at which the component of the magnetization vector $\vec{M}$ perpendicular tot the main magnetic field approaches zero. This spin-spin relaxation time is equal or less than the spin-lattice relaxation, see [86], due to dephasing of the nuclei caused by dipole-dipole interactions. When the mobility of the hydrogen nuclei decreases, their correlation time τ_c increases. As a result more dephasing occurs, because the dipole-dipole interactions are less effectively cancelled out, resulting in a shorter T_2 values. This makes T_2 very susceptible to changes in mobility (e.g. cross-linking) inside a coating. Since Differential Scanning Calorimetry measures the mobility on the molecular scale as a function of temperature, a relation between T_g measured with DSC (see 2.3.2) and the relaxation times T_2 measured with NMR can be expected.

The equation describing the effect of these relaxation phenomena on the macroscopic nuclear magnetization vector $\vec{M}$ is

$$\frac{d\vec{M}}{dt} = - \begin{pmatrix} 1/T_2 & 0 & 0 \\ 0 & 1/T_2 & 0 \\ 0 & 0 & 1/T_1 \end{pmatrix} \vec{M} + \begin{pmatrix} 0 \\ 0 \\ M_0 \end{pmatrix}. \tag{3.9}$$

3.2.4 Detection of the magnetization

In NMR experiments only the nuclear magnetization in the transverse plane can be recorded. The transverse magnetization $M_t = M_x + iM_y$ is acquired by measuring the magnetic induction voltage across a stationary coil in the laboratory frame. The precession movement of the magnetization causes the magnetic induction. Different kinds of pulse sequences can be used to manipulate the magnetization, which allows the relaxation times (T_2 and T_1) to be obtained from the recorded signals. By using magnetic field gradients spatial information can be encoded in the phase and frequency of the precession of the local magnetization vector.

3.2.5 Obtaining spatial information

For research on coatings a resolution (in the y-direction, perpendicular to the coating layer) of about 5 μm is necessary in order to observe processes inside a film of about 100 μm. To achieve this high spatial resolution a magnetic field gradient is required. This gradient causes changes in magnetic field strength and, consequently, changes in Larmor frequency,

$$\omega_L(\vec{r}) = \gamma B_z = \gamma(B_0 + y \cdot G_y). \tag{3.10}$$

Here y is the position in the direction of the gradient and G_y the gradient of the z-component of the magnetic field in the y-direction. During the recording of the NMR signal the different nuclei resonating at different frequencies contribute to the recorded signal:

$$S(t) = \int_V \rho(y) \exp[i\omega_L(y)t]dy. \tag{3.11}$$

To resolve the properties of layers in the y-direction, the Larmor frequency needs to be constant in the horizontal plane. For now we will approximate the gradient by $G_y = \partial B_z / \partial y$, although this is not strictly valid in high gradient NMR setups. We will return to this point in section 3.4. Many parameters influence the resolution; we will discuss the two most important resolution limiting parameters. For a more detailed discussion see [28, 106, 107].

Recording window limited resolution

The relation between distance and frequency difference inside the sample is given by

$$\Delta\omega = \gamma G_y \Delta y. \tag{3.12}$$

To avoid aliasing, a signal should be sampled at a frequency f_s of at least twice the maximum frequency that is present in the signal (Nyquist theorem). Taking N_s samples the total acquisition time is: $t_{acq} = N_s t_s$, where $t_s = 1/f_s$. The resolution without any filtering is given by [28, 106, 108]

$$\Delta y = \frac{\Delta\omega}{\gamma G} = \frac{2\pi}{\gamma G t_s N_s} = \frac{2\pi}{\gamma G t_{acq}}. \tag{3.13}$$

For a setup with a gradient strength of 36 T/m and an acquisition window $t_{acq} = 200$ μs, this gives a best achievable resolution of 3.2 μm. Increasing the window will enhance the resolution, however, other resolution determining factors will gain importance, such as decreasing SNR, field abberations, diffusion, sample orientation, and the transverse relaxation time of the sample.

Relaxation limited resolution

When the relaxation time T_2 is very short, the best achievable resolution is no longer determined by the recording window but by T_2. In that case, the resolution is given by [28]

$$\Delta y = \frac{2}{\gamma G T_2}. \tag{3.14}$$

3.2.6   Selective excitation

Every RF-pulse that is applied to the sample has a certain finite bandwidth $\Delta\omega_L$, corresponding with the duration of the pulse t_p and the pulse shape. Because of the high magnetic field gradient, the sample is not homogenously excited by such a pulse. The resulting NMR profile obtained using the OW-sequence (see section 3.3.3) with block shaped (hard) RF pulses ($t_p = 1$ μs) is simulated and given in figure 3.4. An infinitely large homogeneous sample is used in the simulation. The off-resonance rotation matrix given in Appendix A is used to calculate the excitation. The FWHM frequency bandwidth that is measured is given by

$$\Delta\omega_L = 0.8\frac{2\pi}{t_p}. \tag{3.15}$$
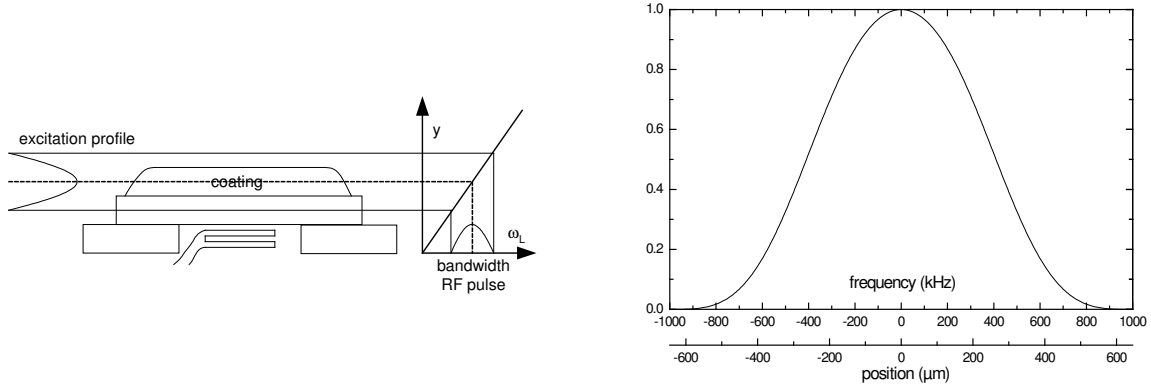
Fig. 3.4: Selective excitation (left) and the simulated RF bandwidth (right). The strength of the gradient (36 T/m) and the RF-bandwidth determines the excited region of the sample. A block shaped RF-pulse was assumed.

The thickness of the excited volume is given by

$$\delta y = 0.8 \frac{2\pi}{\gamma G t_p},\tag{3.16}$$

where $G = 36$ T/m in our setup. This means that a maximum sample size of about 500 μm can be excited (FWHM) for a typical pulse duration $t_p = 1$ μs. From figure 3.4 it can be deduced that for a sample with a thickness less than 200 μm normally no correction is required, because the variation of the profile is less than the noise in the signal.

The actual shape of the RF-pulse is also determined by the properties of the RF power amplifier and the quality factor of the tuned RF-circuit. This may slightly modify the simulated profile plotted in figure 3.4.

3.3   NMR pulse sequences

Many sequences can be used to obtain information on different processes at different time and length scales, from measurements of $T_1, T_{1\rho}, T_2$, and diffusion. The most commonly used NMR sequences will be explained in the present section.

3.3.1   Spin-echo sequence

A spin-echo is created by the pulse sequence shown in figure 3.5. At $t < 0$ (a) the nuclear magnetization is equilibrium. Next (b) at $t = 0$ a 90° pulse is given. After the 90° pulse is applied, the magnetic moments forming the magnetization vector in the transverse plane start to dephase (c) due to field inhomogeneities or the presence of magnetic field gradients.

If at $t = \frac{1}{2}t_e$ a 180° pulse is given; the direction of the spins is reversed. Consequently, they start to rephase again (d). At exactly $t = t_e$ (e) the spins are rephased and a so called spin-echo is created. Next the spins start to dephase again, resulting in loss of
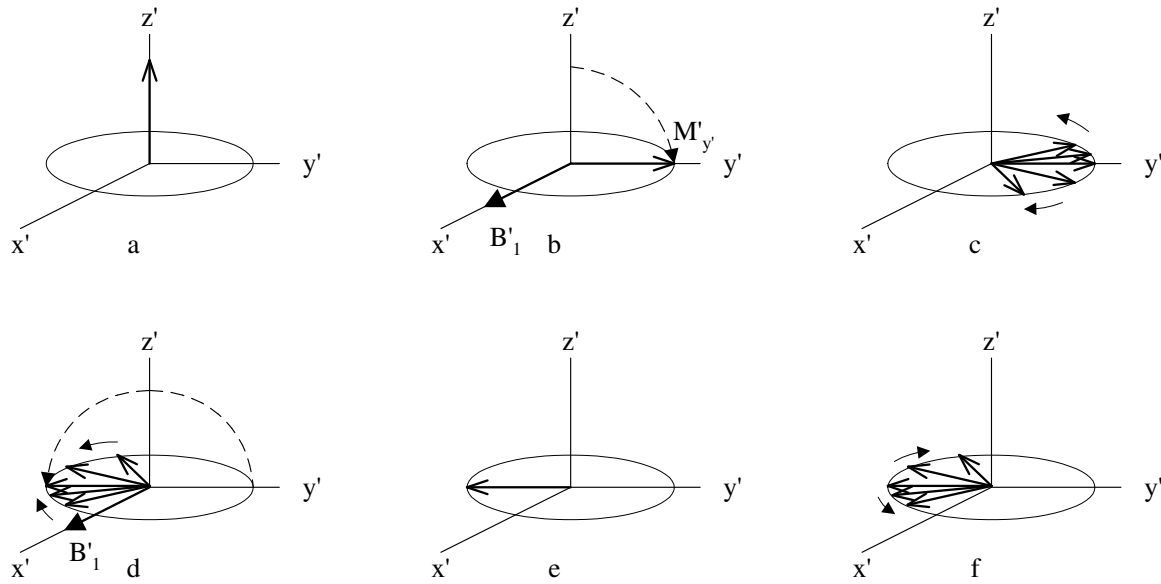
Fig. 3.5: The figure shows the magnetization vector in the rotating frame. The dephasing is caused by the applied magnetic field gradient, which causes the Larmor frequency to differ for different positions inside the sample.
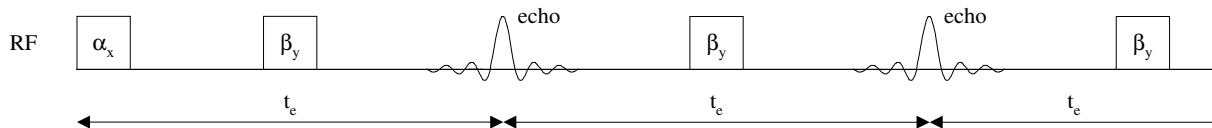
Fig. 3.6: CPMG sequence: $\alpha = 90°$ and $\beta = 180°$. OW sequence: $\alpha = \beta = 90°$.

signal (f). This sequence is called the Hahn spin-echo sequence. By Fourier transforming the recorded signal a density profile in the direction of the applied field gradient can be obtained.

Normally after an echo a long delay is added, to give the magnetization the possibility to restore to its equilibrium, so that the spin-echo experiment can be repeated. The time needed to effectively restore the magnetization to its equilibrium is about three times T_1.

3.3.2   Carr-Purcell-Meiboom-Gill sequence

The Carr-Purcell-Meiboom-Gill sequence (CPMG) is given in figure 3.6. It starts with a 90° pulse, rotating the magnetization vector in the transverse plane. At $t = \frac{1}{2}t_e$ the 180° pulse is applied. The spins start to rephase creating an echo. After recording of this echo again a 180° pulse is given, giving rise to a second spin-echo signal. The time between the pulses is called the inter-echo time t_e. This 180° pulse is repeated N times yielding a series of spin-echoes. The recorded signal intensity will decrease for each next echo,
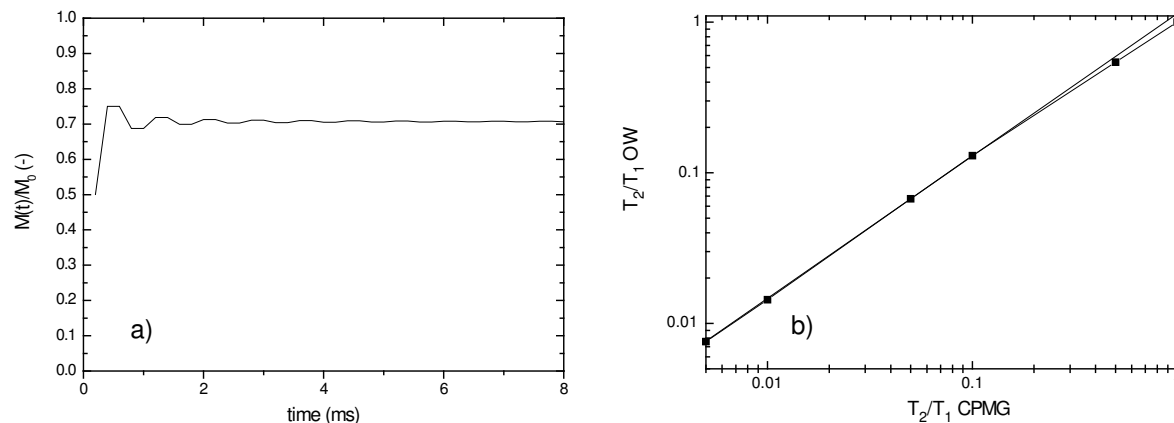
Fig. 3.7: a) Intensity variations observed when measuring a system with a very long T_2 and T_1 value using an OW-sequence. Note that the total magnetization (M_0), that would be measured with a CPMG sequence, is set equal to 1. b) Difference in T_2 values measured using an OW sequence and a CPMG sequence (simulated with a T_1 of 100 ms).

because of the T_2 relaxation. The decay of the spin-echo signal is given by

$$S(mt_e) = \sum_i S_i \exp\left(-mt_e/T_2^i\right), \tag{3.17}$$

where t_e denotes the interecho time and m the number of the acquired echo. The summation over i takes into account the presence of multiple relaxation times in the coating, as will be shown in chapter 4.

3.3.3 Ostroff-Waugh sequence

The Ostroff-Waugh sequence [109] is identical to a CPMG sequence except, for the 180° pulses, which are replaced by 90° pulses, see figure 3.6. After the second 90° pulse is applied, only half of the magnetization is refocussed: the other half remains along the longitudinal axis, see figure 3.7a. During the second echo, after another 90° pulse, the magnetization is refocussed to an intensity of 3/4. For the first 5 echoes the intensity variations are given in table 3.1. The calculations of these intensities are beyond the scope of this thesis, but the theoretical background can be found in [106, 110]. Two different names for this theory are used in literature, the theory of configurations and coherent pathway calculations.

The OW sequence is used in our experiments the measurements of the transverse relaxation time. This sequence must be used because the shorter pulses allow a more complete excitation of the sample, as was discussed in section 3.2.6. Correction of the signal decay of the OW signals is required. In addition some longitudinal magnetization is transferred into the transverse components causing the T_2 to increase. This effect is shown in figure 3.7b. In principle, the spin-echo signal decay may increase if the diffusion of molecules is significant [107]. However, since the diffusion of polymers in the coatings

echo	echo intensity
1	1/2
2	3/4
3	6/8
4	11/16
5	22/32

Table 3.1: OW signal intensity
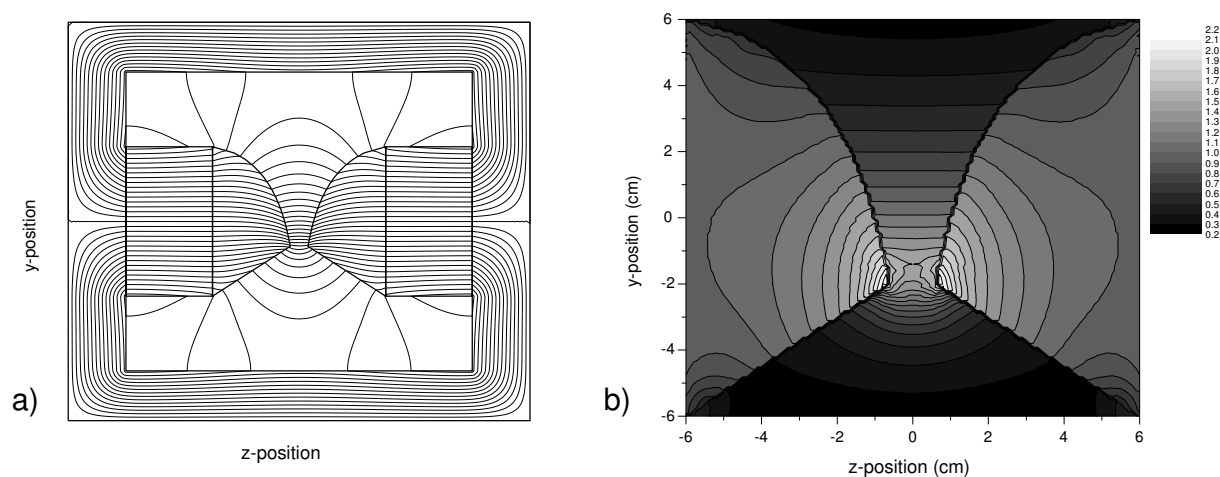
Fig. 3.8: Magnetic fields created by the designed magnet poles. a) Simulation of the magnetic field lines between the poles. b) Magnitude of the magnetic field given in T.

studied in this thesis is low, this effect is not a problem for the measurements presented in the next chapters.

3.4   Design of the setup

Profiling thin film layers using NMR requires a high gradient. Within a horizontal layer of the sample the magnetic field $|\vec{B}|$ should be constant, because the Larmor frequency of the spins in that layer need to be constant, which is the basic principle of the GARField design by Glover et al. [27]. In this section the shape of the magnetic pole tips satisfying this requirement will be calculated and explained in more detail [27]. A low curvature of $|\vec{B}|$ within a region of interest of 5×5 mm is required to obtain a satisfactory resolution. The pole tips will be mounted in an electromagnet, so they should meet specific dimensional criteria.

3.4.1   Design of magnet pole tips

In the design, the poles tips are assumed to be infinitely long in the x-direction, in which case the problem is reduced to a 2D problem. The Maxwell equations for a static magnetic

field without any currents are

$$\nabla \times \vec{B} = 0, \tag{3.18}$$

$$\nabla \cdot \vec{B} = 0. \tag{3.19}$$

One dimension is removed by taking $\vec{B} = (B_x, B_y, B_z) = (0, B_y, B_z)$. Equation (3.18) shows that a gradient in the y-direction (G_y) is given by

$$G_y = \frac{\partial B_z}{\partial y} = \frac{\partial B_y}{\partial z}. \tag{3.20}$$

If there is a spatially varying field $(G_y = \partial B_z/\partial y)$ then there must also be a gradient in another component of the magnetic field $(\partial B_z/\partial y)$. In fact it is not possible to create a gradient in one of the magnetic field components without creating another. In normal setups this problem also exists, but because the radius of curvature $|\vec{B}|/G$ is of the order of 10^2 m for conventional imaging applications, the variations are small compared to the main magnetic field component. When a gradient of the magnetic field amplitude $|\vec{B}_0|$ is created instead of a gradient of one component, this problem can be solved.

We need to find the shape of the pole tips in order to create such a magnetic field gradient, to which end we will use the Maxwell equations again. Since the rotation of a gradient of a scalar potential is always zero, we can take $\vec{B} = \nabla\Phi$. When inserted into equation 3.19, this will result in the Laplace equation

$$\nabla^2\Phi(z, y) = 0. \tag{3.21}$$

We will solve this equation with the method of separation of variables

$$\Phi(z, y) = Z(z)Y(y). \tag{3.22}$$

Equation (3.22) inserted into (3.21) leads to:

$$\frac{d^2Y(y)}{dy^2}\frac{1}{Y(y)} = -\frac{d^2Z(z)}{dz^2}\frac{1}{Z(z)} = \lambda^2, \tag{3.23}$$

where λ is a constant. The general form of the resulting scalar potential satisfying the Laplace equation and vanishing for $y \to \infty$ may be written as

$$\Phi(z, y) = \exp(-\lambda y)(A\sin(\lambda z) + B\cos(\lambda z)). \tag{3.24}$$

Because of the symmetry of the magnetic field with respect to $z = 0$, see figure 3.8, only the following solution will be of interest

$$\Phi(z, y) = A\sin(\lambda z)\exp(-\lambda y). \tag{3.25}$$

Calculating the components of $\vec{B}$ and its modulus $|\vec{B}|$ yields

$$B_z = \frac{\partial\Phi}{\partial z} = A\lambda\cos(\lambda z)\exp(-\lambda y), \tag{3.26}$$

$$B_y = \frac{\partial\Phi}{\partial y} = A\lambda\sin(\lambda z)\exp(-\lambda y), \tag{3.27}$$

$$|\vec{B}| = A\lambda\exp(-\lambda y). \tag{3.28}$$

The last equation shows that indeed the amplitude of the magnetic field is constant in the xz-plane. We can now calculate the gradient, which results in:

$$G = \frac{d|\vec{B}|}{dy} = -A\lambda^2 \exp(-\lambda y). \tag{3.29}$$

Dividing this equation by $|\vec{B}|$ shows that the ratio $G/|\vec{B}|$ is equal to $-\lambda$. The shape of the pole tips can be calculated from the equipotential of Φ.

$$A \sin(\lambda z) e^{-\lambda y} = C. \tag{3.30}$$

Together with appropriate boundary conditions this equation, will determine the shape of the pole tips. At $y = 0$ the poles are spaced at a distance $\Delta z = 2$ cm, which is necessary for the placement of the samples. The pole tips in our setup where chosen 12 cm high and 12 cm long. The total space in the yoke of the magnet was 12 cm, which also restricts the height of the pole tips. The following set of equations determines our design:

$$z(y) = \frac{1}{\lambda} \arcsin \left(D e^{\lambda y} \right), \tag{3.31}$$

$$z(0) = 1.0 \cdot 10^{-2} \text{ m}, \tag{3.32}$$

$$z(6.0 \cdot 10^{-2} \text{ m}) = 6.0 \cdot 10^{-2} \text{ m}, \tag{3.33}$$

where $D = C/A = \sin[\lambda z(0)]$. Using the boundary conditions λ can be calculated and is given by $\lambda = 23.8$ m^{-1}. A simulation of the magnetic field created by the designed pole tips is displayed in figure 3.8a, in which the magnetic field lines are plotted. Figure 3.8b shows the strength of the magnetic field between the pole tips. Note that the magnetic field is constant in the horizontal plane between $y = -1$ cm and $y = 1$ cm. For a magnetic field of 1.4 T at $z = 0$ the theoretical magnetic field gradient at that position equals 34 T/m.

3.4.2   Sample placement
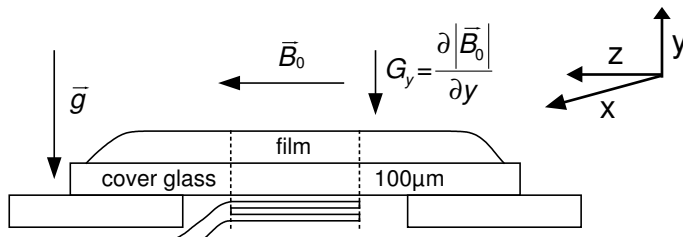
Fig. 3.9: RF coil and sample placement.

An insert was built to measure samples in the region between the constructed pole tips. In figure 3.9 the sample placement is shown. The RF coil is a surface coil on which the sample is placed. The coil has a large filling factor, which is advantageous for the signal to noise ratio (SNR). The sensitivity of the coil decreases with the distance between
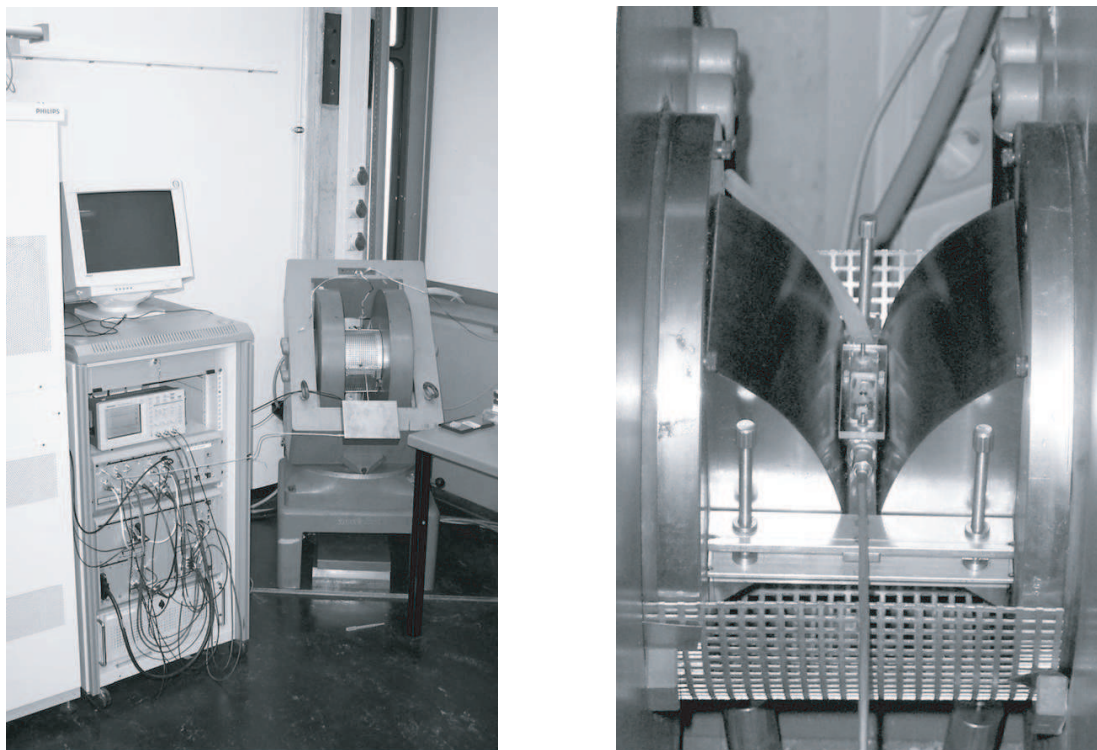
Fig. 3.10: Left the electromagnet with the data-acquisition system is shown. On the right the pole tips are shown, mounted inside the electromagnet. The screws are used to align the sample plateau to the magnetic field.

the sample and coil. The diameter of the coil is 5 mm, so samples with a thickness larger than 2.5 mm cannot be measured. Slices, with a thickness equal to the resolution, and an area roughly equal to $\frac{1}{2}\pi d^2$, determined by the coil diameter d, are measured. Note that the gravitation is directed perpendicular to the sample, making it possible to measure wet films.

To achieve the proper resolution a correct alignment of the sample is very important. To do this three alignment screws are present. The alignment is performed manually using a reference sample. In figure 3.10 the setup is shown. The sample placement together with the alignment screws are clearly visible.

3.4.3 Gradient calibration

After mounting of the pole tips in the electromagnet the actual gradient and resolution were determined. First the magnetic field strength at the center between the pole tips was measured for different currents through the electromagnet. The field strength was determined using a Hall-probe. Figure 3.11 shows the result of this measurement. One can clearly see that the gradient is fairly constant between $y = -1$ cm and $y = 1$ cm, as indicated by the black line. The gradient calibration was performed using a reference
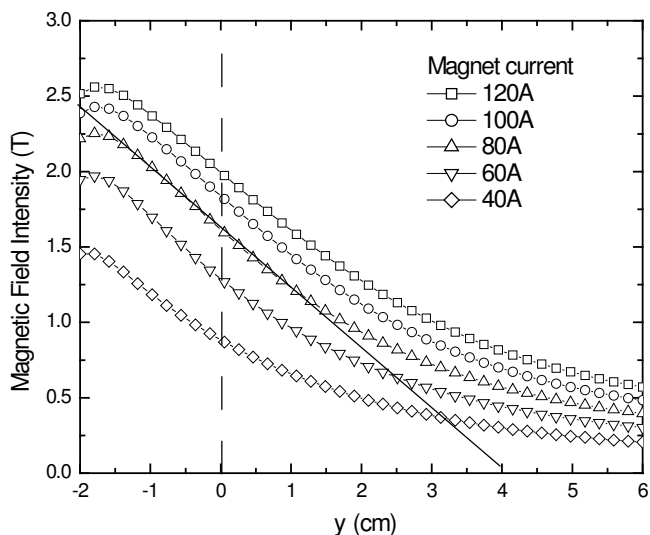
Fig. 3.11: Magnetic field strength at the center between the pole tips ($z = 0$) measured as a function of height (y) for different current settings of the electro magnet. The magnetic field strength was determined using a calibrated Hall probe. The vertical dashed line is the position of the sample. The gradient is indicated by the solid line.
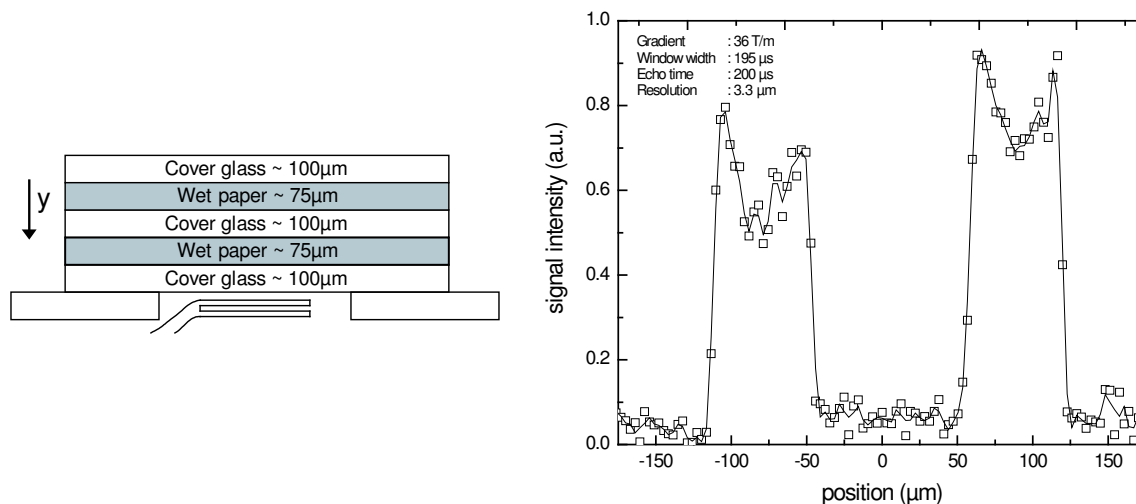
Fig. 3.12: Left the reference sample is shown, which is used for gradient calibration and resolution determination. Note that the sample is not depicted on scale. The paper is wetted using a mixture of glycerol (less evaporation), water, and $CuSO_4$ (shorter T_1). On the right the measurements on this sample are shown. The theoretical spatial resolution (the distance between adjacent data points in the figure) is equal to 3.3 μm. One can clearly see that more water is present on the interface between the paper and the glass.

sample, shown in figure 3.12. The gradient was determined to be 36.4 ± 0.2 T/m for a field of 1.4 T (38.6 A), which is in good agreement with the value 34 T/m expected from the calculation of the shape of the pole tips.

3.4.4 Resolution measurements

The resolution is measured using a reference sample as shown in figure 3.12a. We assume that the interface between the wet paper and the glass to be much smaller than the resolution, in which case the number of data points on the edges of the signal shown in figure 3.12b reflects the actual resolution. The actual resolution appears to be better than 6.6 μm (2 points on the edges).

3.4.5 Resolution versus Signal to Noise Ratio

After curing of an alkyd resin, the mobility of the polymer has decreased significantly because of the increased cross-linking, which results in a fast signal decay (short T_2). Therefore, an optimum setting of the inter-echo time t_e and acquisition time t_{acq} has to be chosen. In this section we will discuss the effects that are observed when the resolution is enhanced.

First, enhancing the resolution means increasing the recording window and hence the inter-echo time t_e has to be increased. The first echo is recorded later, meaning that contributions to the signal with short relaxation times are missed. Second, less points are measured in the typical decay curve, which implies that discrimination of various short relaxation times in the signal decay becomes harder or even impossible. The third effect is a decrease of SNR when the resolution is enhanced, which is caused by a decrease in sample volume per spatial point (1D 'voxel'). To compensate for this effect more signal averages are required. Since the drying of a coating requires a certain time-resolution compared to the drying process, the maximum amount of averages is limited. This sets an upper limit for the resolution. The following equation shows the dependence of the SNR to the amount of averages N_{avg} and acquisition window t_{acq}:

$$SNR \propto \sqrt{\frac{N_{avg}}{t_{acq}}}.$$
(3.34)

4. Comparison of NMR and confocal Raman microscopy as coatings research tools

Recently, several new experimental techniques have been developed to measure the spatial and temporal evolution of a drying coating film. One of these techniques is nuclear magnetic resonance (NMR) using a very high magnetic field gradient. An advantage of this technique is the ability to image a nontransparent coating film perpendicular to its surface with a resolution of about 5 μm (depth profiling). Another, well known technique is confocal Raman microscopy (CRM). This chapter deals with a comparative study of such a micro imaging NMR setup and confocal Raman microscopy for two alkyd coatings, one organic solvent-borne and another water-borne. The NMR and CRM results show a good similarity, when comparing NMR profiles with the disappearance of the double bonds (CRM-detectable) of the unsaturated fatty acids. This indicates that the disappearance of the double bonds in the fatty acid side chains of the alkyd molecules is directly connected with the formation of cross-links by these fatty acid entities. This oxidative cross-linking results in an increase of viscosity and therefore in a change of the measured NMR relaxation times.

4.1 Introduction

Legislation concerning the use of coatings with volatile organic components (VOC) drives coating manufacturers to focus on and increasingly produce water-borne coatings. Still, much research is needed to develop water-borne coatings of the same quality as their organic solvent-borne counterparts. Techniques to spatially resolve properties of coating films in situ include confocal Raman microscopy (CRM, see chapter 2), photoacoustic spectroscopy (PAS) [77, 80] and two-photon confocal laser scanning microscopy (CLSM) [24, 76]. CRM has the advantage that it directly gives chemical information. The imaging time of two-photon CLSM is greatly reduced compared to CRM, but it only gives information on fluorescence and/or reflection. Each of these analytical techniques has specific advantages and limitations [111]. New techniques for research and characterization of paint films using Nuclear Magnetic Resonance (NMR), e.g. GARField [27] and NMR MOUSE [29], have recently become available. A major advantage of NMR over any spatially resolving optical spectroscopic technique is that even nontransparent coatings can be used. However, results from NMR experiments using high magnetic field gradients are often difficult to interpret [86, 112], due to the many factors influencing the NMR signal. In the present study we will combine NMR and CRM data on the drying

of alkyd paint. The NMR setup is a GARField design incorporating an electromagnet. A combined interpretation of the results from both techniques has the advantage that it allows integrating chemical and mobility data. After application of a paint film two stages can be distinguished, first evaporation of the solvent takes place (physical drying) and subsequently curing takes place, in which the polymer of the coating chemically reacts to form cross-links. This latter stage will be referred to as curing. During these two stages many properties, such as molecular self diffusion and viscosity, will vary. These variations influence the rate of the NMR signal decay.

In section 4.2, the principles of both techniques are explained. In section 4.3, first the NMR measurements on a thin paint film are discussed, as well as the problems and questions arising from these measurements. Next, CRM results are presented and used as complementary information to explain the curing process of the film. Finally, we will end with the discussion and conclusion.

4.2   Techniques

In this section we will describe the NMR and CRM techniques used to analyze spatial variations of paint properties within a thin film.

4.2.1   Nuclear Magnetic Resonance
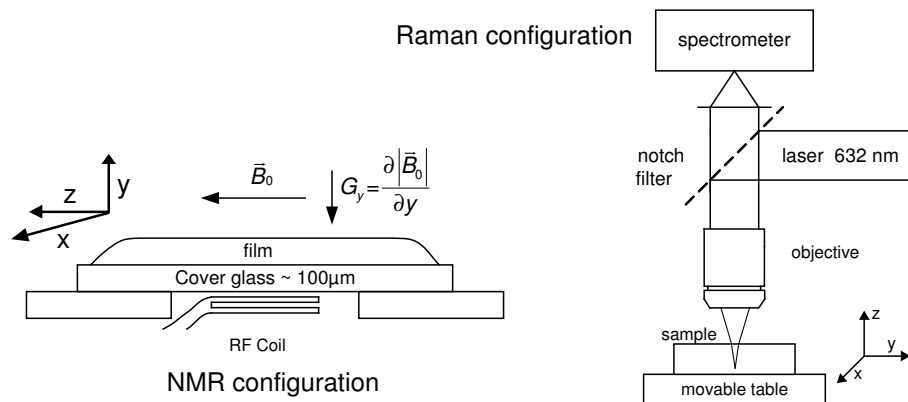
Fig. 4.1: Configuration of the NMR and Raman setup.

Magnetic resonance imaging (MRI) is a well known technique for making images of the human body. Its principle is based on the fact that magnetic nuclei located in a magnetic field may resonate when excited by a radio frequency (RF) pulse. The resonance frequency (f) depends linearly on the applied magnetic field (B), $f = \gamma |\vec{B}|$, with γ the gyromagnetic ratio (for hydrogen nuclei, $\gamma = 42.58$ MHz/T). It is possible to obtain spatial information by varying the magnetic field with position, $f = \gamma(|\vec{B}| + G_\alpha \alpha)$ where $G_\alpha = \partial B_z / \partial_\alpha$ denotes the field gradient and $\alpha = x, y, z$. The signal intensity reflects the amount of nuclei present. To obtain a high spatial resolution (< 10 μm) a very high field gradient

must be applied. A technique used to obtain such a high resolution is stray field imaging [28], in which the gradient just outside the bore of a superconducting magnet is used. Another possibility is the use of a so-called NMR MOUSE [29]. However, Maxwell's equations show that when a high magnetic field gradient in a certain direction is applied, the magnitude of the field $|\vec{B}|$, and hence the resonance frequency, also varies in a plane perpendicular to that direction. The corresponding decrease in spatial resolution is very pronounced in high gradient applications, as is the case in both techniques mentioned above.

At the University of Surrey, the GARField technique [27] was introduced. In this design a gradient in the magnitude of magnetic field was realized, $G_y^{mag} = d|\vec{B}|/dy$ (see figure 4.1) by creating special-shaped pole tips. It is then possible to perform depth profiling of a film, that is oriented perpendicular to the y-direction. The advantage of a setup as shown in figure 4.1 is that a sample can be placed directly on top of a surface coil, which gives good signal to noise ratio. Also the gravity is perpendicular to the applied paint film, which makes it possible to measure wet films.

The NMR setup for the present study contains an electromagnet generating a magnetic field of 1.4 T at the position of the sample. The gradient is 36.4 ± 0.2 T/m.

The obtained NMR signal (S) not only gives information on the density of the magnetic nuclei (spins) ρ, but also on the changes in the environment of these nuclei. The environment of these nuclei determines the NMR signal decay rate. Different pulse sequences can be used to obtain the relaxation times T_1, T_2, and the diffusion of spins within the film. The first two quantities give information on the spin-lattice interactions and the spin-spin interactions, respectively.

4.2.2 Raman spectroscopy

Chemical compositions of coating systems can be analyzed by probing molecular vibrations, using infrared spectroscopy (IRS) or Raman spectroscopy (RS). In IRS the absorption of light passing through a sample is measured. RS is based on radiation being scattered inelastically, due to molecular motions. The scattered radiation has a frequency shifted from that of the incident radiation. The radiation at a lower frequency, called Stokes radiation, is normally used, but also radiation at a higher frequency (anti-Stokes radiation) can be used. If during molecular vibration the polarizability changes, the vibration is Raman active. If the dipole moment changes during the vibration, it is infrared active. Anti-symmetric vibration will change the dipole moment, so it is infra red active, whereas symmetric vibration will change the polarizability, so this vibration is Raman active.

In the case of double bonds (C=C), especially the polarizability is changed during symmetric stretching. This makes Raman spectroscopy very useful to monitor the amount of double bonds. Profiling a thin coating layer requires resolving spatial Raman information. This can be achieved by confocal Raman microscopy (CRM). In this technique a laser is focussed on or in a sample, see figure 4.1. By changing the focus to different positions inside the paint film it is possible to obtain Raman scattered light from that specific focus position. One should note that normally this technique is limited to films
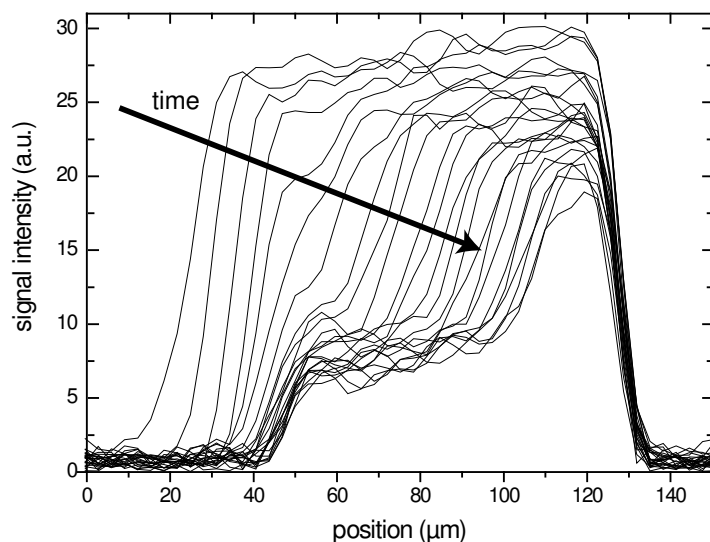
Fig. 4.2: Time and position dependence of the NMR hydrogen signal obtained from the stain
sample. Each profile results from signal integration over 10 minutes starting succes-
sively at 10, 20, 30, 50, 70, 90 and 120 min after positioning the film immediately after
casting. After the 7th profile the profiles are plotted after every 100 min. The left side
is the open side of the coating, at the right the cover glass is located.

that are transparent for IR radiation.

4.3   Experimental results

In this section we will discuss results from both NMR and Raman measurements on
two different alkyd paints. One is a commercially available organic solvent-borne stain
whereas the other is water-borne. The latter, an alkyd emulsion, was made by DSM
Coating Resins, Zwolle, The Netherlands [40]. The resin was synthesized as based on
soybean (50% regular; 50% conjugated) and phthalic acid, and chain stopped. Curing
was caused by the addition of 1% of Nuodex WEB Co 8% prior to film-casting. The
sample is cast on a cover glass of 100 μm thick. A spiral bar is used to cast a wet film of
about 200 μm. After application the paint is directly placed in the NMR setup. In the
next sections the NMR and CRM results are given. Also the weight of the sample was
measured, using an analytical balance connected to a computer.

4.3.1   Nuclear Magnetic Resonance

The measurements of the paint films were performed in a 1.4 T magnetic field with a
gradient of 36.4±0.2 T/m using an Ostroff-Waugh [109] sequence (90°_x-τ-[90°_y-τ-echo-τ]$_n$),
see chapter 3. Before each sequence a delay was added to restore the nuclear magnetization
to its initial state. In all our NMR measurements an echo spacing (2τ) of 200 μs was used.
The recording window to measure the echo had a duration of 195 μs. In all measurements
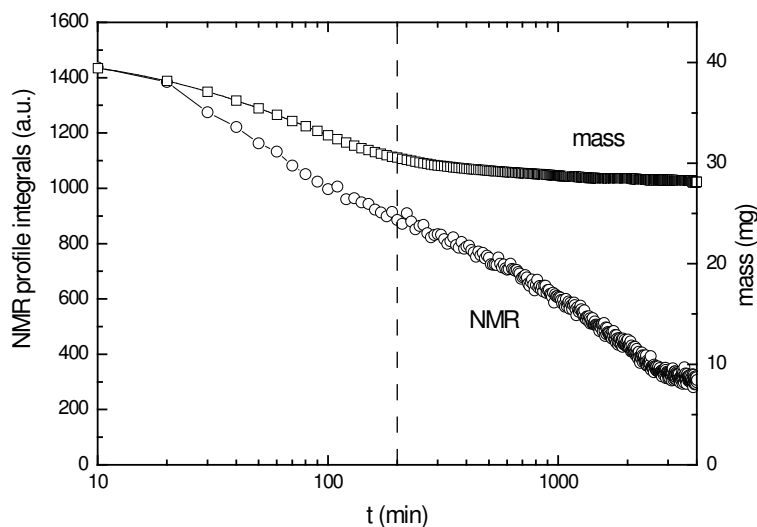
Fig. 4.3: Mass and NMR signal decrease during drying of the stain sample. The NMR signal is obtained by integrating the acquired profiles. The vertical dashed line denotes the time at which the front shown in figure 4.2 starts to move in.

the 90°-pulse had a duration of 1 μs. The spatial resolution Δy is inversely proportional to the duration of the recording window and the gradient strength. In our experiments, the duration of the recording window is limited by T_2 (this relaxation time governs the NMR signal decay). An increase of the gradient strength can be achieved by changing the pole tips of the magnet, but this would reduce the signal to noise ratio and increase the contribution of diffusion to the signal decay. With the settings given above the theoretical spatial resolution is about 3.3 μm. To approach this resolution as much as possible, the sample should be oriented perfectly horizontal in the magnetic field. To verify whether the position and orientation of the sample in the magnetic field are correct a reference sample was used. The effects of T_2 and diffusion can be assessed from the measurements on the actual paint layer.

In figure 4.2 the hydrogen signal profiles of the stain sample are shown. About 10 minutes were needed to obtain each profile, as 512 averages were taken. From the figure two stages can clearly be identified. The first profiles show that the film shrinks, this process takes about one hour. At a certain time, after the 7th profile in figure 4.2, corresponding to roughly between 2 to 3 hours, a front forms which moves towards the lower part of the coating. To explain these processes in more detail the mass a similar film sample under the same conditions was measured. In figure 4.3 this measurement is given together with integrated hydrogen signal. These integrals of the profiles in figure 4.2 reflect the total amount of hydrogen atoms inside the coating visible with NMR. The mass measurement shows that almost all mass loss occurs during the first two hours, which is also reported in [68]. The mass decrease during the first two hours is about $26 \pm 5\%$. The NMR signal decrease is $36 \pm 5\%$. The difference is most likely caused by the fact that the proton densities of the evaporating and non-volatile matter are not the same. Figure 4.2
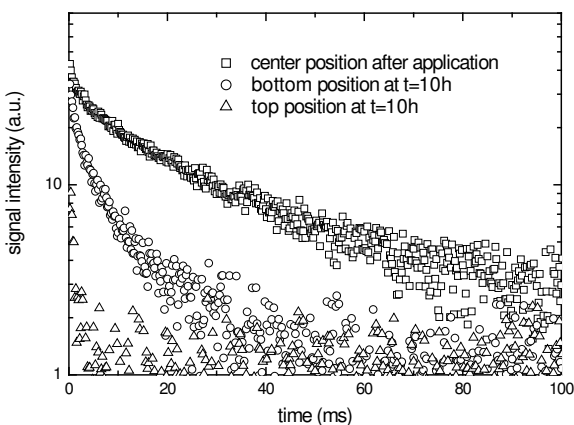
Fig. 4.4: NMR signal decay of the stain sample at $t = 0$ and 10 h.
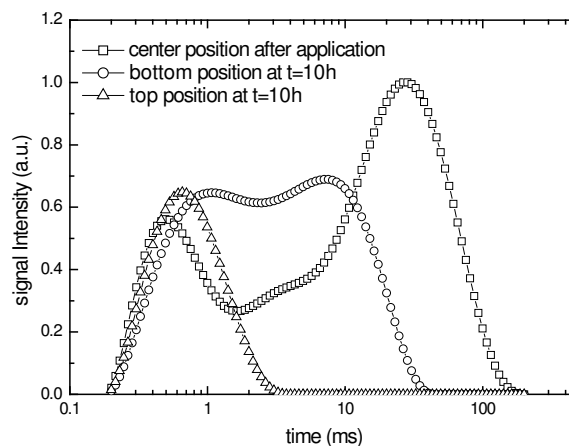
Fig. 4.5: Relaxation time distribution of the stain sample at $t = 0$ and after 10 h.

shows that between 2 to 3 hours a front forms, which starts at the top and moves down to the bottom of the coating. This corresponds with the moment in figure 4.3 after which the NMR signal continues to decrease, while the mass only slightly decreases. It seems that part of the hydrogen in the sample can no longer be detected under the experimental conditions resulting from the settings of the NMR equipment.

The NMR signal loss can be explained by analyzing the relaxation process. Figure 4.4 shows the NMR signal decay immediately after application (t = 0) and after 10 hours of drying of the stain sample. Immediately after application we notice that more than one specific relaxation time is present. After ten hours, when the front in this particular paint film is halfway through the film, the signal decay shows a different behavior. Near the top of the film the decay rate has become quite fast and seems to be mono-exponential, whereas at the bottom part of the film the decay still shows a multi-exponential behavior. In figure 4.5 the relaxation time distribution of these decay curves is shown. This relaxation time distribution is obtained by fitting the decay curves using CONTIN [113], which is a constrained regularization program for inverting algebraic equations. The NMR hydrogen signal decay rate increases during drying, which is caused by a decreased mobility of the polymers during the curing process [86] inside the paint film. Now the NMR signal loss can be understood by inspection of the decay curves and relaxation time distributions in figure 4.4 and figure 4.5, respectively. When the NMR signal decay is very fast the signal has partly decayed at the time of recording, giving a decrease of the amount of visible hydrogen atoms.

4.3.2 Confocal Raman Microscopy

Both alkyd paints have also been investigated using a Confocal Raman Microscope. A Raman spectrometer (Dilor Labram) is used with a HeNe laser at a wavelength of 632 nm. An ultra long working distance objective with a magnification 100x was used (Olympus) to focus inside the paint film. By changing the focus of the Raman Microscope to a given depth, the relevant Raman spectra of the corresponding volume element can be obtained,
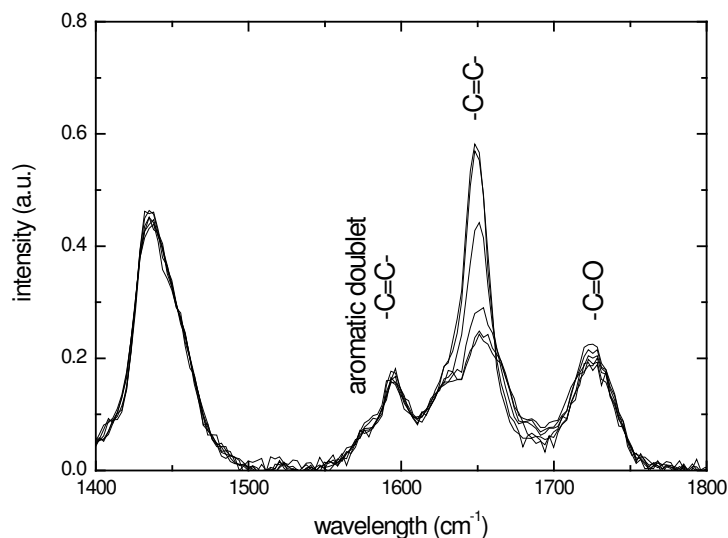
Fig. 4.6: Typical Raman spectra of the stain paint. The peaks are shown at different positions inside the film layer after about 1 day, when the front is halfway.

see figure 4.6. The actual focus is shifted due to refraction of the transparent coating [26]. The nominal position within the film should be corrected by a factor between 1.5 and 2.0 to get the actual position inside the paint layer.

In figure 4.6 Raman spectra between 1500–1800 cm^{-1} are plotted. The peak at 1600 cm^{-1} is the double bond in the aromatic ring of the phthalic acid group, the peak at 1725 cm^{-1} shows the -C=O bonds. Both peaks do not change during the cross-linking process. However, the peak at 1660 cm^{-1} shows the stretching of the double bonds in the aliphatic chains. During the curing double bonds disappear, which causes the chains to cross-link and to form a network. The density of the double bonds is obtained by dividing the peak reflecting the -C=C- bonds by a constant reference peak (figure 4.6) for every position inside the coating. This procedure implicitly corrects for the increase of the size of the effective volume element that is probed by CRM at deeper regions of the film. The decrease of the density of the double bonds is supposed to be a measure for the cross-link density. In each measurement our zero position corresponds to the focus on the top surface of the paint film. The Raman measurement was always started after the front started to move in.

4.3.3 Discussion

In this section we will compare the results from both the NMR and CRM measurements. Figure 4.7 shows NMR and CRM profiles of similar stain samples for the same times in the drying process. The fronts observed in both the NMR and CRM measurements seem to be at comparable positions inside the paint film. To check whether both techniques are actually measuring the same process one water-borne alkyd sample was used, in which the front was moving more slowly. This made it possible to measure NMR and CRM profiles
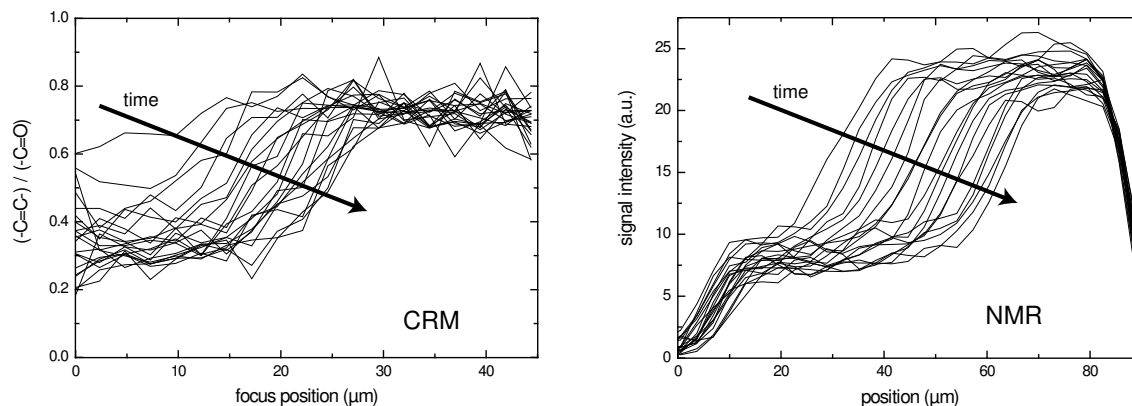
Fig. 4.7: Results for the stain sample (solvent borne alkyd). Similar samples are used, profiles are given for the same times. The first profile started at $t = 4$ h 45 min. The next profiles correspond to time intervals of one hour.
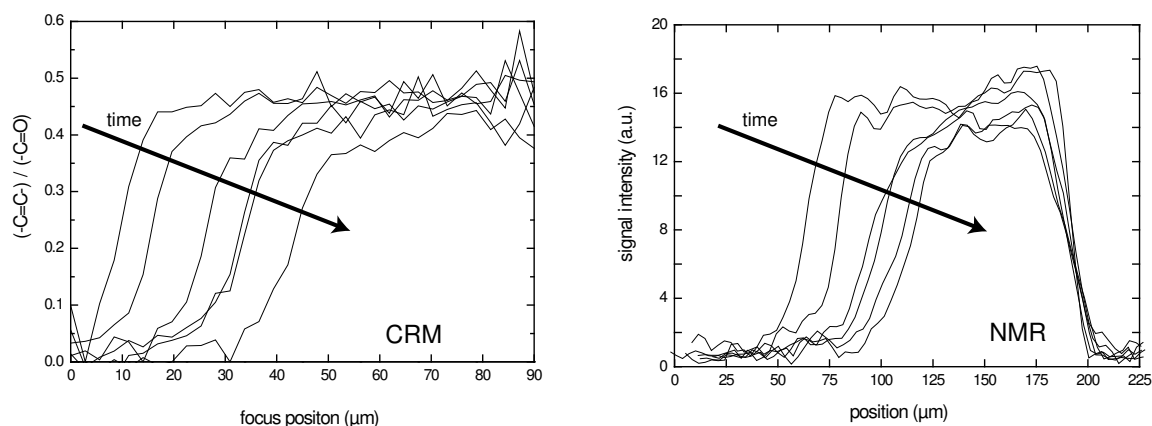
Fig. 4.8: Water-borne alkyd. Profiles of the same sample are given at approximately: 4 h, 30 h, 96 h, 150 h, 198 h, 270 h.

on the same sample alternatingly. In figure 4.8 the NMR and CRM measurements on this sample are displayed. Due to the very short NMR relaxation times in this sample the signal to noise ratio is lower. Also in this case, the front moving down into the sample seems to be at the same position in both the NMR and CRM profiles. To check this in more detail, the position of the NMR front is plotted against the corresponding position of the CRM front for several times during the drying process. The front positions of both the NMR and CRM profiles were determined from the intersection of a horizontal line positioned arbitrarily at approximately half the height of the front. The slope of this graph, which is shown in figure 4.9, gives the correction factor for the CRM position caused by refraction. This factor was found to be equal to 1.6 ± 0.2, in accordance with [26]. The intersection with the vertical axis gives the position of the top of the film in the NMR profiles, which is at 50 ± 5 μm. The small errors in the positions are unavoidable and caused by placing the sample alternatingly in the NMR and CRM setup. Apart from this, one should note that the focus of the laser has a very small spot (10 μm), probing
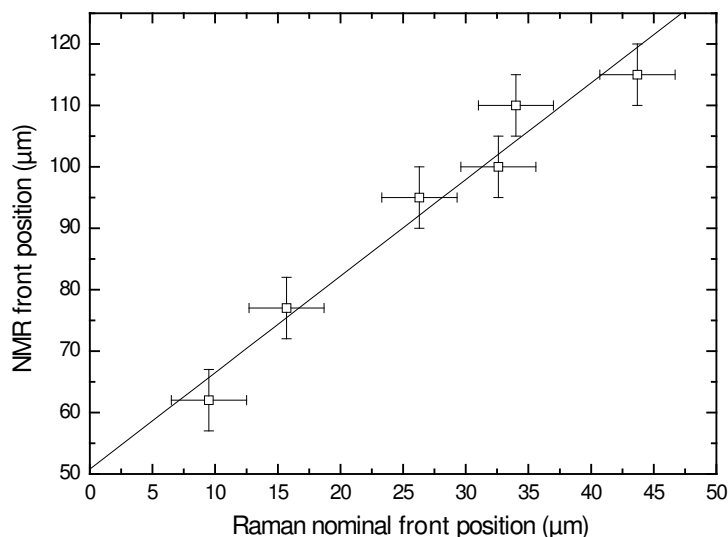
Fig. 4.9: NMR front position against nominal Raman front position.

the local thickness, whereas the NMR setup averages over a region of about 5 mm in diameter. So variations in thickness are averaged in the NMR measurements, whereas CRM gives the local thickness.

Oxygen is incorporated in the curing of the alkyd paints. The reaction mechanisms are given in [40, 49]. When reacting with oxygen, the double bonds become saturated, which explains the vanishing double bonds as observed in the Raman measurements. The fact that the NMR and CRM profiles are at the same position indicates that the cross-linking occurs immediately when the double bonds disappear. The decrease in mobility of the polymer chains, caused by the cross-linking process, results in an increased NMR signal decay rate [114]. We also observe multiple relaxation times, which was not reported by [68, 115]. In principle, these multiple relaxation times can be associated with difference in mobility of parts of the polymer chains in the network, as discussed in [114]. Such an analysis, however, is beyond the scope of this chapter.

In the present study, the position of the front gives the position at which the cross-linking occurs. This is different from what is reported by Bennett et al. [116]. The front they observed was caused by water diffusion in combination with evaporation of water at the top of the sample.

One should note that the CRM measurements (figure 4.7) indicate that in the stain sample not all double bonds disappear. Once vitrification sets in and cross-linking is significant, some of the double bonds may be difficult to reach. This also may explain that part of the hydrogen atoms in the stain sample remain detectable by NMR, because of the higher mobility of the polymer chains.

4.4   Conclusions

In the measurements presented in this chapter two stages of drying can be observed. The first is physical drying, in which the coating shrinks and the mass is decreased due to evaporation. The second is a curing stage, in which double bonds disappear while reacting with oxygen, which is shown in the Raman measurements. The NMR measurements show that disappearance of double bounds is directly related to the formation of cross-links. The cross-linking was also confirmed with Gel Permeation Chromatography (GPC) data. This causes a decrease in mobility and hence a decrease of the NMR signal, giving rise to the observed fronts in the NMR profiles. Our experiments show that NMR can in principle be used to measure the cross-linking in any nontransparent alkyd paint. Apart from this, an analysis of the relaxation behavior and diffusion effects might give information on the presence of, e.g., trapped solvents or monomers in a film.

5. Dynamics of cross-linking fronts in alkyd coatings

The dynamics of the curing process of alkyd coatings is an important aspect for coating performance. The formation of cross-links in an alkyd coating film has been followed in time using a micro imaging Nuclear Magnetic Resonance (NMR) setup, having a spatial resolution of 5 µm perpendicular to the film. During this cross-linking process a front has been observed inside the coating film. The position of this front varied with the square root of time. With the help of a simple reaction model, we have shown that this dynamics results from the fact that the curing rate is limited by the oxygen flux into the coating. This model can also explain, the differences in curing rates observed for various coatings.

5.1   Introduction

Legislation concerning the use of coatings with volatile organic components (VOC) drives coatings manufacturers to focus on the production of water-borne coatings. Much research is done to develop water-borne coatings with the same performance as their solvent-borne counterparts. An important aspect of a coating is its network structure and the development of this structure during the drying process. Techniques to probe the spatial and temporal evolution of the coating structure are essential. Most available techniques are optical techniques, e.g. confocal Raman microscopy (CRM), which can be used to obtain spatially resolved chemical information. Recently, new techniques using high spatial resolution nuclear magnetic resonance (NMR), e.g., GARField [27] have become available for research and characterization of thin layers of hydrogen containing materials. These NMR setups can be used to measure the spatial and temporal evolution of the structure of a thin coating film, with a high spatial resolution perpendicular to the film layer. A major advantage of NMR over any optical technique is that also non-transparent coatings can be imaged.

A important class of commercially available paints contain alkyd resins. These resins consist of polymers with unsaturated fatty acid side chains. In recent years the drying process of alkyd resins has been studied extensively [34, 40, 49, 68, 71, 117]. The drying process of these resins consists of two stages. First, the solvent evaporates (physical drying) and next a network is formed by chemical reactions of double bonds (curing). In previous work it has been shown that both stages can be studied with NMR [34, 68, 117]. In this chapter we study the dynamics of the observed cross-linking fronts and explain it with a simple model.

Fig. 5.1: NMR hydrogen profiles of a water-borne alkyd sample during drying. The left side is the top of the coating, at the right the cover glass is located. The vertical dashed line shows the top of the film after evaporation. The profiles are plotted for 0, 1.3, 2.5, 5, 8, 11, 26, 53, 79, 105, 132, and 158 h.

5.2   *Materials and Methods*

The measurements were performed with a micro imaging NMR setup, consisting of an electromagnet with specially shaped pole tips (GARField), generating a magnetic field of 1.4 T with a gradient of 36.4 T/m perpendicular to the coating film. The NMR pulse sequence used to obtain the hydrogen density profiles and the signal decay is an Ostroff-Waugh [109] sequence ($90°_x$-τ-[$90°_y$-τ-echo-τ]$_n$). The interecho time (2τ) used in the experiments equals 200 μs. The maximum theoretical spatial resolution is 3.3 μm. The acquisition of each profile took about 10 minutes, using 512 signal averages. The experiments were performed on two alkyd samples: a water-borne sample and a commercially available solvent-borne sample. Both coatings were cast on a 100 μm cover glass sheet, using a 200 μm spiral application rod.

The water-borne system is an emulsified alkyd resin mixed with NuoDex WebCo 8%, as a catalyst. The profiles of this water-borne sample are shown in figure 5.1. At the right edge of the profiles the glass sheet is located. The first three profiles show the evaporation stage, during which the solvent evaporates and the coating shrinks. The vertical dashed line corresponds to the position of the surface of the coating after evaporation. After this evaporation stage, a front forms and moves away from the surface of the coating towards the glass sheet. The observed front arises from a NMR signal loss due to fast signal decay in the cured regions. This corresponds to the formation of a cross-linked network, as has been proven by comparing NMR with confocal Raman Mmicroscopy (CRM) [117]. After a certain time a layer at the top of the coating has cross-linked; this layer is often called a skin.
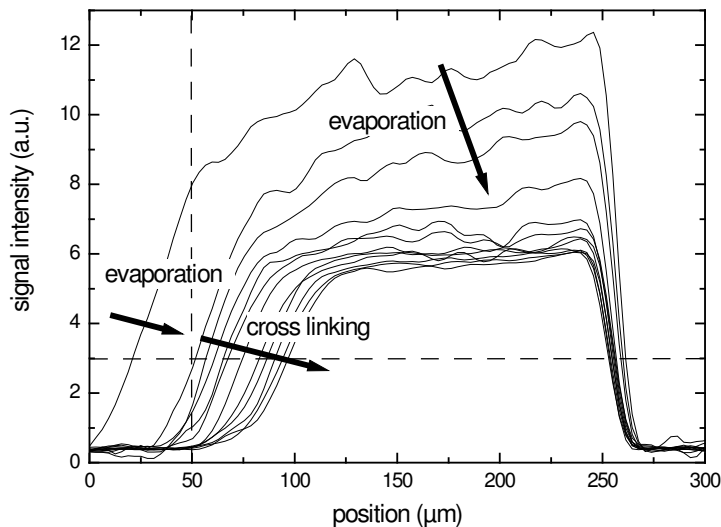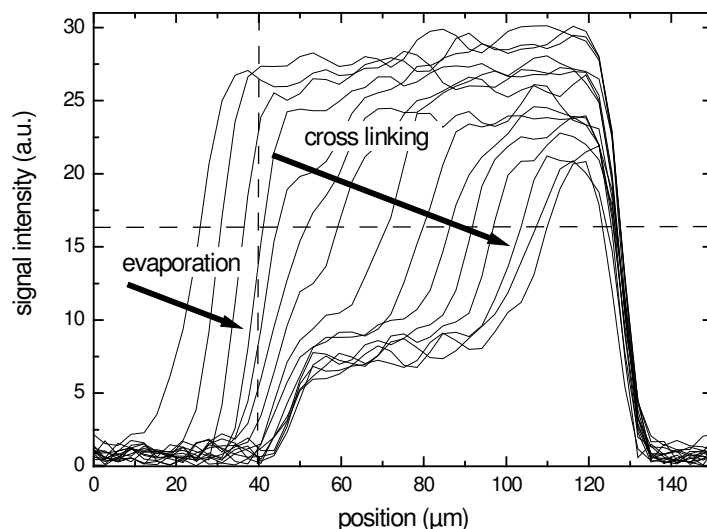
Fig. 5.2: NMR hydrogen profiles of a solvent-borne alkyd sample during drying. The left side is the top of the coating, at the right the cover glass is located. The vertical dashed line shows the top of the film after evaporation. The profiles are plotted for 10, 20, 30, 50, 70, 90, and 120 min. After the seventh profile the profiles are plotted for every 3 h 20 min.

5.3 Results and discussion

The profiles of the solvent-borne sample are shown in figure 5.2. Again the first profiles show the evaporation stage. The vertical dashed line shows the position of the surface of the coating after evaporation. Note that in this system the signal has not completely vanished after the cross-linking front has passed. This is caused by the fact that the network is not as rigid as in the water-borne sample. CRM measurements have shown that the network has indeed only partially cross-linked [117]. We will return to this observation later on.

In order to characterize the dynamics of the curing front, we have determined the front positions f from the intersections of the fronts visible in the different profiles with the horizontal dashed line. For both samples we place this horizontal dashed line arbitrarily at about half the height of the front. The moment that the front forms and starts to move into the coating we will refer to as $t = t_0$. The position of the front at $t = t_0$ is denoted by f_0. The front positions f obtained for both samples are plotted in figure 5.3 as $(f - f_0)^2$ against $t - t_0$. This figure reveals that within experimental inaccuracy the front position varies with the square root of time in both the water-borne and the solvent-borne system.

To explain this front movement $f \sim \sqrt{t - t_0}$ the following model is used. We consider a plane of thickness dx at position x within the coating film. The coating consists of unsaturated fatty acids with a certain density ρ_d of double bonds. A certain amount n of oxygen molecules are consumed per double bond during the cross-linking process, and a fraction ϕ of the bonds is used during the cross-linking process. The cross-linked
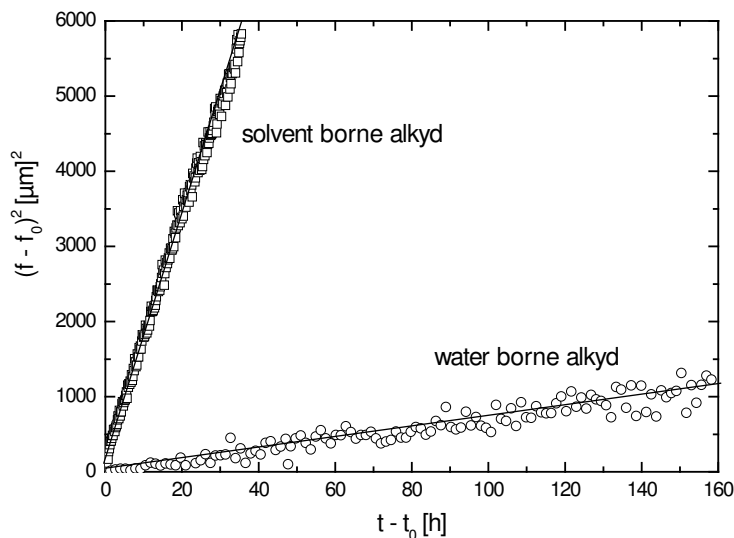
Fig. 5.3: Squared front position against time, for a solvent-borne and water-borne alkyd system.

volume per mole oxygen is given by $\nu = 1/n\phi\rho_d$. We assume that the reaction rate is very high, which means that the oxygen flux into a small layer at position x at a time t will instantaneously be used for the cross-linking reaction, until all possible oxygen reaction sites have vanished. At that moment, the front has passed this position. The speed of the front movement is therefore given by

$$\frac{df}{dt} = \nu J, \tag{5.1}$$

where J [mol/m^{2}s] is the molar flux of oxygen. The flux of oxygen in the cross-linked region is given by

$$J = -D\frac{d\rho}{dx}, \tag{5.2}$$

where D [m^2/s] and ρ [mol/m^3] are, respectively, the diffusion constant and the molar density of oxygen in the cross-linked region. Since the surface of the coating is in equilibrium with the surrounding air, the oxygen density ρ_0 in the surface layer of the coating film will be constant. Because we assumed that at the front all oxygen is consumed instantaneously, the oxygen density equals zero at the front. Furthermore, we assume that the oxygen flux is constant in the cross-linked region. This assumption is valid because the amount of oxygen lost in this region is negligible. In addition, the oxygen distribution is assumed to adapt itself immediately to changes of the front position, resulting in a quasi-steady state approach for the oxygen distribution. With these assumptions the oxygen density linearly decreases over the cross-linked region, see the schematic diagram of our model in figure 5.4. Equation 5.2 can now be rewritten as

$$J = D\frac{\rho_0}{f(t) - f_0}. \tag{5.3}$$
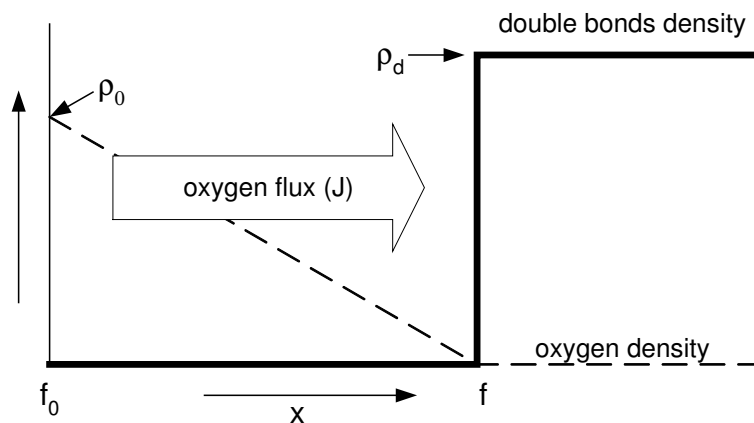
Fig. 5.4: Schematic representation of the drying model. The dashed line indicates the oxygen density. The black line indicates the amount of double bonds. At the curing front the oxygen density is zero, due to the high reaction rate.

When equations 5.1 and 5.3 are combined, the following expression for the front position can be obtained:

$$f(t) = f_0 + \sqrt{2\nu D\rho_0(t - t_0)}. \tag{5.4}$$

This equation is in agreement with the observed behavior. This suggests that the oxygen supply is indeed the key factor limiting the rate of the curing process, and not the capacity of the catalyst.

To check this model we have performed an experiment in which the oxygen supply was limited by creating an argon atmosphere above the coating film. The results of this experiment are shown in figure 5.5. At $t - t_0 = 18$ h essentially all oxygen was removed above the film. The front stops, which indicates that the chemical reaction stops. It appears that only a few minutes are needed to deplete the oxygen inside the cross-linked region. This justifies the quasi-steady state approach for the oxygen distribution. When 22 h later ($t - t_0 = 40$ h) the argon atmosphere is removed and the air atmosphere is restored, the front movement returns to its original speed. This experiment demonstrates that oxygen supply is the limiting factor for the reaction and proves the validity of our model.

Equation 5.4 also explains the higher front speed of the solvent-borne coating compared to water-borne coating, see figure 5.3. The difference of oxygen density in the surface layer ρ_0 between both coating systems is expected to be small. However, the diffusion coefficient and cross-linked volume per mole oxygen vary significantly. One expects an increase of the diffusion constant in a system with a higher polymer mobility in the polymer matrix, which is the case for the solvent-borne system compared to the water-borne system. As we have already noted, the NMR signal from the solvent-borne sample remaining after cross-linking indicates this higher mobility. Furthermore, this solvent-borne system was observed to have a smaller fraction ϕ of double bonds used during the cross-linking process [117], which also indicates a higher polymer mobility. Since less double bonds have cross-linked, the cross-linked volume per mole oxygen ν is also higher. Hence, the factor $\nu D\rho_0$
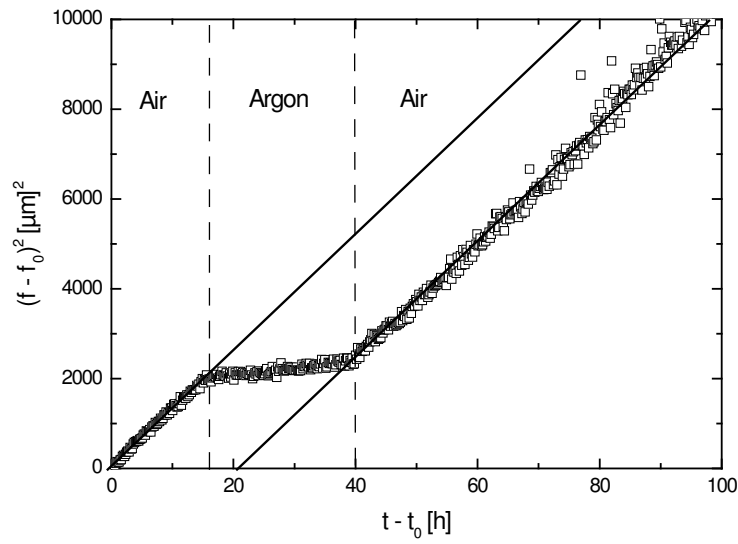
Fig. 5.5: Squared front position against time for the solvent-borne alkyd system. After 18 h of drying an argon atmosphere was created above the film. At $t = 40$ h the air atmosphere was restored.

(Eq. 5.4) is higher in the solvent-borne system, which agrees with the higher curing rate, observed in figure 5.3. This shows that our model can also be used to explain the difference in curing rates of coatings which are limited by oxygen diffusion.

6. Curing processes in solvent-borne alkyd coatings with different drier combinations

The concern regarding the effect of chemicals on the environment has increased considerably in recent years. Nowadays, technological developments in the coating industry are largely influenced by environmental issues and corresponding legislation. One of these issues is the tendency to replace cobalt as a catalyst with more environmentally friendly alternatives, because studies have indicated possible carcinogenicity. Not much knowledge is available on the effects of catalysts (driers) on the in-depth drying of alkyd coatings. Therefore we have studied the effect of cobalt as a primary drier combined with Ca and Zr as secondary driers on the in-depth curing of high solid solvent-borne alkyds. The profiling of the curing of alkyd coatings is performed with a new high spatial resolution Nuclear Magnetic Resonance (NMR) setup. In this study, two effects observed in the solvent-borne alkyd coatings are investigated. One is that when Ca and Zr are added as secondary driers, the speed of the observed cross-linking front increases. Second, in the deeper uncross-linked region below the front, the signal of the NMR profiles was found to decrease proportional to $\sqrt{t}$. This could be explained by the presence of slowly reacting species that diffuse into the deeper uncured region of the coating after which they cross-link. The model describing the effect of these reactive species also indicates that the signal decrease is inversely proportional to coating thickness L, which was confirmed by additional measurements.

6.1 Introduction

Coatings can be found everywhere, e.g. on furniture, cars, airplanes and buildings. An important class of coatings are the ones based on alkyd resins. In 1996 the European coating industry consumed 1.8 million tonnes of binders for the production of paints, of which 25 % were alkyds [4]. The curing of alkyd coatings is a complex autoxidation process [42–45]. By the addition of so-called driers this process can be accelerated considerably. Cobalt is the most commonly used drier in commercial alkyd paints. In most commercially available coatings secondary driers (Ca and Zr) are added to Co to enhance the oxidation. In the literature various statements circulate about the effects of the addition of Ca and Zr [19, 54, 62–64, 68]. As an example, Zr is said to improve the through-drying, i.e., drying in the deeper layers of the coating. Up untill now, however, the knowledge on the effects of driers on the in-depth drying of coatings is still rather limited. In this paper we will focus on the effect of Ca/Zr as secondary driers on the in-depth drying of solvent-borne

alkyd coatings.

Only few analytical techniques are available that can probe the coating structure as a function of time. One of these techniques is Confocal Raman Microscopy (CRM), in which the chemical changes can be probed locally, e.g., the change in double bonds [23, 24, 26, 118–120]. In this study we use a high spatial resolution Nuclear Magnetic Resonance (NMR) setup. This setup has the ability to probe in a non invasive way non transparent coating systems with a spatial resolution of about 5 μm [27]. The NMR setup measures the hydrogen density profiles and the local mobility of the hydrogen nuclei inside the coating by probing the signal decay. During the drying process the mobility decreases and the signal decay increases, allowing the drying process to be visualized.

In section 6.2 we first review the drying process of alkyd resins and the effects of driers on this process. In the following section (section 6.3) the materials and methods are further explained. The measurements will be discussed in section 6.4. In section 6.5 we introduce a model to explain in more detail the measurements in which drying in deeper regions of the coating is observed. Finally we end with the discussion and conclusions.

6.2   Drying of alkyd coatings

The drying process of an alkyd coating can be divided into two stages. The first stage is a physical drying stage in which the solvent evaporates. The second stage is a curing stage (chemical or oxidative drying) in which the resin of the coating reacts and forms a network. These two stages involve different time scales: the evaporation stage takes minutes to several hours, whereas the curing process takes place over several hours to days, or even months. This last stage can continue slowly for years. In this paper we will focus on the second stage, the curing stage.

The curing of alkyd coatings is a lipid autoxidation process [42–50]. Autoxidation is generally divided into six stages [39, 52, 53]. The stages that are distinguished are the induction period, the initiation, hydroperoxide formation and decomposition, followed by cross-linking and degradation. Many possible intermediate and final species can be found during this complex autoxidation process [43, 44].

The autoxidation process is a slow process and driers are needed to increase the speed of this process [53]. These driers enhance the decomposition and/or formation of the hydroperoxides, finally resulting in a speedup amount of radicals. In general, drier metals are divided into two categories [19, 54, 62–64]: primary driers (active driers) and secondary driers (through driers). The first group, the primary driers (in this paper this group is referred to as the catalyst), is said to promote rapid surface drying with limited through-drying properties. Cobalt, manganese and iron belong to this group. The second group, the secondary or auxiliary driers, is assumed to have two effects: they are said to increase the stability of the primary drier and promote the through-drying. Many different effects have been reported for many different driers and drier combinations and concentrations in model systems [19, 68, 70]. In a paper by Mallegol et al. [68] the influence of drier combinations on the through-drying in waterborne alkyd emulsions was investigated by analyzing the T_2-relaxation times obtained using an NMR profiling setup. They concluded

that more uniform cross-linking is achieved using a combination of Co, Ca and Zr. In this paper the dynamics of the curing process will be studied in more detail.

6.3   Materials and Methods

6.3.1   Materials

The high-solid solvent-borne alkyd resin used has a solid content of about 80% and a oil length of 79%. The cobalt concentration used was 0.06% mass/mass with respect to the solid content. The concentration of Ca was 0.23% mass/mass and that of Zr was 0.38% mass/mass when added. The coatings were supplied by Akzo Nobel. The coatings were applied on a microscope cover glass using a 150 μm spiral application rod resulting in a dry film thickness of about 90 μm.

6.3.2   NMR setup
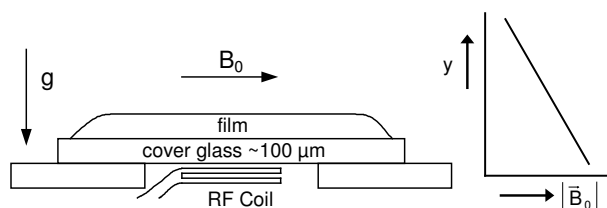
Fig. 6.1: Schematic representation of the RF coil and film placement inside the magnet. The right graph shows the variation of the magnetic field as a function of position inside the coating. Because of this gradient (36 T/m) a resolution of about 5 μm in the vertical direction can be achieved.

A high resolution NMR setup is used for profiling the curing of the coatings. The working principle of this setup is based on the fact that magnetic nuclei located in a magnetic field can be selectively excited by a radio frequency (RF) pulse. The resonance frequency (f) depends linearly on the applied magnetic field (B), $f = \gamma|\vec{B}|$, with γ the gyromagnetic ratio (for hydrogen nuclei, $\gamma = 42.58$ MHz/T). To obtain a high spatial resolution (approximately 5 μm) a very high magnetic field gradient should be applied. To achieve this the magnitude, of the magnetic field is varied with position, $f = \gamma(|\vec{B}|+G\cdot y)$, where $G = \partial|\vec{B}|/\partial y$, according to the GARField design introduced by Glover et al. [27]. The sample can be placed directly on top of a surface coil, as shown in figure 6.1, which gives a good signal to noise ratio. Also the gravity is perpendicular to the applied paint film, which makes it possible to measure wet films. In our study we use an NMR setup that contains an electromagnet generating a magnetic field of 1.4 T at the position of the sample. The gradient is 36.4 ± 0.2 T/m.

The NMR pulse sequence used to obtain the hydrogen density profiles and the signal decay is an Ostroff-Waugh [109] sequence (90°_x-τ-[90°_y-τ-echo-τ]$_n$), see chapter 3. The inter-echo time (2τ) was set to 200 μs. From the signal decay acquired by this pulse
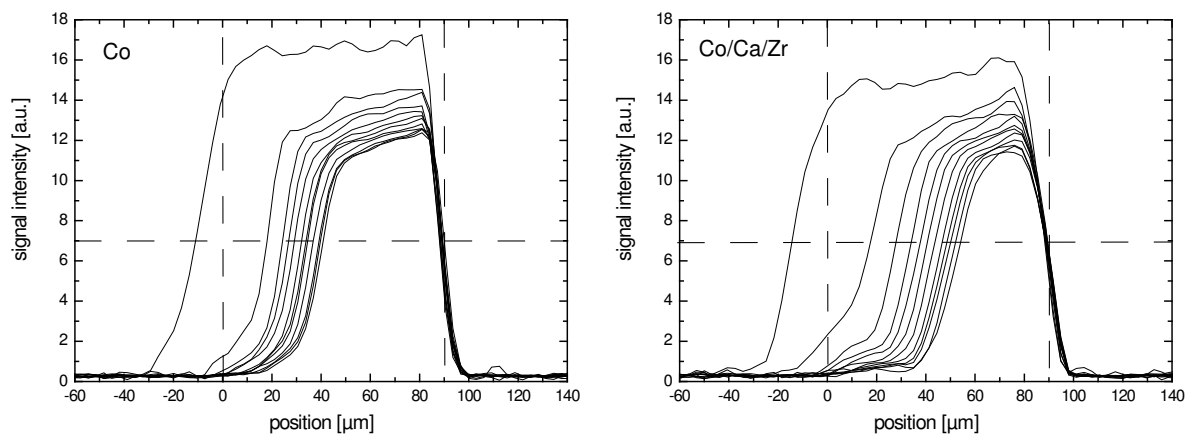
Fig. 6.2: NMR signal intensity measured as a function of position inside the coating at different times, for both Co and Co/Ca/Zr as a catalyst. The glass plate is located at the right side of the coating, indicated by the right vertical dashed line. The left dashed line shows the top of the coating. In both graphs the first profile is given during the evaporation of the solvent, $t = 0.6$ h. The second profile in both graphs is plotted for $t = 5.6$ h and then every 6.3 h. The point of intersection of horizontal dashed line with the left side of the profiles is taken as the position of the front.

sequence several T_2-relaxation times can be obtained, depending on the average local mobility [117].

6.4   Results

6.4.1   Profiles

In figure 6.2 profiles of the alkyd coatings for both Co and Co/Ca/Zr as driers are shown. The profiles were acquired approximately every 20 minutes, however, only several representative profiles, after interpolation over all profiles to reduce the noise, are plotted. The first profile shows the coating after 0.6 h, during the evaporation stage. The left vertical dashed line indicates the position of the surface of the coating after the evaporation of the solvent. The right vertical dashed line indicates the location of the cover glass sheet on which the coating was cast. After the evaporation stage a front forms and moves downward to the bottom of the coating. In previous work we have shown that this front is a cross-linking front [117, 121]. Figure 6.2 clearly shows the formation of a front. Another observation that can be made in this figure is the decrease of the NMR signal in the region where the curing front has not yet passed. This observation will be discussed in section 6.4.3, but first we will focus on the formation and behavior of the curing front.

6.4.2   Drying front

In a recent paper we observed that an oxygen gradient is present and as a result of this gradient we observed a cross-linking front [121]. This front, resulting in a skin layer, was
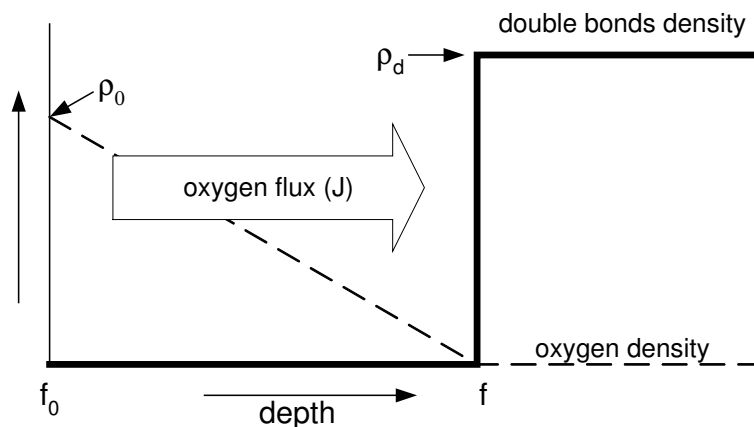
Fig. 6.3: Schematic representation of the drying model. The dashed line indicates the oxygen density. The black line indicates the amount of double bonds. Because of the high reaction rate the oxygen density is taken to be zero at the front.

observed in waterborne alkyd emulsions, solvent-borne alkyds and high solid solvent-borne alkyds, only when cobalt was used as a catalyst. The diffusion of oxygen together with a high reaction rate is the basis of the formation and movement of the front. Whenever cross-linking occurs, the NMR signal decay is so fast that part of the signal is already lost at the moment of the acquisition of the profile, making the front visible in the NMR profiles [117]. The formation of this skin layer is schematically depicted in figure 6.3. At the surface the oxygen concentration is constant, and the oxygen diffuses and is consumed at the cross-linking front to form a network. It is assumed that the oxygen reacts instantaneously, causing the front to move toward the coating substrate. This behavior can be described by the following equation [121]

$$f(t) = f_0 + \sqrt{2\nu D\rho_0(t - t_0)}, \tag{6.1}$$

where D [m^2/s] is the diffusion constant of oxygen in the coating, ρ_0 [mol/m^3] the oxygen density in the surface layer of the coating film, and ν [m^3/mol] the cross-linked volume per mole of oxygen.

In figure 6.4 the front position is plotted squared against time, which according to equation 6.1 should result in straight lines. The front positions are determined from the intersection of the horizontal dashed line in figure 6.2 with the front. This horizontal dashed line is positioned arbitrarily at approximately half of the height of the front. Figure 6.4 shows that the front movement is faster when Ca and Zr are present next to Co. Within the model a change in front speed can only be explained from the three parameters in equation 6.1, the oxygen solubility ρ_0, the oxygen diffusion D, or the cross-linked volume per mole of oxygen ν. If the network structure changes, the amount of oxygen per cross-linked volume (ν) is expected to change. To check whether the network of both coatings differs, the glass transition temperature was determined after the coatings were fully cured. The glass transition temperature (T_g) and the width of the glass transition was found to be the same within the experimental error (13 ± 2 °C and 11 ± 2°C for Co and Co/Ca/Zr, respectively). From this observation it can be expected that no significant
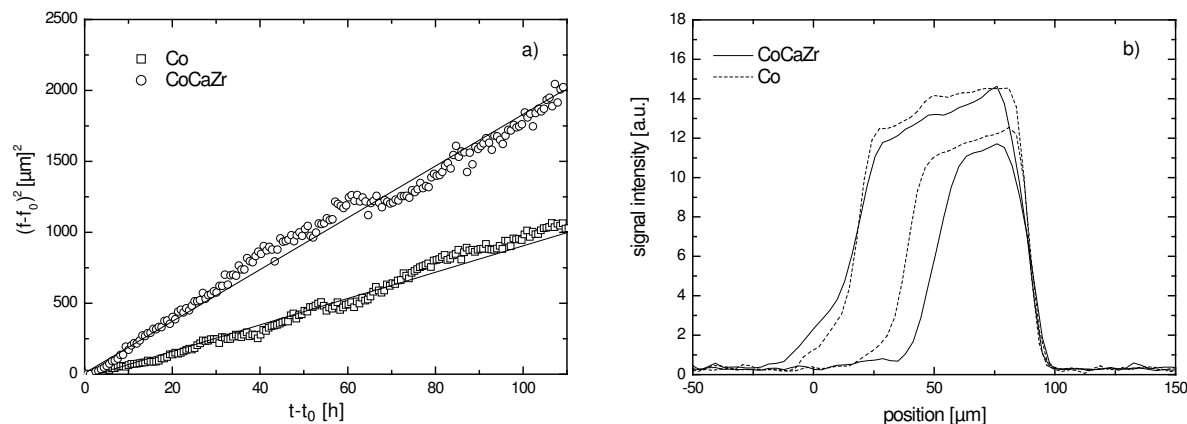
Fig. 6.4: a) Squared front position plotted as a function of time for both Co and Co/Ca/Zr as driers. b) NMR profiles of a coating with Co and a coating with Co/Ca/Zr as driers at 6 h and 60 h after application. Both figures indicate a faster front movement for the Co/Ca/Zr combination.

differences in the network structure are present, meaning no change in ν is expected. Then the other two possibilities remain, which are a change in oxygen solubility at the surface of the coating or a change of the diffusion of oxygen. Further investigations are necessary to clarify this point.

6.4.3   Curing in deeper regions of the coating

From the NMR profiles in figure 6.2 we have observed that the signal decreases in the deeper uncross-linked regions below the cross-linking front. This decrease is small and occurs fairly homogeneously at the substrate side of the front. Plots of the signal intensity in this region against the square root of time result in straight lines, see figure 6.5. Note that the signal intensity is normalized to be able to compare different samples. The signal intensity is only plotted for one position in the deeper regions of the coating, however, the observed behavior applies to the whole uncross-linked region. Additionally, the results for the samples with or without Ca and Zr show no difference in signal decrease. There are two possible explanations for a signal decrease proportional to $\sqrt{t}$. One is that remaining solvent is slowly evaporating from the coating or, second, somehow cross-linking in the deeper regions takes place.

First, let us consider the first explanation. When the thickness of the skin layer increases, it blocks the evaporation of the solvent by the increased resistance of this cross-linked layer. Because the thickness of this resistive layer increases with $\sqrt{t}$, the rate of solvent loss decreases with $\sqrt{t}$. Integration results in a solvent loss (and thus signal decrease) proportional to $\sqrt{t}$. If we would stop the front movement and let the evaporation continue, then the signal from the deeper regions would continue to decrease. Because now
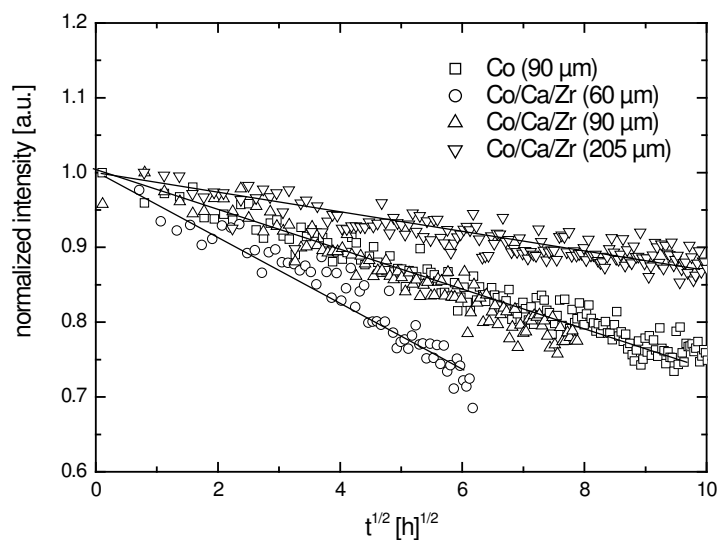
Fig. 6.5: Normalized NMR signal at one position in the deeper region, below the cross-linking front, of the coating as a function of the square root of the curing time. Note that the NMR signal intensity decreases faster for thinner coatings. For both drier combinations (Co and Co/Ca/Zr) with a similar coating thickness the signal intensity decreases at the same rate.
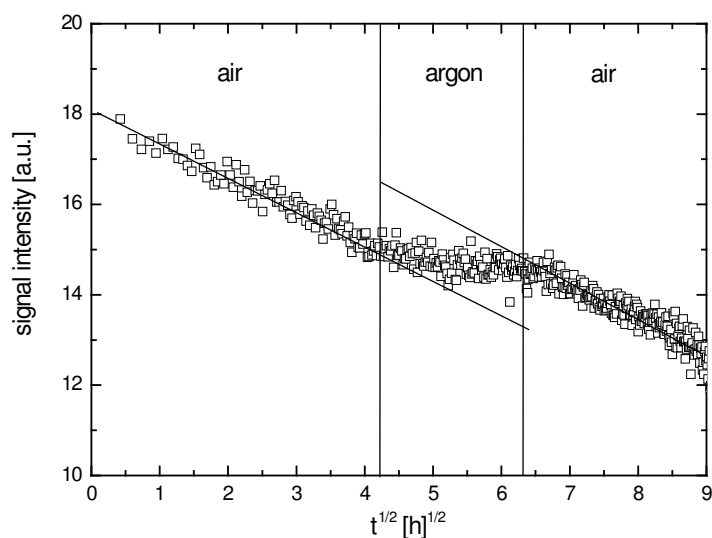
Fig. 6.6: Normalized NMR signal at one position in the deeper region, below the cross-linking front, of the coating as a function of the square root of the curing time. While the argon atmosphere is applied the signal decrease stops.

the thickness of the cross-linked layer would stop increasing, a signal decrease faster than $\sqrt{t}$ would occur. In a previous measurement on a solvent-borne alkyd the front movement was stopped by replacing the oxygen with a dry argon atmosphere around the coating [121]. In that experiment the signal in the deeper layers also showed a $\sqrt{t}$ behavior, see figure 6.6. At $t = 16$ h the argon atmosphere was created and the signal decrease stops, after restoring the air atmosphere the signal in the deeper layers decreases again. A signal decrease faster than $\sqrt{t}$ is not observed, but instead the signal decrease stops, ruling out this explanation. The second explanation, based on the diffusion of reactive species into the deeper regions, remains. This possibility is investigated in the next section.

6.5 Model

As has been shown in the previous section, cross-linking in the deeper regions is related to the oxygen flux, because removal of the oxygen supply above the coating stops the signal decrease. Therefore we assume that the flux of oxygen partially results in fast moving reactive species (high diffusion). These species are slowly reacting, resulting in a homogeneous distribution. The production of these reactive species is equal to $c_1 J$, where c_1 is the fraction of the oxygen influx that is used to create these species. The following differential equation describes the density ρ_r of these species

$$\frac{\partial \rho_r}{\partial t} = \frac{c_1 J}{L} - k\rho_r, \tag{6.2}$$

where J is the oxygen flux, L the thickness of the coating, and k the reaction constant for these species. By insertion of the equation for the oxygen flux $J = D\rho_0/f(t)$ [121], where $f(t)$ is defined by equation 6.1 with $f(0) = 0$ and $t_0 = 0$, the following equation is obtained:

$$\frac{\partial \rho_r}{\partial t} = \frac{c_1}{L}\sqrt{\frac{\rho_o D}{2\nu t}} - k\rho_r. \tag{6.3}$$

To allow the slowly reactive species to distribute homogeneously, the reaction time should be much higher than the diffusion time, $\tau_r/\tau_D = D/L^2 k \gg 1$. From the experiment shown in figure 6.6, the time to stop the signal decrease can be estimated to be about half an hour, which means that k is on the order of 10^{-3} s^{-1}. Taking typical constants for the thickness this means $D > L^2 k = (10^{-4})^2 10^{-3} = 10^{-11}$ m^2/s, which is reasonable for the diffusion constant of these reactive species in the uncross-linked area. Whether this condition holds in the cross-linked area is unclear. At the start of the curing process the production of reactive species is high, and equation 6.3 is governed by the first term at the right hand side. From this equation it can be derived that initially $\frac{\partial \rho_r}{\partial t}/\rho_r$ varies with t^{-1}, meaning that the relative contribution of $\partial \rho_r/\partial t$ decreases. Finally, at sufficiently long times a steady state situation develops and equation 6.3 can be approximated by

$$k\rho_r = \frac{c_1}{L}\sqrt{\frac{\rho_0 D}{2\nu t}}. \tag{6.4}$$

Now we assume that the signal decreases proportional to the reaction rate of the species. This assumption is based on the idea that when such a species reacts and forms a cross-link, the mobility of the surrounding hydrogens decrease dramatically, reducing their
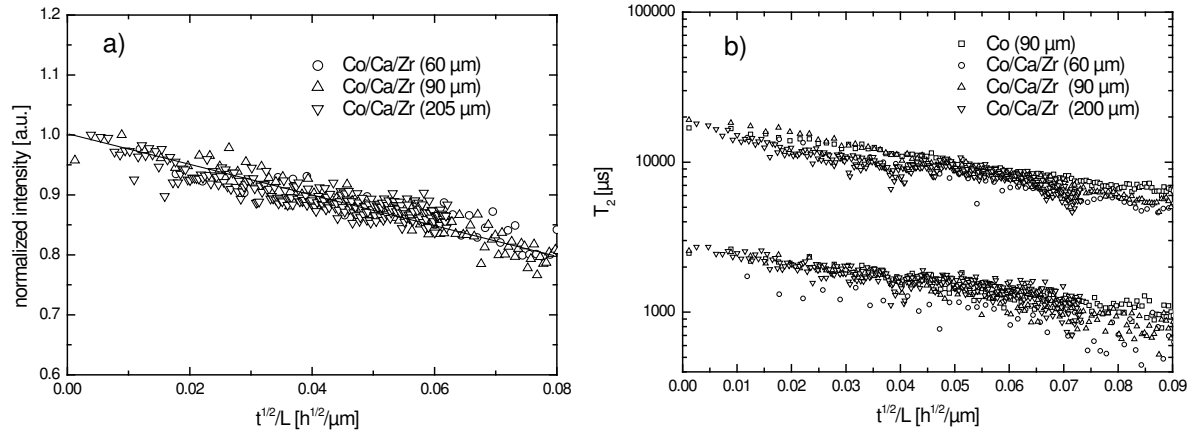
Fig. 6.7: a) Normalized NMR signal intensity as a function of $\sqrt{t}/L$ for the Co/Ca/Zr drier combinations for three different coating thicknesses. b) Two T_2-relaxation times obtained from the signal decay as a function of $\sqrt{t}/L$ for the different drier combinations and coating thicknesses. Both figures indicate that the same scaling law applies.

contribution to the NMR signal. This results in the following equation for the signal loss

$$\frac{dS(t)}{dt} = -\chi k \rho_r = -\frac{\chi c_1}{L}\sqrt{\frac{\rho_0 D}{2\nu t}}, \tag{6.5}$$

where χ is the proportionality constant between the signal decrease and the amount of reactions that have occurred. Starting from a signal $S(0)$ the following equation is obtained:

$$S(t) = S(0) - \frac{\chi c_1}{L}\sqrt{\frac{2\rho_0 D}{\nu}}t = S(0) - \frac{\chi c_1}{\nu L}f(t). \tag{6.6}$$

This equation indicates that the signal decay in the deeper region of the coating proceeds faster in thinner coatings. The model predicts that the time is scalable with L^{-1}, which is supported by the experimental data plotted in figure 6.7a. When the T_2-relaxation times obtained from the signal decay in the deeper regions for all measured coatings are plotted against $\sqrt{t}/L$, they show a similar behavior (fig. 6.7b).

The present model correctly describes the signal decrease with $\sqrt{t}$ and has correctly predicted its dependence on the coating thickness. Therefore we conclude that the diffusion of reactive species is the origin of the observed effects. The fact that this phenomenon is only observed in solvent-borne systems and not in waterborne alkyd emulsions [117] can also be explained by the diffusion of the reactive species. The diffusion is restricted in waterborne systems, which have a viscosity that is substantially higher than that of solvent-borne systems after evaporation of the water or solvent.

6.6   Conclusions and discussion

We have observed that the addition of Ca/Zr as secondary driers, next to Co as a primary drier, results in an increased speed of the curing front. Also a signal decrease in the deeper regions of the coating proportional to $\sqrt{t}$ was observed. Addition of Ca and Zr did not change the signal decrease in the deeper regions of the coating. Contrary to statements in the literature, we do not observe an increase of the through-drying by the addition of Ca and Zr [19, 54, 62–64], only a faster growth of the skin layer (a higher front-speed) is observed. Two probable explanations for the signal decrease in the deeper regions were investigated. One explanation based on the evaporation of the remaining solvent was rejected, based on additional experiments. The other explanation is based on the diffusion of low reactive species. The low reactivity of these species allows penetration in the deeper regions of the coating, after which they react and cross-link. A model describing this process correctly predicts the observed $\sqrt{t}$ behavior of the signal decrease. This model also predicts that the signal decrease scales inversely with the thickness of the coating (L). The scaling with $\sqrt{t}/L$ was experimentally confirmed by changing the coating thickness.

7. Influence of catalyst type on the curing process and network structure of alkyd coatings

Recent studies have shown that cobalt catalysts, used for curing of alkyd coatings, are potentially carcinogenic, and hence replacement by new environmental friendly catalysts is needed. The influence of different metal based catalysts on the oxidation process has been studied extensively in model systems, consisting of unsaturated oils. However, these results may not be representative for real coatings, since in these systems the oxygen diffusion is much lower than in model systems and therefore may have a large effect on the curing. In this paper we will show how the curing of an alkyd coating depends on the type of catalyst (cobalt or manganese based). The curing process is studied using a high spatial resolution Nuclear Magnetic Resonance (NMR) setup. The final network structure and cross-link density are found to be correlated with the catalyst used, i.e., a cobalt based catalyst and two manganese based catalysts. The difference in final network structure is investigated by NMR T_2 relaxation analysis and the glass transition temperature T_g measured using a differential scanning calorimeter (DSC). In case of the cobalt based catalyst a cross-linking front was observed and a high cross-link density was found, compared to the manganese based catalysts, in which case no sharp cross-linking front was observed. To interpret the observed NMR profiles in more detail, simulations based on a reaction-diffusion model were performed. From the results of these simulations estimates were obtained for the reaction constants and the diffusion of oxygen for the different catalysts.

7.1   Introduction

In the past twenty years the concerns regarding the effect of chemicals on the environment have increased considerably. Recent studies have shown that cobalt, commonly used as a catalyst in alkyd coatings, is potentially carcinogenic [16–18]. Hence there is a tendency to replace this traditional catalyst by more environmental friendly ones in the near future. However, a change of catalyst in an alkyd coating has an impact not only on the chemical reactions taking place, but also on the curing behavior and the final network structure, as we will show in this paper. In order to find suitable alternatives the precise effects of the catalyst on the curing process have to be understood.

The research on curing of alkyd focusses on three aspects. First, the autoxidation processes of unsaturated fatty acids is studied in model systems [43, 44, 47, 48]. Autoxidation is a very slow process in which various chemical species are formed while reacting with oxygen. The model systems that are investigated are usually oils, which remain liq-

uid even after oxidation. The second area of interest deals with the influence of different catalysts, e.g., cobalt (Co) or manganese (Mn) based catalysts, on the oxidation process of these model systems [19, 49, 67, 68, 71, 72]. The catalyst accelerates the formation of hydroperoxides and their decomposition into radical species. The cross-linking is driven by the reaction of these radicals. These investigations have led to valuable information concerning the chemical processes. The third area of interest deals with real alkyd coatings. In coating films an additional problem arises, which is the diffusion of oxygen. In contrast to model systems, in which the diffusion of oxygen is high because of the low viscosity and, therefore, does not affect the curing, the curing process of a coating film is influenced by the oxygen diffusion. The oxygen diffusion may limit the curing process of the coating and as a result it may influence the curing time and even the final hardness. The actual curing process in a coating is the topic of this paper. This topic is of interest for coating manufacturers, because it directly links changes on molecular scale to the final coating and, consequently, to the product performance.

Recently, various techniques have become available to follow the curing process of a coating film in time with a high spatial resolution. One of these techniques is Confocal Raman microscopy (CRM) in which the chemical changes can be probed locally, e.g., the change in double bonds [23, 24, 26]. Further, a Nuclear Magnetic Resonance (NMR) setup has been developed with the ability to perform non invasive depth profiling of non-transparent coating systems, with a resolution of about 5 μm [27]. This technique measures the density and mobility of the hydrogen nuclei, which can be obtained from the signal intensity and signal decay, respectively. The mobility of the polymers, and hence the mobility of the hydrogen atoms, decreases when polymers cross-link and form a network.

These two techniques allow the film formation process of alkyd coatings to be studied in more detail. This film formation or drying process can be divided into two stages. The first stage is a physical drying stage in which the solvent evaporates. This stage was studied extensively with high spatial resolution NMR [34, 35, 38]. The second stage is a curing (chemical drying) stage, in which the double bonds of the alkyd molecules vanish and cross-linking occurs. Using a high spatial resolution NMR setup the curing was studied by Mallegol et al. [68] for different drier combinations. As a primary drier (catalyst) cobalt was used, and as secondary driers Ca and Zr were used. They analyzed the curing process using the signal decay measured at three different positions inside the coating. In a previous paper NMR and CRM results were used to interpret the relation between the NMR data and the chemical processes, see chapter 4 [121]. This study showed that the front observed because of the reaction of double bonds is directly related to the formation of cross-links. These experiments showed that NMR can be used to follow the cross-linking in non-transparent alkyd coatings. In a later study, the observed curing fronts were explained by a model that assumes that the curing process is limited by the oxygen diffusion towards the front, see chapter 5 [117].

In this paper we will address the influence of two different manganese (Mn) and one cobalt (Co) based catalyst on the film formation process and the final network structure. First, the experimental details will be outlined in section 7.2. Next, the results of the NMR measurements will be presented and discussed in section 7.3. In section 7.4 the

data will be explained in more detail in terms of a reaction-diffusion model, and also the final network structure is discussed. Finally, the paper is concluded with a discussion in section 7.5.

7.2 Experimental details

7.2.1 Materials

The measurements were performed on a water-borne alkyd emulsion with different catalysts. The alkyd emulsion used was made by DSM Coating Resins, Zwolle, The Netherlands [40]. The resin was synthesized based on soybean (50% regular; 50% conjugated) and phtalic acid. The curing was accelerated by the addition of a catalyst (either Nuodex WebCo 8%, Nuodex WebMn 9%, or MnMeTACN) to the emulsion (50% water and 50% oil) prior to film-casting. MnMeTACN is a di-centered manganese-based catalyst, that is a potential alternative for cobalt containing catalysts. It has been reported that MnMeTACN acts as a highly effective catalyst during the oxidation of alkyd molecules [72, 122]. The samples were cast on a 100 μm thick microscope cover glass. A spiral bar was used to cast a wet film with a thickness of about 200 μm. After application, the coating was directly placed in the NMR setup.

7.2.2 NMR setup
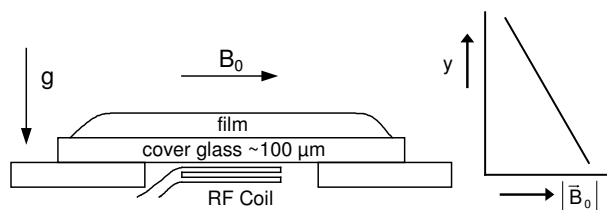
Fig. 7.1: RF coil and film placement in a high magnetic field gradient.

Magnetic Resonance Imaging (MRI) is a well known NMR technique for making images of the human body. Its principle is based on the fact that magnetic nuclei located in a magnetic field have a specific resonance frequency, and can be excited by a radio frequency (RF) pulse. The resonance frequency f depends linearly on the magnitude of the applied magnetic field $\vec{B}$, $f = \gamma|\vec{B}|$, with γ the gyromagnetic ratio (for hydrogen nuclei, $\gamma = 42.58$ MHz/T). To obtain one dimensional (1D) profiles perpendicular to the film plane, the magnetic field should only vary with position in the y-direction, $B = B_0 + G_y y$, where $G_y = \partial B_z / \partial y$ denotes the field gradient in the y-direction and B_0, the magnetic field in the z-direction at $y = 0$. To obtain a high spatial resolution (< 10 μm) a very high magnetic field gradient should be applied. However, Maxwell's equations show that when a magnetic field gradient in a certain direction is applied, the magnitude of the field $|\vec{B}|$ in a plane perpendicular to that direction is not constant. At high field gradients the curvature of the surfaces with constant $|\vec{B}|$ becomes comparable to the measured sample
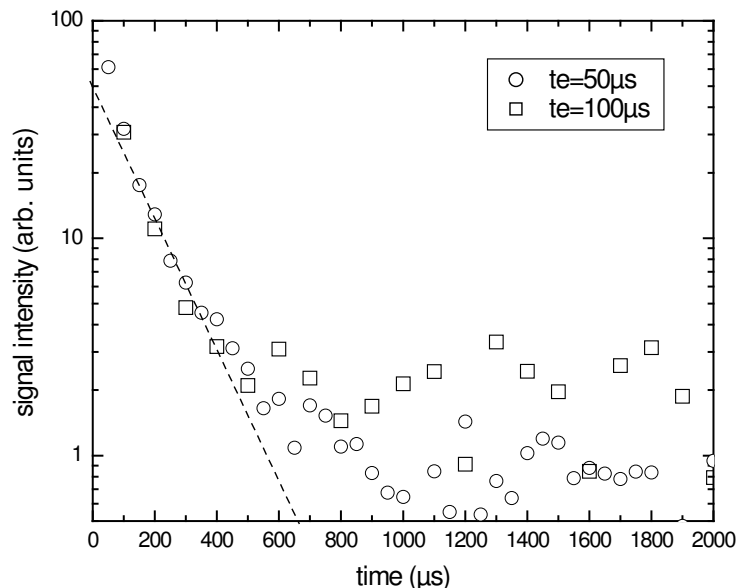
Fig. 7.2: Typical signal decay of a cured alkyd resin, measured using an Ostroff-Waugh sequence. By increasing the inter-echo time from 50 μs to 100 μs the fast signal decay below 100 μs is missed. Also the signal to noise ratio (SNR) decreases, which is a consequence of the increased spatial resolution. The dashed line is a fit to the echo decay observed when using $t_e = 100$ μs as inter-echo time setting.

volume. As a result the resonance frequency varies substantially within a horizontal plane inside the coating, resulting in a decrease of the effective 1D resolution.

To solve this problem, the so called GARField was introduced [27]. In this design a gradient in the magnitude of magnetic field was realized, $G_y^{mag} = d|\vec{B}|/dy$ (see figure 7.1) by creating special-shaped magnetic pole tips. It is then possible to distinguish thin layers within a film, that is oriented perpendicular to the y-direction. The advantage of a setup as shown in figure 7.1 is that a sample can be placed directly on top of a surface coil, which gives a good signal to noise ratio.

In our study we use an NMR setup that contains an electromagnet generating a magnetic field of 1.4 T at the position of the sample. The field gradient is 36.4 ± 0.2 T/m.

7.2.3 Interpreting the NMR signal decay

The NMR pulse sequence used to obtain the hydrogen density profiles and the signal decay is an Ostroff-Waugh (OW) [109] sequence (90°_x-τ-[90°_y-τ-echo-τ]$_n$). The inter-echo time ($t_e = 2\tau$) used in the experiments equals 50 μs, 100 μs, or 200 μs. The theoretical spatial resolution increases when the duration of the signal recording window ($t_{rec} < t_e$) and hence the inter-echo time are increased, according to $\Delta y = 1/\gamma G t_{rec}$. The best achievable spatial resolutions corresponding to the inter-echo time settings given above are 13 μm, 6.6 μm, or 3.3 μm, respectively. The acquisition of each profile took about 10

minutes, using 512 signal averages.

The obtained NMR signals (S) give not only information on the density of the magnetic nuclei (in this case hydrogen nuclei) ρ, but also on the mobility of these nuclei. The network structure determines the mobility of the polymer chains, which is reflected by the transverse relaxation time T_2, describing the decay of the NMR signal. In general this signal decay can be described by

$$S(mt_e) = \sum_i S_i \exp\left(-mt_e/T_2^i\right), \tag{7.1}$$

where t_e denotes the inter-echo time and m the sequence number of the acquired echo, and a sum over all T_2 values is observed. The mobility of the hydrogen nuclei may vary within the coating and therefore different T_2 values can be observed at different positions. The cross-links have a low mobility (short T_2) and the polymer chains between the cross-links have a high mobility (long T_2) [88–90]. Note that with this NMR setup the signal intensity and the signal decay are obtained as a function of depth within the coating.

After curing of the alkyd resin, the mobility of the polymer has decreased significantly because of the cross-linking, which results in a fast signal decay, governed by the interaction between the rigid nuclear dipoles [86]. However, when the signal decay is measured with the OW sequence , at small inter-echo time settings a slightly increased effective T_2 is observed [123]. Therefore, T_2 values can only be compared at fixed inter-echo time settings. In figure 7.2 the signal decay of a completely cured alkyd resin is depicted. The duration of the recording window and, consequently, the inter-echo time should be carefully chosen. When the characteristic T_2 time governing the signal decay is much shorter than the inter-echo time, the resolution is not only determined by the time of the recording window, but also by the T_2-value. In such a case, the duration of the recording window (and hence the inter-echo time t_e) should be decreased, so that more points are measured in a typical decay curve. This makes discrimination of different short relaxation times possible. This is illustrated by the dashed line in figure 7.2, which is a fit for the echo decay observed when using $t_e = 100$ μs as inter-echo time setting. For the setting $t_e = 50$ μs one can see that more relaxation times can be distinguished. Note that the first data point is located significantly above the dashed line. An increase of the duration of the recording window also results in a decrease of the SNR, caused by a decrease of the 1D voxel size. These three effects, the missing of fast relaxation times, the decrease of the SNR, and a shorter effective T_2 at longer inter-echo times, cause that in this film no signal is observed from the cross-linked areas at an inter-echo time $t_e = 200$ μs.

7.2.4 Differential Scanning Calorimeter

Glass transition temperatures of the coatings were determined using a Mettler Toledo Differential Scanning Calorimeter 822^e. The experiments were started at -50 °C and next the sample was heated up to 80 °C, with a ramp speed of 10 °C/min using a 20 μl aluminum crucible. The glass transition temperature was determined from the second run, to eliminate the "memory" (the thermal history of the system) effects seen in the first run [75].
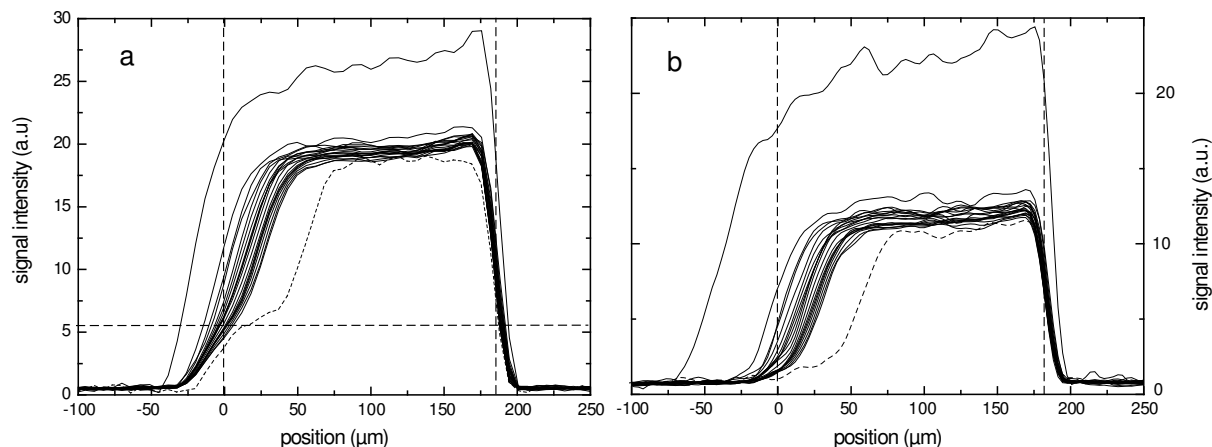
Fig. 7.3: NMR profiles for 0.07% Co metal mass to the mass of the alkyd resin. The profiles were acquired using an inter-echo time setting (a) $t_e = 100$ μs (b) $t_e = 200$ μs. The profiles are given every 9.6 h. The dashed profile is measured after 21 days of curing. The left vertical dashed line indicates the top of the coating after evaporation. The right vertical dashed line indicates the bottom of the coating on top a cover glass. The horizontal dashed line in figure a shows the signal remaining after the complete curing process.

7.3   Results

7.3.1   Curing process

The influence of the catalyst on the curing process was investigated by analyzing the observed changes in the acquired NMR profiles. The profiles obtained from measurements on the water-borne alkyd coating using a 0.07% mass/mass concentration of cobalt catalyst are shown in figure 7.3. NMR measurements were performed with two different inter-echo time settings, $t_e = 100$ μs and $t_e = 200$ μs, shown in figure 7.3a and figure 7.3b, respectively. At the right side of these profiles the cover glass is positioned. The slope of the profiles at the coating/glass interface is limited by the experimental resolution. At the left side the surface of the coating is located, which is in contact with the surrounding air. The profiles are acquired every 10 minutes; only a subset of the profiles is represented in the figure after interpolation over all acquired profiles. First, we observe a drying stage in which water evaporates from the emulsified alkyd. During this stage the height of the profiles decreases and some shrinkage of the film occurs at the left side of the profiles. The first profile plotted in figure 7.3 is measured just after application of the film. After about 5 h of drying, between the first and second profile shown in figure 7.3, a front develops, which moves towards the bottom of the coating. Above this front a glassy skin layer has formed, and underneath this layer uncross-linked resin remains. In figure 7.3a a plateau corresponding to a signal level of about 5 a.u. starts to form, which is the signal that remains after cross-linking has occurred. This is most clearly visible in the profile obtained after 21 days of curing given by the dashed curve. The front becomes
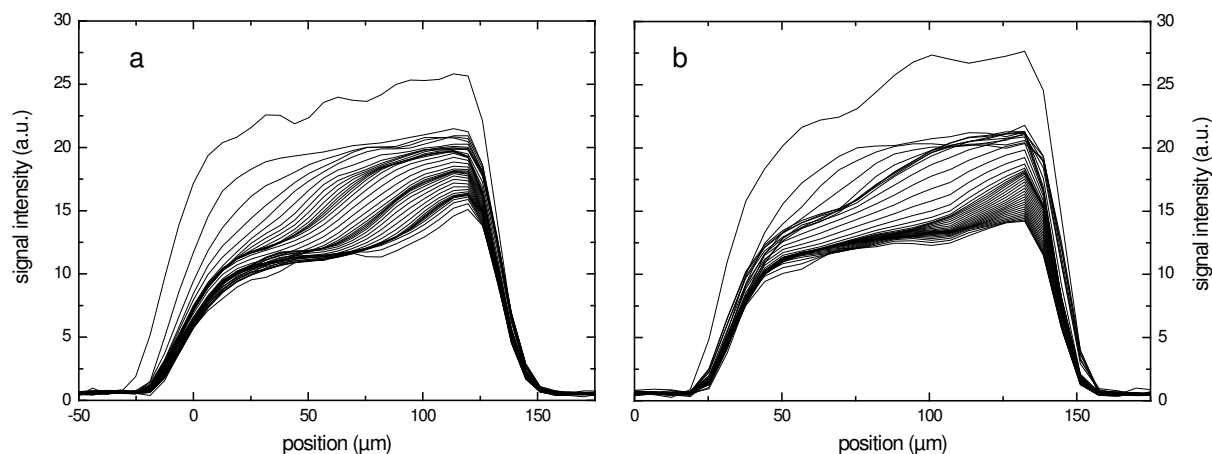
Fig. 7.4: NMR profiles for 0.07% Mn metal mass to the mass of the alkyd resin. (a) Cured with WebMn catalyst, profiles are given every 7.8 h (b) Cured with MnMeTACN catalyst, profiles are given every 3.5 h. The profiles were acquired using an inter-echo time setting $t_e = 100$ μs.

visible because of a decrease of the relaxation time when cross-linking occurs, as was discussed in section 7.2.3. In figure 7.3b, in which the signal is acquired 200 μs after excitation, the signal of the cross-linked part has vanished completely, and the difference between the cross-linked and uncross-linked region is more pronounced. However, since the cross-linked region is no longer visible, the movement of the left edge of the profile could erroneously be interpreted as shrinkage of the film. Therefore, only the profiles acquired with an inter-echo time setting of $t_e = 100$ μs will be shown from now on.

The results of similar measurements on a sample with WebMn and MnMeTACN as a catalyst are plotted figure 7.4a and figure 7.4b, respectively. A curing front is still present in these profiles, but it is not as sharp as is the case for cobalt (figure 7.3). These samples cure more homogeneously, indicating that oxygen penetrates the coating much further than for the cobalt catalyst. The final stage of the curing process, in which no changes are observed anymore, is reached in about one week for the Mn based catalyst, which is much faster than for the Co based catalyst. In case of Co, the observed sharp front takes several months to reach the bottom of the coating. In both figure 7.4a and 7.4b one can clearly see that relative signal decrease during curing is much smaller than for the sample with WebCo as a catalyst. This indicates that the polymers remain more mobile and the network has a lower cross-link density. In the next section we will further discuss the correlation between the curing behavior and the final network structure that is formed.

To check whether the change in behavior for the manganese based catalyst is only a matter of change in reaction rate, the normally used Co based catalyst concentration was diluted by a factor of 100. In figure 7.5 the NMR profiles for this sample are shown. In this case no sharp curing front is present and the results resembles those of the Mn based catalyst. We will further discuss this result in section 7.4.
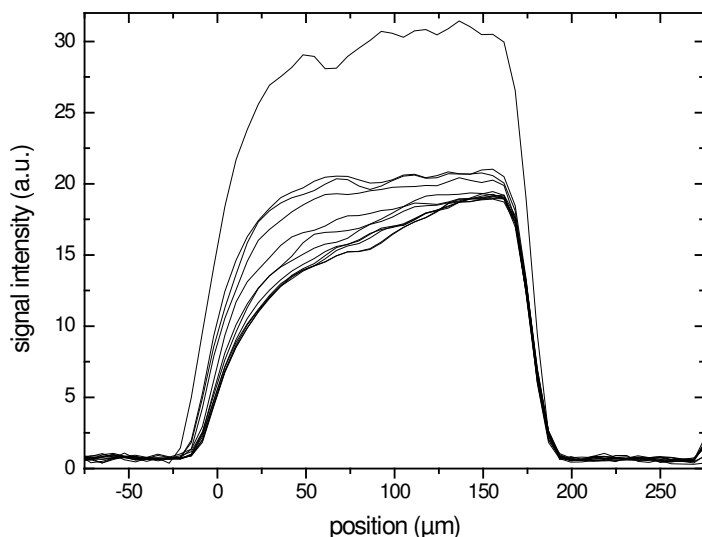
Fig. 7.5: NMR profiles for 0.0007% Co metal mass to the mass of the alkyd resin. The profiles are given at $t = 0, 10.4$ h, and then every 13 h. The profiles were acquired using an inter-echo time setting $t_e = 100$ μs.

7.3.2 Final network structure

Confocal Raman Microscopy can be used to obtain spatially resolved chemical information inside a transparent coating film [23, 24, 26, 41, 117, 124]. The samples measured by NMR were also analyzed using CRM after 6 months of curing to see whether double bonds have remained. This enable us to check whether the cross-link density in the samples with the Mn based catalysts is indeed less dense, as suggested by the NMR measurements. In figure 7.6 the results of these CRM measurements are shown. Because at every position inside the coating the same behavior was observed, only the average is shown. The double bonds (at 1650 cm^{-1}) that are present before curing are clearly visible, but after about 6 months this signal has completely vanished for all types of catalyst. Also T_2 measurements on these samples were performed to measure the mobility. After cross-linking the T_2 values are very short. Therefore, the NMR signal decay was measured using an inter-echo time of 50 μs, at the cost of spatial resolution. Using this setting bi-exponential behavior of the signal decay was observed. Only the longest relaxation time T_2^l contributing to this decay was used in the analysis. Also DSC measurements were performed to obtain the glass-transition temperature (T_g) of these samples. The value of T_g found for the different catalysts, catalyst concentrations, and for the uncross-linked alkyd resin is plotted against T_2^l in figure 7.7. This figure reveals a distinct correlation between T_2^l and T_g. The results also show that if a front is visible during the curing process, a high T_g is observed and T_2^l is short. When no sharp front was visible (all cases except for the normal concentration of cobalt catalyst) T_g was significantly lower and T_2^l longer.

We conclude that even though CRM shows complete curing, NMR and DSC still show differences in the final network structure as a result of changes in catalyst or catalyst
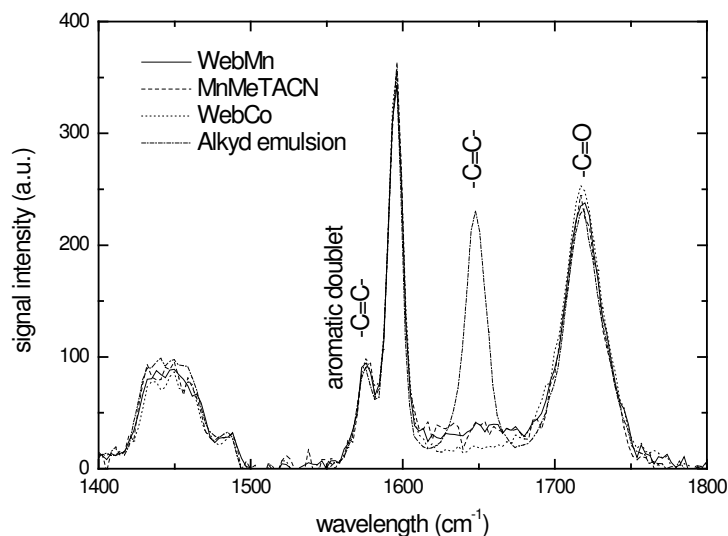
Fig. 7.6: Results obtained using Confocal Raman Microscopy for the three catalyst used. No double bonds remain after complete curing of the coating after 6 months.

concentration, which indicates that changes have occurred during the curing of the alkyd resin.

7.4 Model

To explain the observed characteristics in more detail we need to obtain information on the reaction rate and the diffusion of oxygen for the different catalysts. To achieve this, the evolution of the NMR profiles of curing alkyd resins was described by a reaction-diffusion model and by the change of the signal decay caused by the cross-linking.

Since the results have shown that for the manganese catalyst no longer a sharp front exists, as reported in chapter 5 and chapter 6, those models no longer hold. Equation 5.4 is a special case of the reaction-diffusion equations presented in this section. Additionally, the diffusion of reactive species reported in chapter 6 is neglected in the model presented here, because this behavior was only observed in solvent-borne alkyd coatings.

In the first subsection the reaction-diffusion equations are discussed, and in the next subsection the NMR profiles are explained in more detail, using a model describing the change of the signal decay as a function of the degree of cross-linking. In the third subsection the predictions from the reaction-diffusion model are compared with the NMR results.

7.4.1 Reaction-diffusion equations

The reaction of oxygen with fatty acid side chains of the alkyd resin causes a decrease of the concentration of double bonds ρ_d [mol/m^3] and the formation of cross-links. The
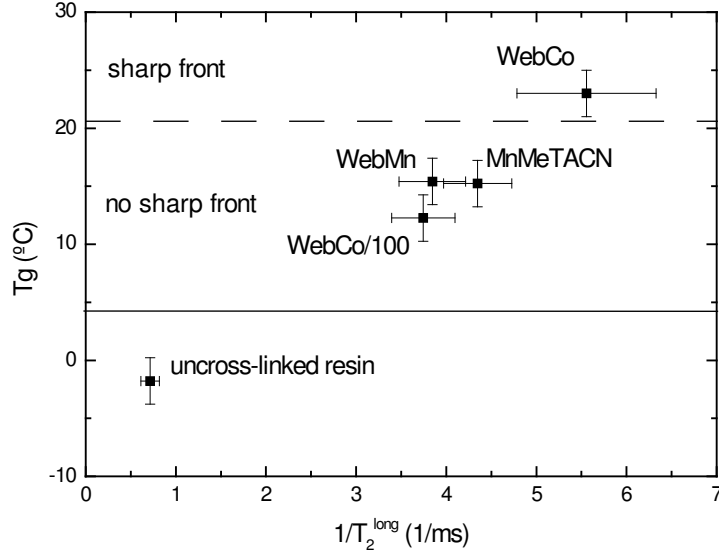
Fig. 7.7: Relation between T_2 measured with NMR and T_g measured with a DSC.

oxygen diffusivity D [m^2/s] generally depends on the mobility of the polymers. The oxygen density ρ_o [mol/m^3] inside the coating is determined by oxygen diffusion as well as the reaction of oxygen with the double bonds and can be described by

$$\frac{\partial \rho_d}{\partial t} = -k\rho_o\rho_d, \tag{7.2}$$

$$\frac{\partial \rho_o}{\partial t} = \frac{\partial}{\partial x}\left(D(\rho_d)\frac{\partial \rho_o}{\partial x}\right) - nk\rho_o\rho_d, \tag{7.3}$$

in which k [m^3/mol s] denotes the reaction rate of the oxygen with the double bonds, and n [mol/mol] denotes the amount of oxygen reacting per double bond. We will assume $D(\rho_d) = D$ in all numerical calculations. The boundary conditions are specified as follows

$$\rho_o(0,t) = \rho_o^i, \tag{7.4}$$

$$\frac{\partial \rho_o}{\partial x}(L,0) = 0, \tag{7.5}$$

$$\rho_o(x,0) = 0, \tag{7.6}$$

$$\rho_d(x,0) = \rho_d^i, \tag{7.7}$$

where L is the coating thickness and denotes the position of the microscope glass. At $x = L$ the the oxygen flux is zero, whereas at the surface the oxygen density is equal the solubility density. The oxygen density within the film is taken equal to zero at the start of the curing process. The initial values are given in table 7.1.

7.4.2   NMR profiles

The measured NMR signal decay of the alkyd coatings is governed by multiple relaxation times (see equation 7.1 and section 7.2.3) when the resin is not cross-linked. If an inter-

ρ_d^i [mol/m^3]	ρ_o^i [mol/m^3]	n [mol/mol]	S_s [a.u.]	T_2^s [μs]	S_l [a.u.]	T_2^l [μs]
2000	3	1.0	37	50	17	1000

Table 7.1: Fixed initial values used in the numerical simulations. The values of S_i and T_2^i are chosen to correspond with the experimental values obtained from the NMR data.

Catalyst	D [m^2/s]	k [m^3/mol s]	L [μm]	figure
WebCo	10^{-12}	1×10^{-4}	200	7.8
WebCo/100	4×10^{-12}	1×10^{-6}	200	7.9
WebMn	8×10^{-12}	5×10^{-6}	150	7.10
MnMeTACN	2×10^{-11}	5×10^{-6}	125	7.11

Table 7.2: Values for the diffusion constant, reaction constant, and layer thickness used in the different simulations. The figures displaying the simulated results are also indicated.

echo time $t_e = 100$ μs is used, two relaxation times are observed before cross-linking. After cross-linking only one relaxation time can be observed, see also [121]. Therefore, the signal decay can be described by

$$S(mt_e) = S_s(t) \exp\left(-mt_e/T_2^s\right) + S_l(t) \exp\left(-mt_e/T_2^l\right), \qquad (7.8)$$

where $S(mt_e)$ is the NMR signal during the NMR experiment and m the sequence number of the echo. Note that mt_e is of the order of ms, whereas the time t corresponds to the time scale of the curing process, which is of the order of hours or days. S_s is the intensity of the signal corresponding to the short relaxation time T_2^s and S_l the intensity of the signal corresponding to the long relaxation time T_2^l. In all numerical simulations average values for T_2^l and T_2^s were taken, although, for the manganese based catalyst slightly higher values of T_2^s were observed.

We assume that when the cross-linking occurs the mobile chains become immobile, so the contribution of S_l to the observed NMR signal will be incorporated in S_s. This signal change is assumed to be proportional to the amount of double bonds present. This implies that when no double bonds are present any more only one relaxation time is observed, which agrees with the results of our NMR measurements.

Additionally, the simulated profiles are convoluted with the observed experimental resolution of about 10 μm to enable a more direct comparison between simulations and measurements.

7.4.3 Results

Combining the reaction diffusion equation and the equations relating the NMR signal profiles to the cross-linking process, numerical simulations can be performed. We have performed calculations on four different systems that represent the ones presented in section 7.3.1. For these four coatings the fixed parameters have to be specified. We need the amount of double bonds ρ_d, oxygen concentration ρ_o, amount of oxygen per

double bond n, diffusion constant D, and reaction constant k. The values of S_s, S_l, T_2^s, and T_2^l were determined from the NMR data. Table 7.1 shows the initial values that are taken constant in all numerical simulations. The only parameters that are varied are the diffusion and reaction constant. The alkyd used has an oil length of 40%, which corresponds to 400 kg/m^3. Taking a molar mass of about 300 g/mol for the fatty acid chain gives 1200 mol/m^3 of oil chains. Since each oil chain contains on average two double bonds ρ_d is set at 2×10^3 mol/m^3. From oxygen uptake measurements of ethyllinoleate, a model system, it is known that n, the amount of oxygen molecules per double bond, is about 0.75 in case of a manganese based catalyst and about 1.1 in case of a cobalt based catalyst [72, 122], so n will be taken equal to 1. The oxygen solubility in oil is estimated as 3 mol/m^3 [40, 41, 125].

For the four different coating systems simulations were performed, at time intervals similar to the measured profiles. Note that the evaporation stage is not included in the simulations. The thickness of the coating in the simulation was set to the thickness measured using the NMR setup. For the different catalysts the values for the diffusion and reaction constant used in the simulations are given in table 7.2. They were chosen such that a good match between the simulations and the observed profiles was obtained. Although these values should only be considered as crude estimates, due to the inaccuracy in the initial values given in table 7.1, they can be used to explain the observed tendencies of the curing behavior. The results for the film containing WebCo as a catalyst are plotted in figure 7.8. The simulated results clearly show the cross-linking front moving to the right that is present in the experimental data. Clearly, oxygen diffusion is the limiting step, see also the high reaction constant and low diffusion constant in table 7.2. Since in the cross-linked region the T_2 is very short, the actual experimental resolution is lower than that was used in the simulations. This explains why, in contrast to the simulations, the plateau observed in the measurements after 21 days of curing is not horizontal. For the diluted WebCo (Fig. 7.9) the reaction constant in the simulation was decreased by a factor of 100, equal to the dilution of the catalyst, which implicitly assumes that the reaction constant is proportional to the catalyst concentration. An increase of the diffusion constant was needed to obtain a behavior matching the results of the NMR measurements, which is reasonable if the coating is less densely cross-linked. For the WebMn and MnMeTACN catalysts the reaction constant was kept constant at 5×10^{-6} m^3/mol s, whereas the diffusion constant was varied to obtain a good match with the experimental data, see figure 7.10 and figure 7.11. The diffusion constant ranges between 10^{-11} and 10^{-12} m^2/s, which is within the range of values reported in the literature [126, 127]. The reaction constants correspond fairly well to representative reaction constants given in the literature [22].

If we compare the simulations of the NMR profiles with the NMR measurements for the manganese based catalysts, we observe that the signal intensity that remains in the NMR measurements in the cross-linked region is larger than the signal intensity in the simulations. This is caused by the fact that the value of T_2^s in these systems is somewhat larger than the average value used or the simulations. The CRM measurements have indicated that all double bonds have reacted, but the results from the NMR T_2 and the T_g measurements plotted in figure 7.7 indicate a higher polymer mobility. The final network structure seems to be less dense than for the WebCo catalyst, which explains

Fig. 7.8: Time and position dependence of the NMR hydrogen signal for the WebCo catalyst a) experimental data b) results obtained from a reaction-diffusion-relaxation NMR model. $D = 10^{-12}$ m^2/s, $k = 1 \times 10^{-4}$ m^3/mol s, $L = 200$ μm. In the the left graph the dotted profile after 21 days of curing is plotted to make the formation of the plateau more clearly visible.

the higher diffusion coefficient needed as input for the simulation of the NMR profiles. A possible explanation of this change in network structure may be a change of reaction routes of the oxidation mechanism of unsaturated fatty acids, but this is beyond the scope of this paper.

For the coating with the WebCo catalyst, shown in figure 7.8, the reaction constant is the highest and the diffusion constant used in the simulation is the lowest. The high reaction rate is the basis for the formation of a glassy skin. In this glassy skin the polymer mobility is very low, because it is fully cross-linked, making diffusion of oxygen difficult. In this particular case the diffusion of oxygen is the limiting factor. If one would plot the front position as a function of $\sqrt{t}$ a linear relation would be found, as described by equation 5.4. The width of the front does not affect this behavior as long as the front does not reach the bottom of the coating.

For the other simulations the reaction constant is much lower, and a sharp front is no longer observed, as a result diffusion takes place through a partly cross-linked region. Since the diffusion constant is expected to decrease during curing, the diffusion varies as function of position inside the coating in these simulations. Based on the diffusion constants given in table 7.2, we estimate that the diffusion varies at most within one order of magnitude. Because in the simulations the diffusion is assumed to be constant, the results at long simulations times may differ from the experimental data.

7.5 Conclusions

Using NMR depth profiling we observed distinct changes in curing behavior for different catalysts. For a cobalt based catalyst a sharp drying front was observed, whereas for the

Fig. 7.9: Time and position dependence of the NMR hydrogen signal for the 100 times diluted WebCo catalyst a) experimental data b) results obtained from a reaction-diffusion-relaxation NMR model. $D = 4 \times 10^{-12}$ m^2/s, $k = 1 \times 10^{-6}$ m^3/mol s, $L = 200$ μm.
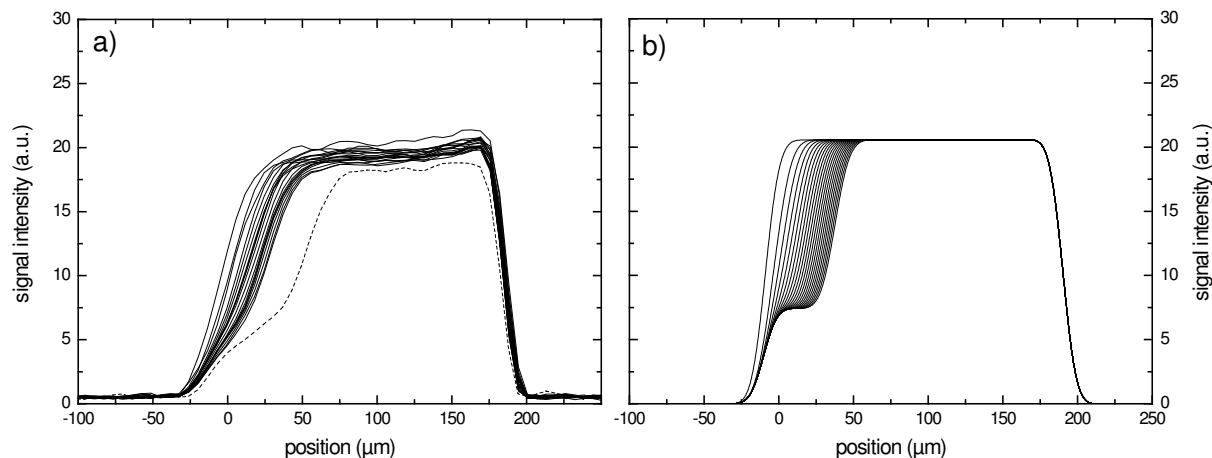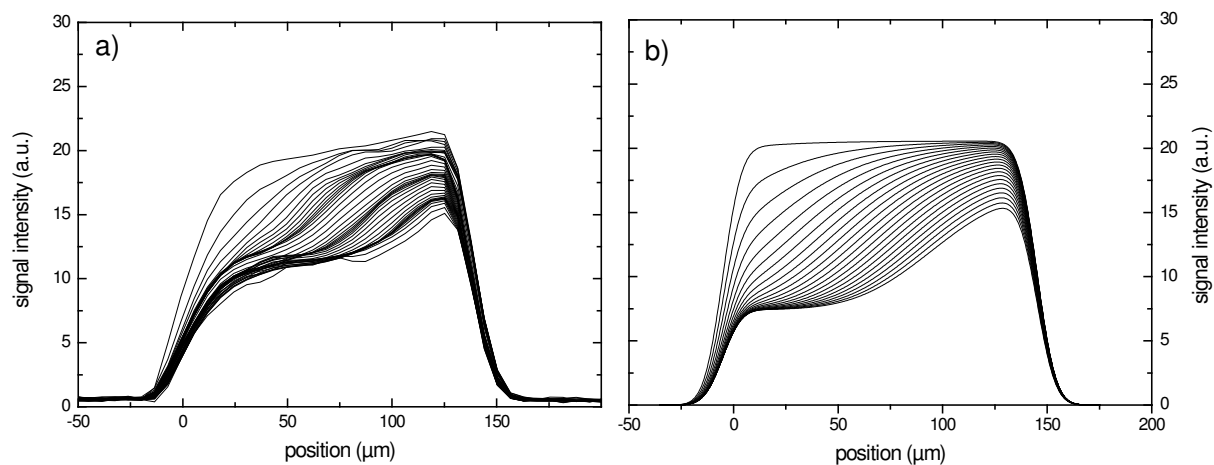

Fig. 7.10: Time and position dependence of the NMR hydrogen signal for the WebMn catalyst a) experimental data b) results obtained from a reaction-diffusion-relaxation NMR model. $D = 8 \times 10^{-12}$ m^2/s, $k = 5 \times 10^{-6}$ m^3/mol s, $L = 125$ μm.
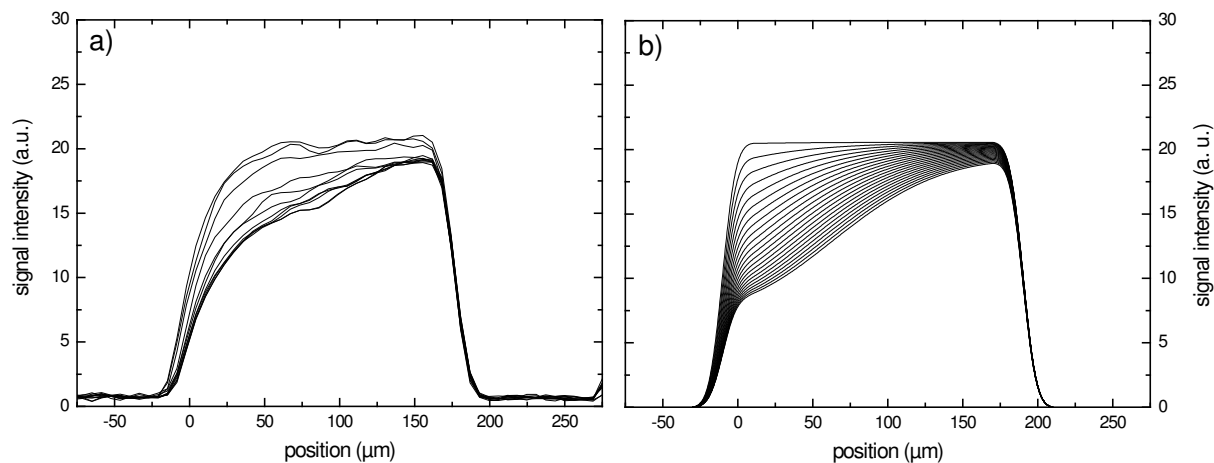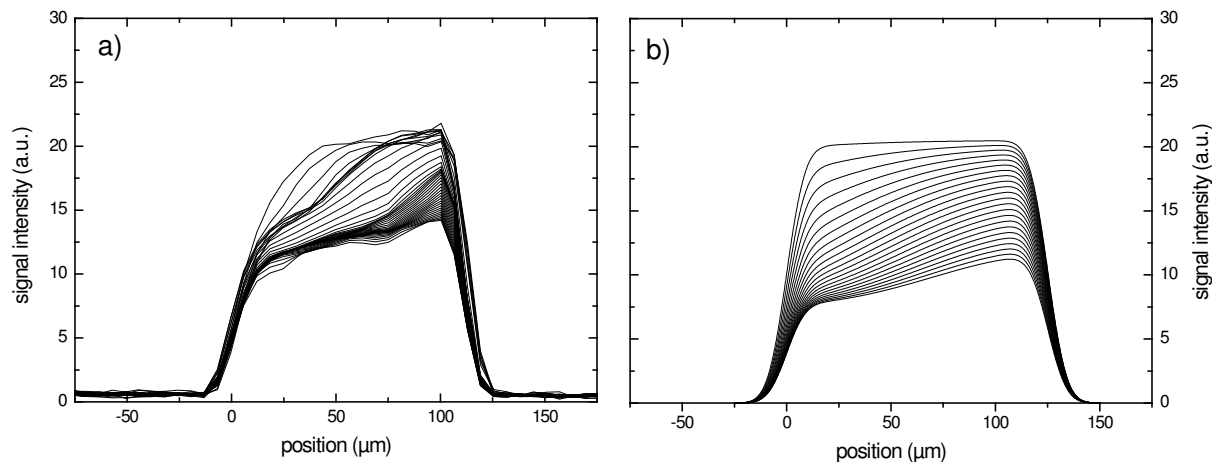
Fig. 7.11: Time and position dependence of the NMR hydrogen signal for the MnMeTACN catalyst a) experimental data b) results obtained from a reaction-diffusion-relaxation NMR model. $D = 2 \times 10^{-11}$ m^2/s, $k = 5 \times 10^{-6}$ m^3/mol s, $L = 150$ μm.

manganese based catalysts no sharp front was observed. Additionally, the final network structure after complete curing was analyzed by DSC and NMR. A decrease in glass transition temperature T_g for the manganese catalysts compared to the cobalt catalyst was found. Also a clear correlation between T_g and the NMR relaxation time T_2 was found; with increasing T_g the value of T_2 decreases. When a sharp cross-linking front was present in the NMR data, the final cross-link density was found to be higher, indicated by both the T_2 and T_g values. This behavior might be explained by changes in the complex autoxidation mechanisms involved in the cross-linking of alkyd resins [43, 44, 48, 51], which is beyond the scope of this paper.

The differences in curing speed observed for the WebCo, WebMn, and MnMeTACN catalyst can be explained by changes in reaction rate and oxygen diffusion constant only. A change of the diffusion constant seems to be necessary to obtain a good match between the simulations and the experimental NMR profiles. An increase of the diffusion coefficient indicates that the network structure is less rigid, which is corroborated by the lower cross-link density found for the low concentration of WebCo and for the manganese based catalysts.

Replacing the cobalt based catalyst in coatings obviously results in completely different curing behavior, whereas also the final hardness seems to change. Our study unambiguously demonstrates that the consequences of replacement of the catalyst cannot solely be assessed from measurements on model systems, but also knowledge on the curing behavior inside a coating is required. High resolution nuclear magnetic resonance has proven to be an excellent tool to achieve a more in-depth knowledge of the curing behavior and degree of cross-linking in coatings.

8. Drying of alkyd coatings on porous substrates

Coatings are often applied on porous substrates, e.g., wood, stone, or gypsum layers. The type and porosity of the substrate influences the coating performance. One example is the adhesion, which generally increases when the depth of penetration of the coating into the substrate is higher. Until recently, no techniques were available to monitor the drying process in-depth as a function of time with a high spatial resolution (about 5 μm) in non-transparent coating systems. In the study presented in this chapter, we show that with high resolution NMR imaging the drying process, consisting of penetration and evaporation of solvent and subsequent curing (chemical cross-linking) on and inside the substrate (wood and gypsum) can be monitored. The drying of a water-borne alkyd emulsion on a gypsum substrate was investigated. The curing of the emulsion was studied for both glass and gypsum substrates as a function of catalyst concentration, in this case cobalt based. Curing was not only observed at the coating surface, but in case of gypsum also at the coating/substrate interface. On both substrates a concentration dependence of the catalyst concentration was observed. On the gypsum substrate the speed of the observed curing front was always higher than on glass. This indicates that part of the Ca^{2+} ions originating from the gypsum might act as a secondary drier after migration to the coating. The drying of a commercially available solvent-borne alkyd coating was monitored on gypsum and pine wood. The measurements showed that the coating completely penetrates the substrate and starts to cure inside. From the results it can be concluded that for optimization of the coating performance one should explicitly take the substrate into account.

8.1 Introduction

Coatings provide many substrates with protection against environmental attacks like moisture, biological processes (e.g. growth of fungi), radiation, heat, and chemical stresses. In many cases the coatings are applied on porous substrates, e.g., wood, stone, or gypsum layers. In recent years the paint market has changed considerably, partly due to the legislation on the emission of volatile organic components (VOC). As a result more eco-friendlier alternatives, such as waterborne products have been developed. The performance of these and/or new products on porous substrates should be competitive with the traditional systems. To further improve and reduce development times and costs of products, knowledge about the interaction between the coating and the underlying substrate is required, because the substrate can in many ways affect the performance of the

coating.

One example of a type of paint, which is often applied on porous substrates, is alkyd paint. When an alkyd paint is applied onto a porous substrate three drying stages can be distinguished. First, the solvent and/or the resin penetrates the substrate. During the second stage, the solvent evaporates from the coating and the underlying substrate. During the third stage, the coating starts to solidify by the formation of chemical cross-links (curing). Immediately after application the coating penetrates the substrate. When the penetration into the substrate is higher, the adhesion of the coating onto the substrate is likely to increase [128, 129]. The depth of penetration depends on the paint properties such as the viscosity and the surface tension, and substrate properties like permeability and characteristic pore sizes. Note that the conductance of flow in porous media is determined by the ratio between the permeability and viscosity. The driving force is the capillary force, which is proportional to the ratio between the surface tension and the pore size. The flow properties of the three different types of alkyd paint (solvent-borne, high-solid, water-borne) differ, because of differences in viscosity [130, 131].

Many water-borne coatings consist of emulsified resin droplets in water. When these emulsions are applied on a porous substrate the penetration of the different phases in a porous substrate can differ [69]. The size and visco-elastic deformation of the emulsion droplets together with the pore size of the substrate determines whether or not the resin will enter the substrate. It was suggested by Ostberg et al. [69] that the water phase penetrates deeper into wood than the alkyd resin, because of the high molecular weight of the resin. The difference in penetration behavior of the water and resin phase will have consequences for the additives present inside the coating, such as driers, anti-fungal agents, and pigments. Additives that are partly present in the water phase might end up inside the substrate instead of in the coating, which can have a negative influence on the drying process and many other properties. An important class of additives are the driers. Driers enhance the drying process of alkyd coatings, their main purpose is to catalyze the oxidative curing process. The most commonly used catalysts for the curing of alkyd resins are cobalt based. During the penetration of the coating into the substrate also part of the catalyst might be transported into the substrate. As a result the concentration in the coating drops, thereby affecting the curing of the coating, which might affect other properties, such as the resistivity against moisture [132–134].

To study the effects of the substrate on the drying behavior, information on the dynamics of the drying process of the alkyd coating on a porous substrate as a function of depth is required. Except for NMR there are no techniques to follow the drying process as a function of depth in non-transparent coating systems. In this study we use our recently developed NMR setup, see chapter 3, to investigate the curing process of alkyd coatings on porous substrates as a function of depth and time. Two types of alkyds are investigated, a solvent-borne and a water-borne. The water-borne alkyd coating is applied on non-porous glass, as a reference, and on porous gypsum. The solvent-borne alkyd coating is applied on gypsum and wood. The depth of penetration, the curing, and the effect of the substrate on the speed of the curing will be investigated. In section 8.2, we briefly discuss the materials used. In section 8.3 the results of the NMR measurements are presented. This section is subdivided in three parts. First NMR measurements of the water-borne

alkyd coating on glass are presented. The catalyst concentration to cure the coatings is varied and the speed of curing is analyzed. The curing of alkyd on the gypsum substrate is presented in the second part. In the third part, the drying of a solvent-borne alkyd on gypsum and pine wood is studied. Finally, the conclusions are presented in section 8.4.

8.2 Experimental details

8.2.1 Materials

A water-borne alkyd emulsion, containing approximately 50% water and 50% resin was used. Nuodex WebCo 8% catalyst was added in different concentrations to catalyze the curing process. The emulsion has an average droplet size of 0.3 μm [40, 131]. The glass transition temperature of the uncross-linked alkyd resin is 2 ± 2 °C. Except for the catalyst no other additives or pigments were added to the emulsion. After the addition of the cobalt catalyst to the emulsion and subsequent mixing, the emulsion was applied on the substrate (non-porous glass or gypsum) using a spiral application rod. The glass substrate used was a 100 μm thick microscope cover glass. The gypsum layer (CaSO$_4$·2H$_2$O) had a thickness of approximately 400 μm and a porosity of about 45%. The layer was made from pure hemihydrate (CaSO$_4 \cdot \frac{1}{2}$H$_2$O) using a water to binder mass ratio of 0.66 [135]. The average pore diameter of the gypsum was found to be in the order of 1 μm by [135], and was calculated from mercury intrusion porosimetry data assuming cylindrical pores. The peak to peak surface roughness was reported to be approximately 5 μm.

Besides the water-borne formulation, a commercially available solvent-borne alkyd was used. This coating was applied on a gypsum substrate approximately 0.3 mm thick and a thin layer of pine wood approximately 0.5 mm thick. For more details on the microscopic structure of pine wood and a microscopic investigation of paint penetrating pine wood see [136].

8.2.2 Pulse sequence

After application of the coating on the substrate, it was immediately placed in the NMR setup. The NMR pulse sequence used to obtain the hydrogen density profiles and the signal decay was an Ostroff-Waugh [109] sequence (90°_x-τ-[90°_y-τ-echo-τ]$_n$). The inter-echo time (2τ) used in the experiments equals 100 μs. The theoretical spatial resolution corresponding to this inter-echo time setting is 6.6 μm, see chapter 3. The acquisition of each profile took about 10 minutes, using 512 signal averages.

8.3 Results

8.3.1 Water-borne alkyd applied on glass

First the drying behavior of the water-borne alkyd emulsion on a glass substrate was investigated. In figure 8.1 the NMR profiles are shown for a coating with a cobalt concentration of 0.007% mass/mass. At the left side of the profiles the surface of the coating is
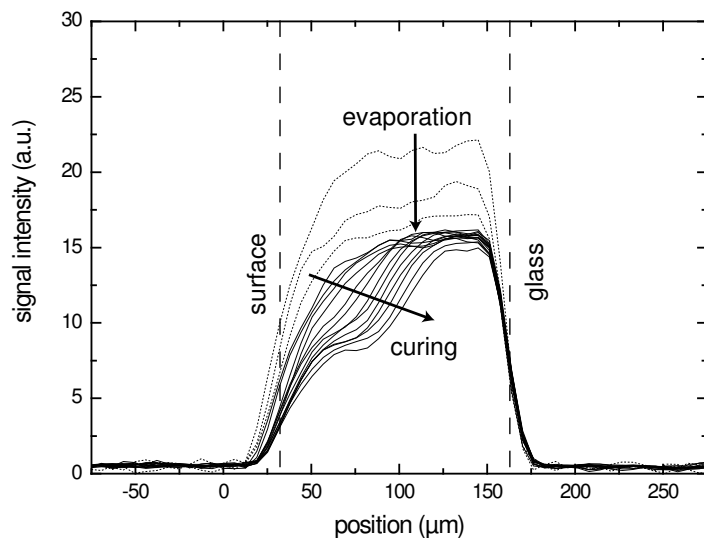
Fig. 8.1: NMR profiles of a coating with 0.007% cobalt mass to the mass of the alkyd resin applied on a glass substrate. The profiles are given at $t = 0, 1.3, 2.6, 5.2, 7.8, 10.4$ h and then every 13 h. The dotted profiles indicate the evaporation stage, and the solid profiles the curing stage.

located, and at the right side the glass substrate is located. Directly after application the evaporation stage sets in, represented by the dotted curves. One can see the formation of a cross-linking front: When polymers cross-link and form a network, the mobility of the hydrogen nuclei decreases. As a consequence, the decay rate of the NMR signal increases and part of the signal is lost, which allows the curing to be visualized [117]. The drying behavior was studied for different cobalt catalyst concentrations, ranging from 0.7% mass/mass to the alkyd resin to 0.007% mass/mass.

In order to characterize the dynamics of the cross-linking front in more detail, we have determined the front positions f from the intersections of the fronts with a line positioned halfway the height of the front. We will refer to the moment that a front appears and starts to move into the coating as $t = t_0$, which is roughly 2 h after application. The position of the front at $t = t_0$ is denoted by f_0. The front positions f for three typical concentrations (0.7%, 0.07%, and 0.007%) are plotted in figure 8.2 as $(f - f_0)^2$ against $t - t_0$. This figure reveals that within experimental inaccuracy the squared front position varies linearly with time. In chapter 5 it has been shown that oxygen diffusion limits the speed of the cross-linking front, and can be described with the following equation [121]:

$$f(t) = f_0 + \sqrt{2\nu D \rho_0 (t - t_0)}. \tag{8.1}$$

In this equation f_0 [m] is the front position at the moment t_0 [s] at which the front forms and starts to move into the coating, D [m^2/s] the diffusion constant of oxygen in the coating, ρ_0 [mol/m^3] the oxygen density in the surface layer of the coating film, and ν [m^3/mol] the cross-linked volume per mole of oxygen.

In figure 8.3 the front speed ($2\nu D \rho_0$) is plotted as a function of the catalyst concen-
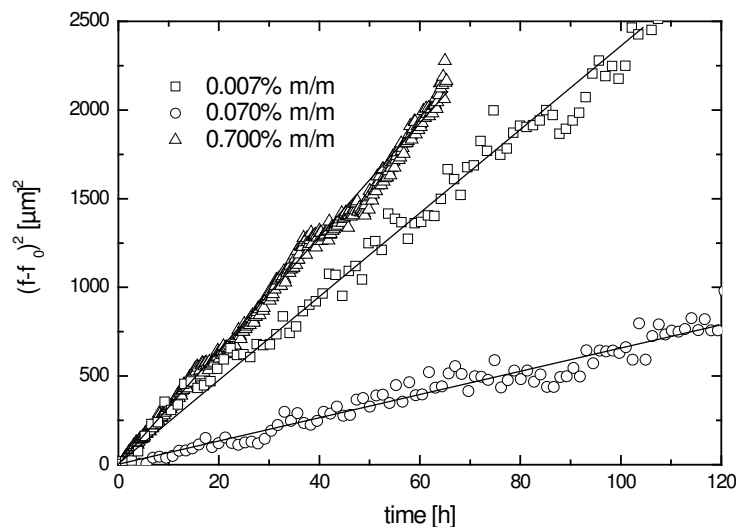
Fig. 8.2: Squared curing front positions of alkyd resins plotted against time for three cobalt catalyst concentrations. The coatings were all applied on a glass substrate. Both the high and low catalyst concentration leads to faster curing of the sample.

tration (open squares). The curve through the points is drawn as a guide to the eye. At the lowest and highest concentration the fastest front speeds are observed. The slowest curing occurs at the cobalt concentration of 0.07% mass/mass, which is common concentration used in commercial products. According to equation 8.1, changes in front speed can be attributed to three variables: ν, D, and ρ_0. It seems that the catalyst concentration influences the final network structure. If the network structure would becomes less dense (higher ν), the diffusion of oxygen increases (higher D), resulting in an increase of the front speed by both variables. This would mean that the highest network density is formed exactly at the Co catalyst concentration of 0.07% mass/mass.

8.3.2   Water-borne alkyd applied on gypsum

The water-borne alkyd emulsion was also investigated on the gypsum substrate. The profiles of the NMR measurements are plotted in figure 8.4. At the left side the coating is located and at the right side the gypsum is located. The surface of the coating and the coating/substrate interface are denoted by the two vertical lines. The measurements show that the penetration of the water phase into the gypsum layer is almost instantaneous, and wets the gypsum layer. In practical applications the gypsum substrate is thicker, and as a result the water uptake would be even higher. Directly after this water uptake, the water present in the coating and substrate starts to evaporate. This process is indicated by the dashed profiles in figure 8.4. The signal intensities from the gypsum layer before application of the paint and after the evaporation stage are the same. Therefore, it can be concluded that the resin has not penetrated the substrate, except possibly at the interface with a penetration depth smaller than the experimental resolution.
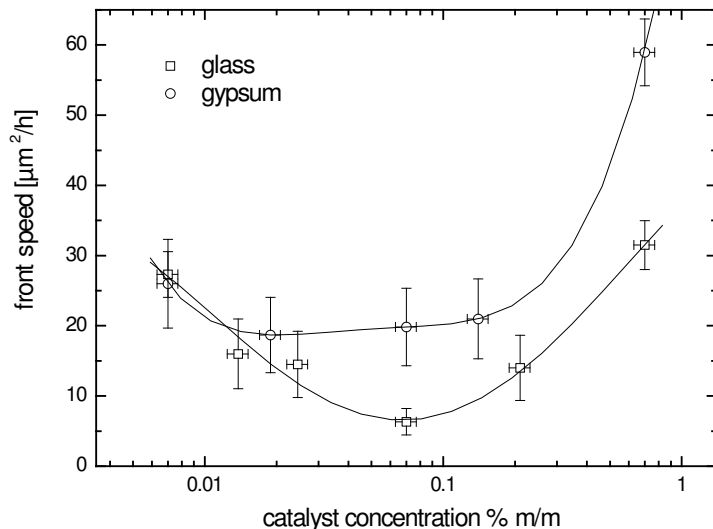
Fig. 8.3: Front speeds of alkyd resins plotted against the catalyst concentration for both the glass and gypsum substrates.

size	hard droplets	deformable droplets
droplet > pore	impossible	possible
droplet < pore	possible	possible

Table 8.1: Possibility of penetration of waterborne alkyd emulsion droplets in a porous substrate based on droplets size and deformability of the alkyd droplets, assuming that the driving capillary forces are high enough.

In general, the penetration depth of the resin droplets in the substrate is determined by the deformability of the resin droplets and the size of the alkyd droplets compared to the characteristic pore sizes of the substrate, as was discussed in section 8.1. Table 8.1 indicates whether penetration can be expected for a water-borne alkyd emulsion, based on the size of the droplets and the deformability of the droplets, assuming that the driving capillary forces are high enough. If the droplets are difficult to deform but their size is small compared to the pore size, penetration is possible. However, if the droplets are difficult to deform but larger than the pore size the coating is not expected to penetrate the substrate. In our case the emulsion droplet size ($0.3 \ \mu$m) is comparable to the pore size of the gypsum (approximately 1 μm) and the droplets are difficult to deform (their shape is still visible with AFM after drying). Since the internal structure of gypsum is irregular and the pores are not cylindrical, as was assumed in the calculation of the porosity of gypsum from mercury intrusion porosimetry [135], it is likely that the emulsion droplets are still too large to penetrate the substrate. In addition, due to the fast absorbtion of the water phase the resin droplets might already start coalescing before penetrating the substrate.

After the evaporation stage, curing sets in, which is denoted by the two bold arrows in
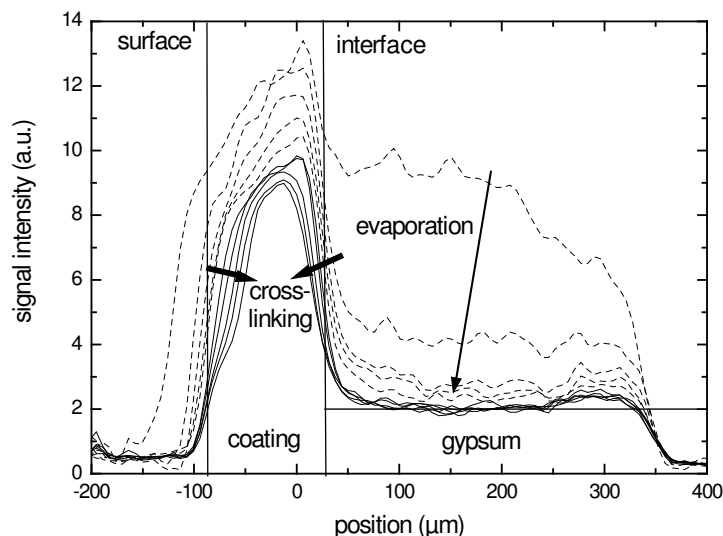
Fig. 8.4: Water-borne alkyd emulsion with 0.07% Co mass/mass as a catalyst. The dashed profiles show the penetration and evaporation of the solvent. These profiles are given at $t = 0, 0.3, 0.6, 1.0, 1.3$ h. The solid profiles show the curing of the coating. These profiles are given at $t = 8, 16, 49, 65$ h after application. The horizontal line shows the signal from the hydrated gypsum layer, both before and after paint application.

figure 8.4. Not only a curing front is visible at the surface of the coating, but also at the coating/gypsum interface. One can clearly see that at the surface of the coating, the front moves towards the bottom of the coating, whereas at the substrate side the front moves towards the top of the coating. Obviously, oxygen transport is taking place through the gypsum layer, which is possible because it is a porous layer in contact with air.

We have plotted the square of the position of the curing front (at the surface) against time in figure 8.5 for three typical catalyst concentrations. Again this figure reveals that within experimental inaccuracy the squared front position varies linearly with time. In figure 8.3, the front speeds found for the gypsum substrate are plotted as a function of the Co concentration. In general the trend is comparable to that observed for the glass substrate. However, the front speeds observed for the coating on the gypsum layer are always higher than for the same coating applied on glass. Besides this effect, we observe that at higher Co concentrations the front speed for the coating on the gypsum layer increases much faster than in case of the glass substrate.

The observation that the overall front speed is faster on a gypsum substrate cannot be explained by transport of cobalt to the substrate. For cobalt concentrations above 0.07% on glass figure 8.3 shows that the front speed increases with cobalt concentration. If part of the catalyst would be transported to the substrate the concentration and consequently the front speed in the coating would decrease. This is not in agreement with the data shown in figure 8.3, which clearly indicates a higher front speed when the coating is applied on gypsum instead of glass. However, that part of the cobalt catalyst has been transported out of the coating into the gypsum substrate was confirmed by Inductively
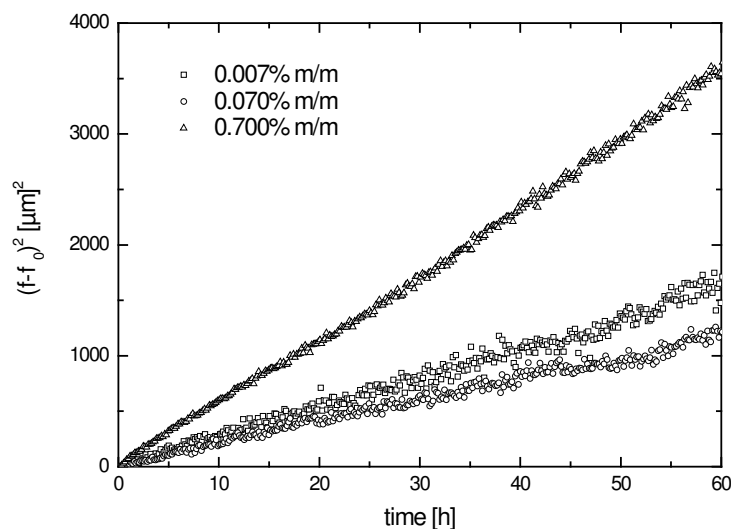
Fig. 8.5: Squared curing front positions observed at the surface of the alkyd coatings applied on a gypsum layer plotted against time for three cobalt catalyst concentrations. Only a high catalyst concentration leads to faster curing of the sample.

Coupled Plasma (ICP) spectrometry. So the overall increase of front speed needs to be explained by another effect. We attribute the increase to the presence of Ca^{2+}. Directly after application the water penetrates the substrate, and via the water Ca^{2+} ions from the $CaSO_4$ might migrate from the substrate into the coating. In a recent study [137], we have found that addition of Ca/Zr as secondary driers results in an increased front speed, which might indeed explain the observed increased front speed on gypsum substrates.

8.3.3 *Solvent-borne alkyd applied on gypsum and wood*

In this section it will be shown that curing can be investigated even inside the porous substrate. We have studied a solvent-borne alkyd coating on two porous substrates: gypsum and wood. The NMR profiles for the gypsum substrate are plotted in figure 8.6. The alkyd completely penetrates the gypsum layer, because its it is molecular dispersed in the solvent and the overall liquid has a low viscosity. In this particular case it is difficult to distinguish the evaporation of the solvent and the curing process. A small curing front is visible and is indicated in figure 8.6 by the arrow at the left. The solvent-borne alkyd was also applied on a thin layer pine wood with a thickness of approximately 0.5 mm. The results of the measurements are given in figure 8.7. The surface of the coating is located at the left side of the profile and the vertical line shows the surface of the wood. The solvent and resin both penetrate the wood almost instantaneously after application; after the first profile no changes are observed in the deeper region of the wood. In this case the depth of penetration into the wood is approximately equal to the thickness of the pine wood. After the penetration of the substrate the solvent starts to evaporate. This stage is indicated by the dashed profiles in figure 8.7. Again a curing front develops,
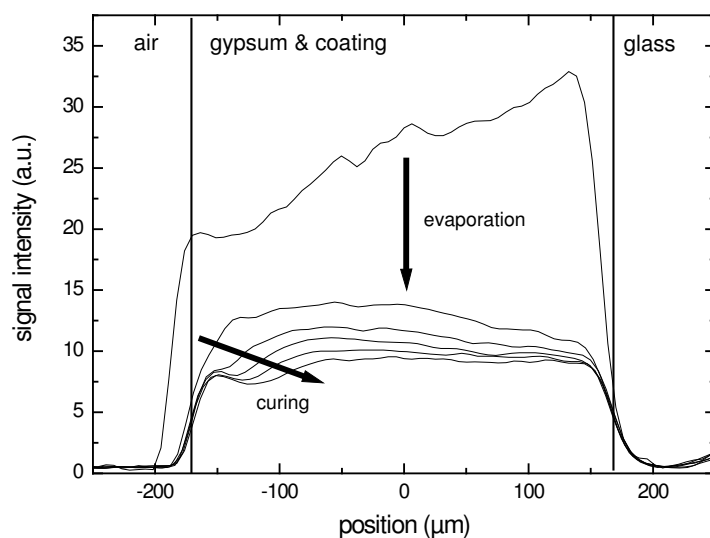
Fig. 8.6: Solvent-borne alkyd coating applied on a gypsum substrate. The NMR profiles are given every 3 h.
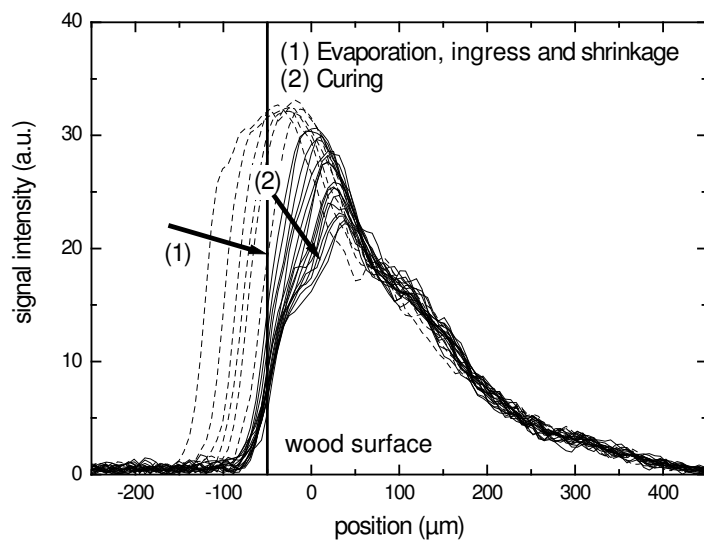
Fig. 8.7: Solvent-borne alkyd coating applied on a wooden substrate. The dashed NMR profiles show the penetration and evaporation of the coating. These profiles are given at $t = 0.3, 0.6, 1, 1.3, 1.6, 3.3$ h. The solid profiles are given every 1.7 h after the last dashed profile at $t = 3.3$ h. The vertical line shows the wood surface.

which slowly moves down into the wood.

8.4   Conclusions

The results presented in this chapter have shown that high spatial resolution MRI is an excellent tool to image the dynamical drying processes of alkyd coatings in and on porous substrates. Three drying stages could be visualized: the penetration of the coating in the substrate, the evaporation of the solvent, and the curing.

We have observed that the alkyd resin from the water-borne emulsion remained on top of the gypsum layer, whereas the water phase penetrated into the substrate. For the water-borne alkyd curing is observed both at the surface of the coating and at the coating/gypsum interface. The speed of the curing front on non-porous glass and on porous gypsum showed a clear dependency on the cobalt concentration. A minimum in front speed was found for a cobalt concentration of 0.07% Co mass/mass, which is commonly used concentration in alkyd coatings. When the coating was applied on a gypsum substrate instead of glass a higher front speed was found. Although a part of the cobalt catalyst was found in the substrate, the faster front speed observed on gypsum cannot be related to the observed higher front speeds. To explain the higher front speeds observed, we suggest that part of the Ca^{2+} ions of the gypsum are transported to the coating during the evaporation stage. This assumption is strengthened by a recent study, showing that the front speed increases when Ca/Zr are added as secondary driers, see chapter 6. Further experiments are needed to test this hypothesis, e.g., by monitoring the curing speed of water-borne coating on an inert porous substrate, such as glass.

For the solvent-borne alkyd coating the penetration of the coating inside the pine wood substrate was clearly visible, whereas also the curing process could be visualized inside the substrate as a function of depth.

The results unambiguously indicate that in order to optimize the overall coating performance one should explicitly take the effect of the underlying substrate into account.

9. Conclusions and outlook

Laat de toekomst uit de verf komen.
prof. dr. R.A.T.M. van Benthem (12 maart 2004)

9.1 Conclusions

In the previous chapters we have shown that NMR is a useful technique to image the curing process of alkyd coatings. To achieve the required depth resolution of 5 μm, even in samples with a short transverse relaxation time T_2, the NMR setup was designed to operate at a field of 1.4 T, with a gradient of 36.4 T/m. By using NMR in combination with additional techniques, like CRM, DSC, and mass measurements, we were able to distinguish the physical and chemical drying (curing) stage of alkyd coatings in our NMR measurements. NMR allows the complete drying process to be visualized, including the curing of the alkyd coating, even in non-transparent coatings.

It was found that the curing of alkyd coatings with a cobalt based catalyst is limited by diffusion of oxygen. This oxygen diffusion limitation results in a cross-linked layer (a skin), located on top of an uncross-linked layer of the coating. At the interface of these two layers cross-linking takes place. This cross-linking front is visible in the NMR data, and was observed to move with $\sqrt{t}$. The movement of this cross-linking front was modelled, resulting in an equation describing the observed behavior.

In solvent-borne alkyd coatings we found an additional effect, i.e., part of the NMR signal from the deeper regions below the cross-linking front decreases during the curing process. This behavior was explained by diffusion of a small amount of reactive species generated at the location of the front into deeper regions, where they subsequently react. When these species react cross-linking occurs and the NMR signal from the deeper regions in the coating decreases. This process of diffusion of reactive species has been described by a model, which predicts that the signal below the cross-linking front decreases proportional to $\sqrt{t}/L$, where L is the coating thickness. When the signal in the deeper regions is plotted as a function of $\sqrt{t}/L$, the data points indeed collapse on a single line. This is illustrated in figure 9.1. The cross-linking in deeper regions was only observed for solvent-borne systems, which are known to have a lower viscosity than water-borne systems. A lower viscosity implies a higher diffusion of reactive species and hence a possibility to cross-link in deeper regions. Both the model and the measurements indicate that the thickness of the coating is an important factor for the curing process. Consequently, for a correct interpretation of the data on the drying in low viscous alkyd coatings, knowledge of the coating thickness is absolutely necessary.

In our experiments the speed of the observed cross-linking front was found to depend
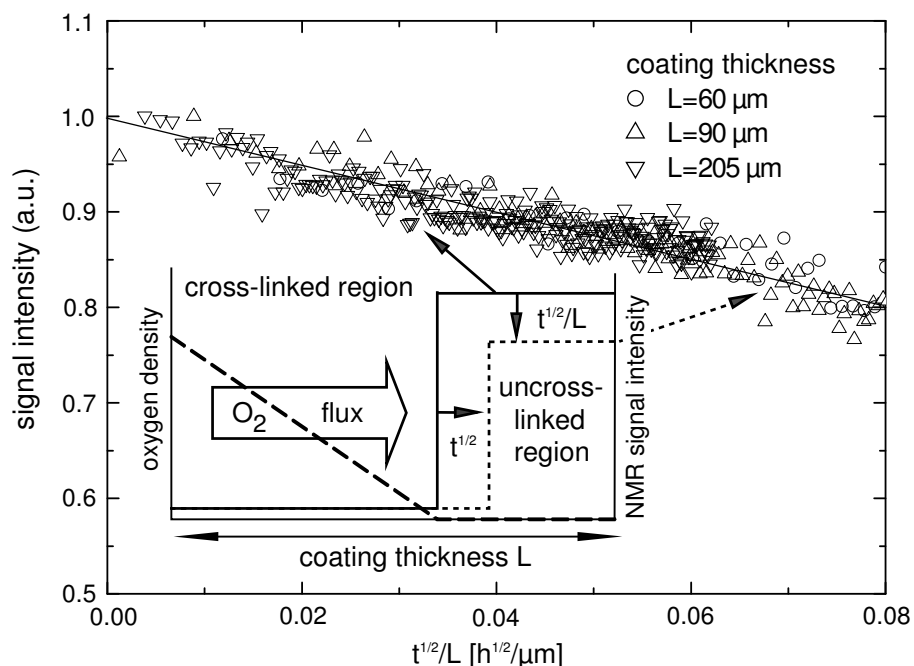
Fig. 9.1: Summary of the curing processes observed in solvent-borne alkyd coatings with Co or Co/Ca/Zr as driers. A front movement with the square root of time is observed, because of oxygen diffusion limitation. A signal decrease in the deeper region of the coating is observed because of slowly reacting species diffusing into this region, after which they react. This signal decrease scales with $\sqrt{t}$ and the inverse thickness of the coating ($1/L$).

on the catalyst concentration (see chapter 8 and [138]), addition of secondary driers such as Ca and Zr (see chapter 6), and the substrate (in our case gypsum, see chapter 8). These observations can be explained in terms of changes of the variables of the equation describing the front movement (Eq. 5.4), which are the oxygen solubility ρ_0 at the surface layer of the coating, the oxygen diffusion constant D, and the fully cross-linked volume per supplied mole of oxygen ν. However, the exact origin of these changes has not yet been completely identified.

In our experiments oxygen diffusion limitation and the resulting skin layer were only found for coatings with cobalt as a catalyst, which is the most commonly used catalyst in commercial alkyd paints. However, when manganese was used a more homogeneous and faster curing behavior was observed. A reaction-diffusion model combined with equations describing the NMR signal as a function of the degree of cross-linking was used to simulate the observed results. When a lower reaction constant and a higher diffusion constant was used in the simulations for manganese compared to the simulations of cobalt, the observed results were simulated correctly. Note that the typical $\sqrt{t}$ behavior observed for cobalt catalysts is a special case of the more general reaction-diffusion equations and is also observed in the corresponding simulations. For manganese as a catalyst, the higher diffusion constant, lower reaction constant, and the increase in T_2 indicate that the final completely cured coating is less densely cross-linked. Since the oxygen diffusion constant

is higher than for cobalt, the diffusion constant of water or other molecules may be higher as well. This might negatively affect the performance of the coating, for instance, because of a reduced resistance against water. This demonstrates that the use of NMR helps assessing the coating performance of alternative driers (like Mn and Fe) in real alkyd systems.

The effect of substrates on the curing of alkyd coatings was also investigated. With NMR the curing reactions could be visualized, on or even inside a substrate. The curing speed was found to be higher when the alkyd emulsion was applied on a gypsum substrate. From the NMR profiles also the depth of penetration is visible, which allows the adhesion properties to be related to the penetration of the porous substrate. From the results it can be concluded that for optimization of the overall coating performance one should explicitly take the substrate into account.

9.2 Outlook

Thus far we have focussed on the curing of alkyd coatings. However, the high resolution NMR imaging setup enables us to study a whole range of processes inside coatings or thin layers. In the following subsections, we will discuss the ability of the setup to probe, the moisture content and the moisture transport properties inside a coating, spatial variations in network structure which as a result can change the transport properties (e.g., multilayered systems), and finally we will discus the ability to probe fluorine containing coatings.

9.2.1 Moisture Transport

In this subsection we will show that high spatial resolution NMR is a valuable technique for studying moisture in coatings. Such a study is of interest for two reasons. First of all, environmental issues concerning the use of VOC's, see also chapter 1, have led to new reformulated water-borne coatings. These water-borne coatings should be (partly) hydrophilic while stored, but should be hydrophobic after application and drying. As a result they can be susceptible to moisture transport. Additionally, the moisture uptake and drying is determined by factors such as the pigment to volume concentration (CPVC), temperature, and relative humidity (RH), making it a very important topic for coating manufacturers [128, 132–134, 139–141]. Secondly, the NMR setup provides spatial information, whereas most other techniques only provide bulk information. With the NMR setup the water distribution and the water transport properties, such as diffusivity can be measured [34, 142]. In this section this will be illustrated by a measurement of the barrier property of a coating applied on a gypsum layer and a measurement showing the water uptake of a solvent-borne alkyd coating at a high relative humidity.

First, we measured the moisture transport through a water-borne alkyd emulsion applied on a gypsum layer. The results of these measurements are plotted in figure 9.2a. The acquisition of one profile took 10 minutes. The gypsum layer ($CaSO_4 \cdot 2H_2O$) was made from pure hemihydrate ($CaSO_4 \cdot \frac{1}{2}H_2O$), with a mass ratio water to binder of 0.66, resulting in a porosity of about 45% [135]. After the curing process was measured, a cylinder was
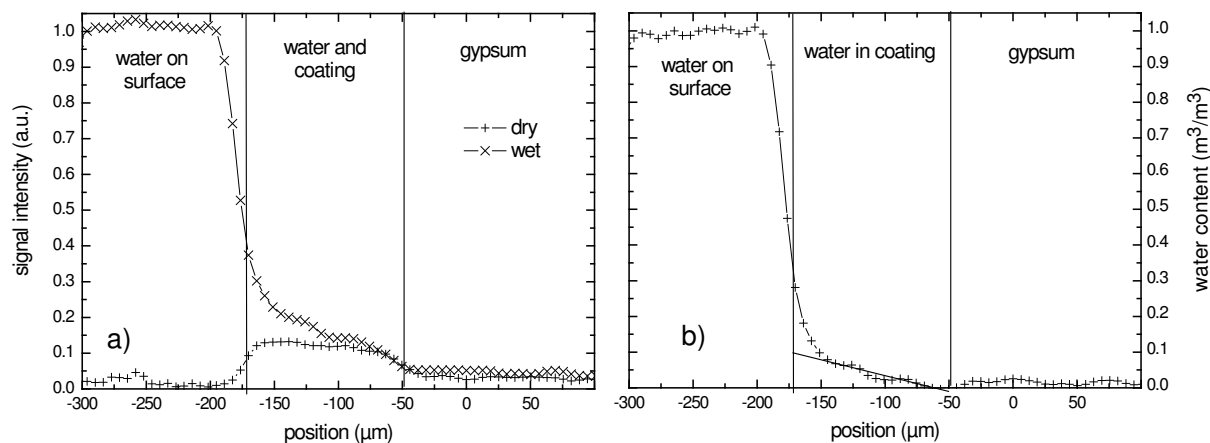
Fig. 9.2: NMR profile of a water-borne alkyd coating on top of a gypsum substrate. a) The
initially dry coating and gypsum layer and the system after applying water on top of
the coating. b) The water content obtained by subtracting the two curves plotted in
a).

glued on top of the coating and was filled with water. By subtracting the initial NMR
profiles of the dry coating and gypsum from the subsequent measurements, the moisture
content was calculated. The results are plotted in figure 9.2b. We observed that the water
penetrated the coating, and that within half an hour a steady-state situation was reached.
The coating acts as a moisture diffusion barrier to the gypsum. Once the water reaches
the gypsum it diffuses very fast and may eventually evaporate.

Secondly, a cured solvent-borne system was investigated that was equilibrated in an
environment with a 97.5% relative humidity at 20 °C. The NMR profiles are shown in
figure 9.3. The profiles were acquired every 10 minutes, and indicate that the sample equi-
librates within 30 minutes to the room temperature and humidity. The decrease in signal
suggests that water evaporates from the coating. However, when a high concentration of
water is present in a coating, this water might act as a plasticizing agent, which results
in an increase of the T_2 value and, consequently, the NMR signal intensity. Therefore,
calibration of the moisture content measured with NMR using additional techniques , e.g.,
mass-measurements, is required.

The two measurements presented here show that profiling the water content as a
function of time is possible. However, measuring low concentrations of water with a
good SNR and a sufficient time resolution for the particular wetting or drying process is a
problem. Fortunately, some possibilities exist to improve the SNR, e.g., by taking a larger
RF coil, or by addition of T_1 reducing ions (e.g. $CuSO_4$) to increase the experimental
repetition rate. Measurements of the diffusion coefficient as a function of position requires
a very long acquisition time (several hours), as a result the diffusion can only be measured
in steady-state situations or during slow processes.
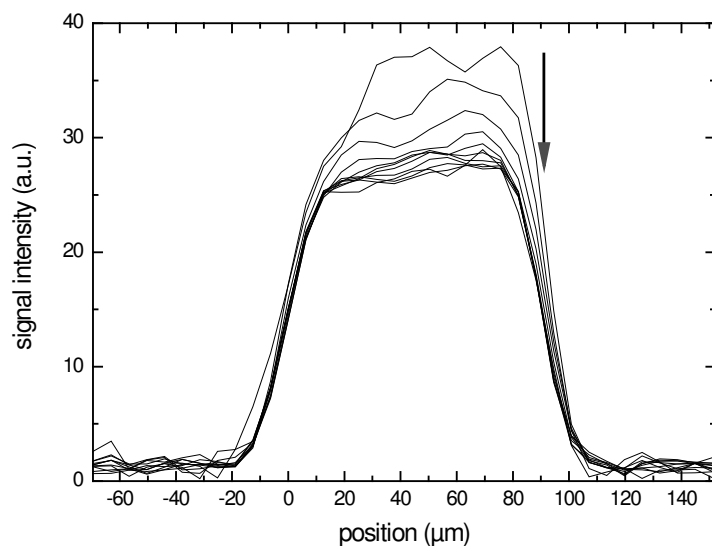
Fig. 9.3: NMR profiles of a solvent-borne alkyd coating. After equilibration in 97.5% RH at 20 °C, the coating was placed in the NMR setup. The profiles are acquired every 10 minutes.

9.2.2   Depth resolving the network structure

In this section we will show the possibilities of high resolution NMR imaging to probe network properties as a function of position. In general, with network properties one refers to cross-link density, chain branches, chain loops, network defects, and so on. The properties of the network determine in large extent the transport properties of the coating. There are several reasons why high resolution NMR imaging may be useful technique to probe network properties. First of all, a great interest exists in spatially resolving the network properties, because in many cases inhomogeneous networks are expected or present in coatings, e.g., UV curable coatings and drying alkyds. The second reason is the way in which NMR resolves network properties. From the NMR signal decay the polymer mobility can be obtained, and from the differences in mobility information on the network properties can be obtained. Other techniques only allow a characterization of physical properties of cured materials (macroscopic scale), or an analysis of chemical conversion (microscopic scale) [88].

We will now first demonstrate the ability to obtain information on the molecular mobility by analyzing the NMR relaxation of UV cured acrylate coatings. Next, we will briefly discuss the importance of nano-particles in coatings, and their influence on the network topology. Finally, we will show how -in principle- the glass transition temperature as a function of position can be measured.

Mw	n	$T_g \pm 2$ °C
700	12	-55
575	9-10	-30
302	4	33
258	2	64

Table 9.1: Average molecular weight of the PEGDA samples used to obtain different cross-link densities. n denotes the number of monomeric units of PEGDA: $CH_2=CO-[O-CH_2-CH_2]_n-O-CO=CH_2$. The glass transition temperature T_g is given for each coating after UV curing.
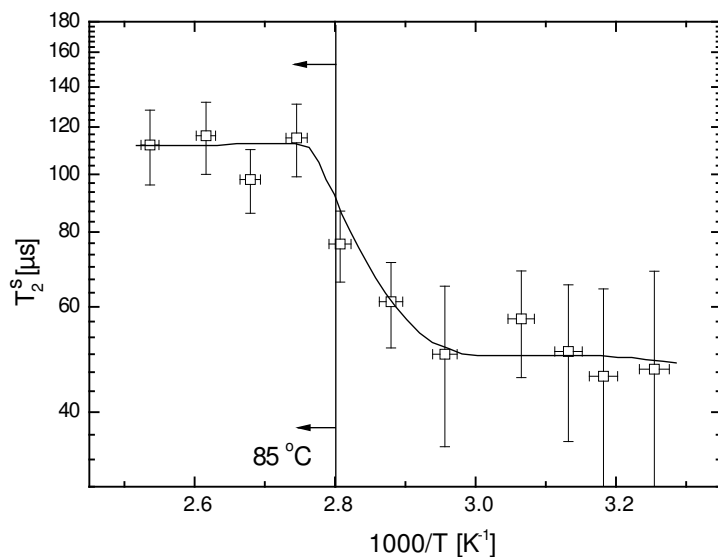
Fig. 9.4: Short relaxation time T_2^s against temperature T^{-1}. A plateau is observed above 85 °C.

UV cured acrylates

Some model UV curable acrylate systems are used for analyzing the network structure of a coating after UV curing, using the relaxation data obtained from the NMR signal decay. A photoinitiator is used to cure a di-functional poly(ethylene glycol) diacrylate (PEGDA). Curing of PEGDA results in a cross-linked network [88]. Four different PEGDA samples with different average molecular weights were used, resulting in UV cured coatings with different cross-link densities, see table 9.1.

In figure 9.4 the short relaxation time T_2^s obtained from a bi-exponential fit of the NMR signal decay is plotted as a function of reciprocal temperature. The transverse relaxation is governed by the interactions of near neighbors, which depend on the hydrogen mobility [86] and therefore also on the intra-chain mobility. At high temperatures, 60–150 °C above the glass-transition temperature, the mobility of the polymers becomes restricted by the cross-links and a plateau develops [88–90, 143]. At low temperatures the relaxation time T_2^s drops below the minimum value that can be determined in this setup. This value is roughly equal to the inter-echo spacing (50 μs in this case).
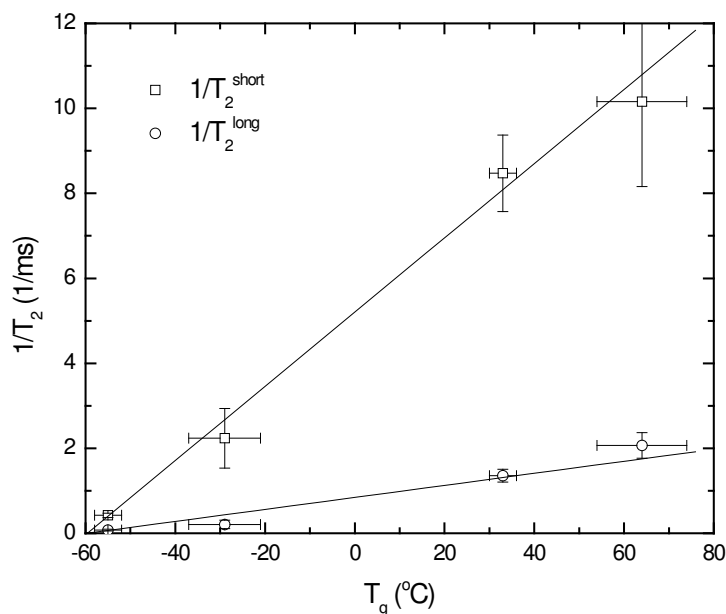
Fig. 9.5: T_2^{-1} against the glass transition temperature (T_g). The measurements are performed at 110 °C, far above the glass transition temperature.

In figure 9.5 the relaxation times T_2^s and T_2^l are plotted against the glass temperature for the different PEGDA samples. The samples are all measured well above the glass-transition temperature, which means that T_2 is determined by the cross-link density. The figure shows a very clear relation between T_2 and the glass transition temperature. For low cross-link densities the glass transition temperature is known to depend linearly on the cross-link density ρ_c [144]. Consequently, T_2 varies inversely with the cross-link density.

Nano particles

Many organic and inorganic particles are used as additives in coatings. When the added particles have dimensions below 100 nm, they are referred to as nano-particles. Much recent research on coatings is focussed on the use of nano-particles as additives. Nano-particles can be used to improve the mechanical properties of coatings but also to create electrical conductive coatings [145]. Conductive coatings have many applications, such as making conductive patterns by direct digital printing. New anti-static coatings can be developed for use on windows, screens, etc. The use of nanoscale particles with antibacterial properties in coatings is another example [146]. Because the distribution of nano-particles is not necessarily uniform and also affects the network properties, techniques that allow depth profiling are crucial for obtaining information on the distribution of these particles.

nr	T_g (°C)	ρ_c (mmol/cm^3)	T_2 (μs) at 22 °C
I	79	1.58	64 ± 10
II	69	0.98	96 ± 10
III	61	0.12	120 ± 10

Table 9.2: Three different polyurethane coatings produced with different cross-link densities (ρ_c), obtained from DMTA measurements. The relaxation times T_2 are measured at room temperature, far below the glass transition temperature T_g.

Multilayered systems

Often coatings are applied in multiple layers, each with its specific purpose, e.g., adhesion, barrier properties, color, and gloss. For example, automotive coatings consists generally of a base coat and a clear coat. We will now show that three consecutive layers with different glass transition temperatures applied on a substrate can be spatially resolved using our NMR equipment. This can be achieved by measuring T_2 as a function of temperature [143]. Three different polyurethane thermosetting coatings with different cross-link densities and glass transition temperatures were made. The cross-link density of each coating was determined by DMTA. The properties of the three layers are listed in table 9.2. Using the NMR setup the relaxation time T_2 was measured at room temperature for the three separate layers. Also a three layered sample was made by applying three consecutive layers on top of each other, each layer with a cross-link density equal to one of the three separate layers listed in table 9.2. This sample was depth profiled using NMR, and the results obtained at various temperatures are plotted in figure 9.6. Because the relaxation is very fast, part of the signal is already lost at the first moment of acquisition, which explains the difference in signal intensity for the different layers, assuming that the hydrogen density is the same in all layers. By increasing the temperature the polymer mobility increases and as a result the relaxation time increases, resulting in more signal. By investigating the signal intensity and relaxation times as a function of temperature in principle the glass transition temperature can be determined. One can clearly see that layer 3 has a much lower glass transition temperature, because at lower temperatures the signal of this layer significantly exceeds that of the other layers.

We conclude that by heating a coating information on the network (cross-link density and glass transition temperature) can be obtained as a function of depth. According to literature [88, 90], also swelling agents can be added to the coatings instead of heating, allowing network properties to be obtained from measurements at, for instance, room temperature.

9.2.3   Fluorine containing coatings

Next to hydrogen also fluorine is a sensitive nucleus for NMR. In this section we will discuss the importance of fluorine and the distribution of fluorine in coatings. Fluorine in coatings is used to reduce the adherence between a coating surface and possible contaminants. Reducing the adherence of contaminants is of major importance to retain the aesthetical properties of the coating [147, 148]. A reduced adherence can be achieved
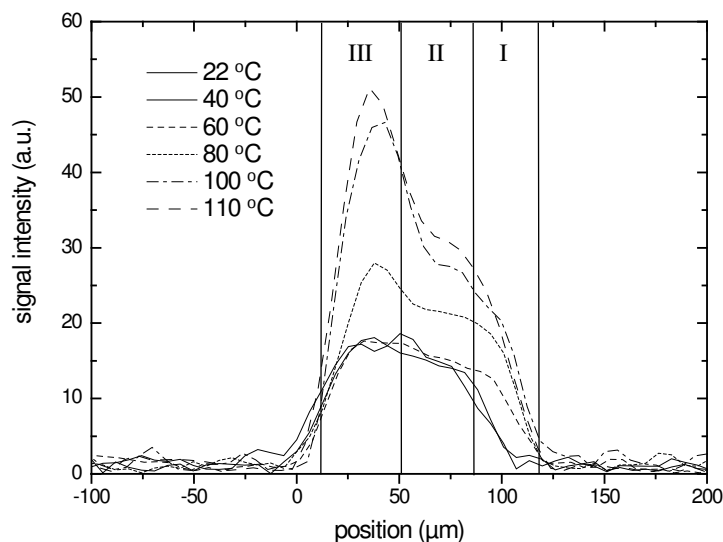
Fig. 9.6: NMR signal intensity as a function of position for a multilayered sample consisting of separate polyurethane layers applied on top of each other. The properties of each layer are listed in table 9.2.

by lowering the surface energy of the coating, making it easily cleanable. Addition of a small fraction of low surface energy species, such as perfluoroalkyl alcohols, will lead to a significantly lower surface tension of the film [147]. Only a small fraction is necessary, because these species will orient or move towards the air/film interface. This property has been used for preparation of so-called self-stratified low-adhesion coatings, in which an initially homogeneous formulation transforms into a layered film upon film formation. Previous research has shown a strong surface segregation of fluorinated species during film formation, and revealed that the fluorine rich layer is thin (around 20 nm [149, 150]). Upon mechanical abrasion, the coating will therefore sustain the low adherence only if the fluorine bulk level is sufficiently high.

Determining the fluorine distribution as a function of position is not straightforward. Techniques like confocal Raman spectroscopy and FTIR have a sensitivity that is not sufficient to probe the fluorine distribution as a function of depth. On the other hand, when the sensitivity is sufficient, the measurements are destructive and expensive, e.g. sputtering XPS [151]. High resolution NMR imaging may be a possible option, as will be demonstrated below.

Figure 9.7 shows the hydrogen and the fluorine profiles of two coatings placed on top of each other. One coating contains 1 mass % fluorine and the other 2 mass %. The hydrogen and fluorine signals are measured using a inter-echo time setting of 150 μs and a recording window of 130 μs, giving a spatial resolution of 5 μm. The sensitivity of fluorine is 80% of that of hydrogen. Because of the low concentration of fluorine, a huge amount of averages are needed (256000). It takes approximately 24 h to measure the fluorine profiles. Since an OW sequence is used, multiple echoes (and thus profiles) are measured to enhance the SNR as much as possible. However, the use of multiple echoes
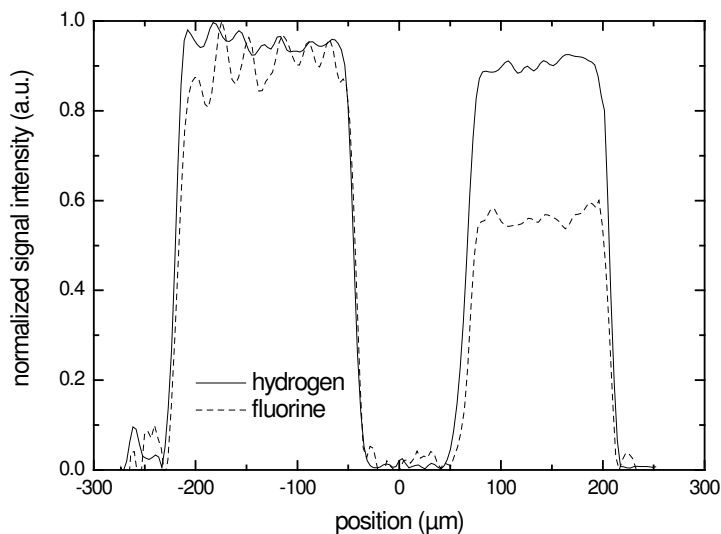
Fig. 9.7: Fluorine and hydrogen distribution obtained for samples containing 2% and 1% of fluorine, respectively.

is only possible if the relaxation time T_2 is long enough, which requires the measurement to be performed sufficiently far above the glass transition temperature T_g.

Our preliminary results indicate that NMR can be considered as a good alternative to determine the fluorine distribution. However, the measurement time is very long (about a day), which rules out the possibility to monitor various dynamic processes, such as the fluorine redistribution during drying of a coating.

9.2.4   Concluding remarks and recommendations

The examples presented in this section prove that high resolution NMR imaging is a promising technique to probe local properties. Using different NMR sequences, high spatial resolution MRI allows determination of hydrogen and fluorine densities, moisture diffusivity, and network structures, all as a function of time. Information on these properties is very valuable in research on transport processes in permeable media. Having this information available allows modelling of transport processes and can therefore be very helpful in predicting durability and performance of coatings.

The examples also indicate that for several future studies controlling the environmental conditions is important (e.g., relative humidity and temperature). Therefore, it would be very useful to equip the present NMR setup with a small climate chamber around the sample.

Appendix A: Off resonance excitation
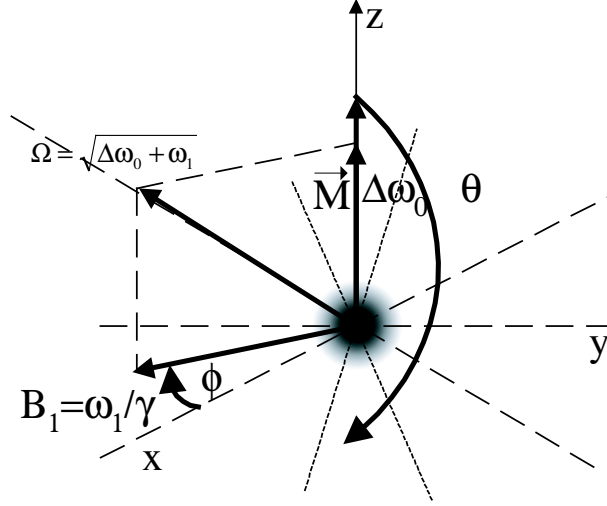
Fig. A.1: Excitation of a spin in an inhomogeneous field.

In a high magnetic field gradient, e.g., a stray field magnet (STRAFI) or a gradient at right angle to the magnetic field (GARFIELD) magnet, on resonance excitation does not apply. Due to the large static magnetic field gradient only the spins at the Larmor frequency are experiencing the correct rotation angle. Note that the center of the sample means the position at exactly the excitation frequency. Consider a spin displaced from that center inside the gradient by δy. Its frequency difference with respect to spins at the center is given by:

$$\Delta\omega_0 = \gamma G \delta y \tag{A.1}$$

This means that in the rotating frame of reference the spins located outside the center are still rotating. This is in fact always the case, but for low gradients these rotations can often be neglected. The effective rotation frequency is given by:

$$\Omega = \sqrt{\Delta\omega_0^2 + \omega_1^2}, \tag{A.2}$$

where $\omega_1 = \gamma B_1$, the excitation frequency. The precession axis is not located within the xy-plane but is tilted upwards to the z-axis, by an angle α, given by $\alpha = \arctan(\Delta\omega_0/\omega_1)$. A rotation over an angle $-\alpha$ to the xy-plane is given by:

$$R_{-\alpha} = \frac{1}{\Omega}\begin{pmatrix} \omega_1 & 0 & -\Delta\omega_0 \\ 0 & 0 & 0 \\ \Delta\omega_0 & 0 & \omega_1 \end{pmatrix}, \tag{A.3}$$

Therefore the effective rotation for any spin is given by:

$$R_{\phi,\theta,\alpha} = R_\alpha R_\phi R_\theta R_{-\phi} R_{-\alpha} =$$

$$
\begin{pmatrix}
\frac{\Delta\omega_0^2 \cos\theta + \omega_1^2(\cos^2\phi + \cos\theta \sin^2\phi)}{\Omega^2} & \frac{\cos\phi(\Delta\omega_0 \sin\theta + \omega_1(1-\cos\theta)\sin\phi)}{\Omega} & \frac{\Omega^2 \sin\theta \sin\phi - 2\Delta\omega\omega_1 \cos^2\phi \sin^2\frac{\theta}{2}}{\Omega^2} \\
\frac{\cos\phi(-\Delta\omega_0 \sin\theta + \omega_1(1-\cos\theta)\sin\phi)}{\Omega} & \cos\theta \cos^2\phi + \sin^2\phi & -\frac{\cos\phi(\Delta\omega_0(1-\cos\phi)\sin\phi + \omega_1 \sin\theta)}{\Omega} \\
\frac{-\Omega^2 \sin\theta \sin\phi - 2\Delta\omega\omega_1 \cos^2\phi \sin^2\frac{\theta}{2}}{\Omega^2} & \frac{\cos\phi(-\Delta\omega_0(1-\cos\phi)\sin\phi + \omega_1 \sin\theta)}{\Omega} & \frac{\Delta\omega_0^2(\cos^2\phi + \cos\theta \sin^2\phi) + \omega_1^2 \cos\theta}{\Omega^2}
\end{pmatrix}
$$

$$(A.4)$$

This rotation matrix can be implemented to simulate excitation in inhomogeneous fields [112]. Using the common transformation $M_+ s = M_x + iM_y$ and $M_- = M_x - iM_y$ (see matrices A.5), discrimination between rephasing and dephasing configuration can be achieved. The rotation matrix for the vector $\vec{M} = (M_+, M_-, M_z)$ is than given by $R^*_{\phi,\theta,\alpha} = TR_\alpha R_\phi R_\theta R_{-\phi} R_{-\alpha} T^*$. Using coherent pathways [112] (also called theory of configuration [106]), spin echo intensities and shapes can be calculated. Using simulation programs based on rotation, relaxation, and diffusion matrices allows data to interpreted more easily.

$$
T = \begin{pmatrix} 1 & i & 0 \\ 1 & -i & 0 \\ 0 & 0 & 1 \end{pmatrix}, \quad T^* = \begin{pmatrix} \frac{1}{2} & \frac{1}{2} & 0 \\ \frac{1}{2i} & \frac{-1}{2i} & 0 \\ 0 & 0 & 1 \end{pmatrix} \tag{A.5}
$$

References

[1] R. Lambourne and T. A. Strivens. *Paint and surface coatings : theory and practice.* Woodhead, Cambridge, 2nd edition, 1999.

[2] R. van der Linde. *Coatingtechnologie : kunst, ambacht, wetenschap.* Inaugural lecture, Technische Universiteit Eindhoven, 1996.

[3] K. D. Weiss. Paint and coatings: A mature industry in transition. *Progress in Polymer Science*, 22(2):203–245, 1997.

[4] *A profile of the European paint industry.* IRL (Information Research Limited), 12th edition edition, 1998.

[5] R. H. Kienle and C. S. Ferguson. Alkyd resins as film-forming materials. *Industrial and Engineering Chemistry*, 21:349, 1929.

[6] I. Bockelmann, E. A. Pfister, B. Peters, and S. Duchstein. Psychological effects of occupational exposure to organic solvent mixtures on printers. *Disability and Rehabilitation*, 26(13):798–807, 2004.

[7] I. Bockelmann, H. Lindner, B. Peters, and E. A. Pfister. Influence of long term occupational exposure to solvents on colour vision. *Ophthalmologe*, 100(2):133–141, 2003.

[8] I. Bockelmann, S. Darius, N. McGauran, B. P. Robra, B. Peter, and E. A. Pfister. The psychological effects of exposure to mixed organic solvents on car painters. *Disability and Rehabilitation*, 24(9):455–461, 2002.

[9] S. R. Steinhauer, L. A. Morrow, R. Condray, and A. J. Scott. Respiratory sinus arrhythmia in persons with organic solvent exposure: Comparisons with anxiety patients and controls. *Archives of Environmental Health*, 56(2):175–180, 2001.

[10] R. Condray, L. A. Morrow, S. R. Steinhauer, M. Hodgson, and M. Kelley. Mood and behavioral symptoms in individuals with chronic solvent exposure. *Psychiatry Research*, 97(2-3):191–206, 2000.

[11] E. Pfister, I. Bockelmann, S. Darius, and C. Wurthmann. Diagnosis of early toxic effects of lead or mixed organic solvents - inclusion of psychopathological methods. *Fortschritte der Neurologie Psychiatrie*, 67(10):435–440, 1999.

[12] L. A. Morrow and S. R. Steinhauer. Alterations in heart-rate and pupillary response in persons with organic-solvent exposure. *Biological Psychiatry*, 37(10):721–730, 1995.

[13] J. F. Hoogervorst. Wijziging arbeisomstandighedenregeling betreffende werkzaamheden met vluchtige organische stoffen. *Staatscourant*, 2001.

[14] M. Rutte. Wijziging arbeisomstandighedenregeling. *Staatscourant*, 2004.

[15] European Commission. *Registration, evaluation and authorization of chemicals (REACH)*. http://europa.eu.int/comm/environment/chemicals, 2003.

[16] D. Lison, M. de Boeck, V. Verougstraete, and M. Kirsch-Volders. Update on the genotoxicity and carcinogenicity of cobalt compounds. *Occupational and Environmental Medicine*, 58(10):619–625, 2001.

[17] J. R. Bucher, J. R. Hailey, J. R. Roycroft, J. K. Haseman, R. C. Sills, S. L. Grumbein, P. W. Mellick, and B. J. Chou. Inhalation toxicity and carcinogenicity studies of cobalt sulfate. *Toxicological Sciences*, 49(1):56–67, 1999.

[18] M. de Boeck, M. Kirsch-Volders, and D. Lison. Cobalt and antimony: genotoxicity and carcinogenicity. *Mutation Research*, 533(1-2):135–152, 2003.

[19] J. H. Bieleman. Progress in the development of cobalt-free drier systems. *Macromolecular Symposia*, 187:811–821, 2002.

[20] E. Staring, A. A. Dias, and R. A. T. M. van Benthem. New challenges for r&d in coating resins. *Progress in Organic Coatings*, 45(2-3):101–117, 2002.

[21] R. A. T. M. van Benthem. *Coating technologie laat de toekomst uit de verf komen*. Inaugural lecture, Technische Universiteit Eindhoven, 2004.

[22] M. Wallin, P. M. Glover, A. C. Hellgren, J. L. Keddie, and P. J. McDonald. Depth profiles of polymer mobility during the film formation of a latex dispersion undergoing photoinitiated cross-linking. *Macromolecules*, 33(22):8443–8452, 2000.

[23] W. Schrof, E. Beck, R. Koniger, W. Reich, and R. Schwalm. Depth profiling of uv cured coatings containing photostabilizers by confocal raman microscopy. *Progress in Organic Coatings*, 35(1-4):197–204, 1999.

[24] W. Schrof, E. Beck, G. Etzrodt, H. Hintze-Bruning, U. Meisenburg, R. Schwalm, and J. Warming. Depth-resolved characterization of uv cured coatings by confocal raman and two-photon microscopy. *Progress in Organic Coatings*, 43(1-3):1–9, 2001.

[25] S. K. Basu, L. E. Scriven, L. F. Francis, and A. V. McCormick. Mechanism of wrinkle formation in curing coatings. *Progress in Organic Coatings*, 53(1):1–16, 2005.

[26] C. A. Froud, I. P. Hayward, and J. Laven. Advances in the raman depth profiling of polymer laminates. *Applied Spectroscopy*, 57(12):1468–1474, 2003.

[27] P. M. Glover, P. S. Aptaker, J. R. Bowler, E. Ciampi, and P. J. McDonald. A novel high-gradient permanent magnet for the profiling of planar films and coatings. *Journal of Magnetic Resonance*, 139(1):90–97, 1999.

[28] P. J. McDonald and B. Newling. Stray field magnetic resonance imaging. *Reports on Progress in Physics*, 61(11):1441–1493, 1998.

[29] G. Eidmann, R. Savelsberg, P. Blumler, and B. Blumich. The nmr mouse, a mobile universal surface explorer. *Journal of Magnetic Resonance Series A*, 122(1):104–109, 1996.

[30] M. Clark and J. Boon. Molart, a multidisciplinary priority nwo project on molecular aspects of aging in painted works of art. Report, 2002.

[31] M. Visschers, J. Laven, and R. van der Linde. Forces operative during film formation from latex dispersions. *Progress in Organic Coatings*, 31:311–323, 1997.

[32] M. Visschers, J. Laven, and A. L. German. Current understanding of the deformation of latex particles during film formation. *Progress in Organic Coatings*, 30(1-2): 39–49, 1997.

[33] M. Visschers, J. Laven, and R. van der Linde. Film formation from latex dispersions. *Journal of Coatings Technology*, 73(916):49–55, 2001.

[34] J. P. Gorce, D. Bovey, P. J. McDonald, P. Palasz, D. Taylor, and J. L. Keddie. Vertical water distribution during the drying of polymer films cast from aqueous emulsions. *European Physical Journal E: Soft Matter*, 8(4):421–429, 2002.

[35] E. Ciampi and P. J. McDonald. Skin formation and water distribution in semicrystalline polymer layers cast from solution: A magnetic resonance imaging study. *Macromolecules*, 36(22):8398–8405, 2003.

[36] J. L. Keddie, J.-P. Gorce, J. Mallegol, and P. J. McDonald. Understanding waterborne coatings: New techniques to answer old questions. *Surface Coatings International Part A*, 2003(2):70, 2003.

[37] J. M. Salamanca, E. Ciampi, D. A. Faux, P. M. Glover, P. J. McDonald, A. F. Routh, A. C. I. A. Peters, R. Satguru, and J. L. Keddie. Lateral drying in thick films of waterborne colloidal particles. *Langmuir*, 17(11):3202–3207, 2001.

[38] E. Ciampi, U. Goerke, J. L. Keddie, and P. J. McDonald. Lateral transport of water during drying of alkyd emulsions. *Langmuir*, 16(3):1057–1065, 2000.

[39] W. O. Lundberg, F. Scofield, F. M. Greenawald, and E. B. Fitzgerald. Panel discussion on mechanism of drier action. *Industrial and Engineering Chemistry*, 46(3): 570–572, 1954.

[40] J Laven and U. K. Uravind. The chemical drying process in alkyd emulsion paint films. Athens Conference on Coatings Science and Technology, Jul 2003.

[41] B. Marton. *A depth-resolved look at the film formation and properties of alkyd-based coatings*. Ph.D. Thesis, University of Twente, 2004.

[42] N. A. Porter, B. A. Weber, H. Weenen, and J. A. Khan. Autoxidation of polyunsaturated lipids. factors controlling the stereochemistry of product hydroperoxides. *Journal of the American Chemical Society*, 102(17):5597, 1980.

[43] N. A. Porter, S. Lehman, B. A. Weber, and K. J. Smith. Unified mechanism for polyunsaturated fatty acid autoxidation. competition of peroxy radical hydrogen atom abstraction, -scission, and cyclization. *Journal of the American Chemical Society*, 103:6447–6455, 1981.

[44] N. A. Porter and D. G. Wujek. Autoxidation of polyunsaturated fatty acids, an expanded mechanistic study. *Journal of the American Chemical Society*, 106:2626–2629, 1984.

[45] N. A. Porter, K. A. Mills, and R. L. Carter. A mechanistic study of oleate autoxidation - competing peroxyl h-atom abstraction and rearrangement. *Journal of the American Chemical Society*, 116(15):6690–6696, 1994.

[46] J. C. Hubert, R. A. M. Venderbosch, W. J. Muizebelt, R. P. Klaasen, and K. H. Zabel. Mechanistic study of drying of alkyd resins using (z,z)- and (e,e)-3,6-nonadiene as model substances. *Progress in Organic Coatings*, 31(4):331–340, 1997.

[47] J. C. Hubert, R. A. M. Venderbosch, W. J. Muizebelt, R. P. Klaasen, and K. H. Zabel. Singlet oxygen drying of alkyd resins and model compounds. *Journal of Coatings Technology*, 69(869):59–64, 1997.

[48] W. J. Muizebelt, J. J. Donkerbroek, M. W. F. Nielen, J. B. Hussem, M. E. F. Biemond, R. P. Klaasen, and K. H. Zabel. Oxidative crosslinking of alkyd resins studied with mass spectrometry and nmr using model compounds. *Journal of Coatings Technology*, 70(876):83–93, 1998.

[49] W. J. Muizebelt, J. C. Hubert, M. W. F. Nielen, R. P. Klaasen, and K. H. Zabel. Crosslink mechanisms of high-solids alkyd resins in the presence of reactive diluents. *Progress in Organic Coatings*, 40(1-4):121–130, 2000.

[50] J. Mallegol, L. Gonon, S. Commereuc, and V. Verney. Thermal (dsc) and chemical (iodometric titration) methods for peroxides measurements in order to monitor drying extent of alkyd resins. *Progress in Organic Coatings*, 41(1-3):171–176, 2001.

[51] W. J. Muizebelt and M. W. F. Nielen. Oxidative crosslinking of unsaturated fatty acids studied with mass spectrometry. *Journal of Mass Spectrometry*, 31(5):545–554, 1996.

[52] J. K. Wise. Introduction - mechanism of drier action. *Industrial and Engineering Chemistry*, 46(3):562–562, 1954.

[53] E. R. Mueller. Proposal - mechanism of drier action. *Industrial and Engineering Chemistry*, 46(3):562–569, 1954.

[54] J. H. Bieleman. *Additives for Coatings*. Wiley-VCH, Weinheim, 2000.

[55] N. A. Porter. Mechanisms for the autoxidation of polyunsaturated lipids. *Accounts of Chemical Research*, 19:262–268, 1986.

[56] N. I. Krinsky. Antioxidant functions of carotenoids. *Free Radical Biology and Medicine*, 7(6):617–635, 1989.

[57] N. I. Krinsky. Mechanism of action of biological antioxidants. *Proceedings of the Society for Experimental Biology and Medicine*, 200(2):248–254, 1992.

[58] Z. O. Oyman, W. Ming, and R. van der Linde. Oxidation of drying oils containing non-conjugated and conjugated double bonds catalyzed by a cobalt catalyst. *Progress in Organic Coatings*, 54(3):198–204, 2005.

[59] C. Stenberg, M. Svensson, E. Wallstrom, and M. Johansson. Drying of linseed oil wood coatings using reactive diluents. *Surface Coatings International Part B-Coatings Transactions*, 88(2):119–126, 2005.

[60] C. Stenberg, M. Svensson, and M. Johansson. Study of the drying of linseed oils with different fatty acid patterns using rtir-spectroscopy and chemiluminescence (cl). *Industrial Crops and Products*, 21(2):263–272, 2005.

[61] J. Samuelsson and M. Johansson. Oxidation of fa with alkene or alkyne functionalities studied with chemiluminescence and real-time ir spectroscopy. *Journal of the American Oil Chemists Society*, 80(5):491–496, 2003.

[62] S. M. P. Meneghetti, R. F. de Souza, A. L. Monteiro, and M. O. de Souza. Substitution of lead catalysts by zirconium in the oxidative polymerization of linseed oil. *Progress in Organic Coatings*, 33(3-4):219–224, 1998.

[63] R. W. Hein. Driers for waterborne coatings. *Journal of Coatings Technology*, 70 (886):19–22, 1998.

[64] R. W. Hein. Driers for high-solids coatings. *Journal of Coatings Technology*, 71 (898):21–25, 1999.

[65] F. Haber and J Weiss. The catalytic decomposition of hydrogen peroxide by iron salts. *Proceedings of the Royal Society of London. Series A, Mathematical and Physical Sciences*, 147(861):332–351, 1934.

[66] W. A. Waters. The kinetics and mechanism of metal-catalyzed autoxidation. *Journal of the American Oil Chemists Society*, 48:427, 1971.

[67] J. Mallegol, J. Lemaire, and J. L. Gardette. Drier influence on the curing of linseed oil. *Progress in Organic Coatings*, 39(2-4):107–113, 2000.

[68] J. Mallegol, A. M. Barry, E. Ciampi, P. M. Glover, P. J. McDonald, J. L. Keddie, M. Wallin, A. Motiejauskaite, and P. K. Weissenborn. Influence of drier combination on through-drying in waterborne alkyd emulsion coatings observed with magnetic resonance profiling. *Journal of Coatings Technology*, 74(933):113–124, 2002.

[69] G. Ostberg, B. Bergenstahl, and K. Sorenssen. Distribution of driers between the alkyd and aqueous phase in alkyd emulsions and its relation to drying properties. *Journal of Coatings Technology*, 64(814):33–43, 1992.

[70] R. van Gorkum and E. Bouwman. The oxidative drying of alkyd paint catalysed by metal complexes. *Coordination Chemistry Reviews*, 249(17-18):1709–1728, 2005.

[71] Z. O. Oyman, W. Ming, and R. van der Linde. Oxidation of model compound emulsions for alkyd paints under the influence of cobalt drier. *Progress in Organic Coatings*, 48:80–91, 2003.

[72] Z. O. Oyman, W. Ming, F. Micciche, E. Oostveen, J. van Haveren, and R. van der Linde. A promising environmentally-friendly manganese-based catalyst for alkyd emulsion coatings. *Polymer*, 45(22):7431–7436, 2004.

[73] R. van Gorkum, E. Bouwman, and J. Reedijk. Fast autoxidation of ethyl linoleate catalyzed by [mn(acac)(3)] and bipyridine: A possible drying catalyst for alkyd paints. *Inorganic Chemistry*, 43(8):2456–2458, 2004.

[74] F. Micciche, E. Oostveen, J. van Haveren, and R. van der Linde. The combination of reducing agents/iron as environmentally friendlier alternatives for co-based driers in the drying of alkyd paints. *Progress in Organic Coatings*, 53(2):99–105, 2005.

[75] G. W. H. Hohne, W. F. Hemminger, and H.-J. Flammersheim. *Differential scanning calorimetriy*. Springer-Verlag, Heidelberg, second edition, 2003.

[76] W. Denk, J. H. Strickler, and W. W. Webb. 2-photon laser scanning fluorescence microscopy. *Science*, 248(4951):73–76, 1990.

[77] M. W. Urban. Surfactants in latex films; interactions with latex components and quantitative analysis using atr and step-scan pas ft-ir spectroscopy. *Progress in Organic Coatings*, 32(1-4):215–229, 1997.

[78] M. W. Urban. Three-dimensional compositional gradients in water-borne urethanes and latexes: spectroscopic approaches. *Progress in Organic Coatings*, 40(1-4):195–202, 2000.

[79] M. W. Urban. Depth-profiling studies of double-layer pvf2-on-pet films by fourier transform infrared photoacoustic spectroscopy. *Applied Spectroscopy*, 40(7):994, 1986.

[80] A. Rosencwaig and A. Gersho. Theory of photoacoustic effect with solids. *Journal of Applied Physics Letters*, 47(1):64–69, 1976.

[81] W. Pauli. Zur frage der theoretischen deutung der satelliten einiger spektrallinien und ihrer beeinflussung durch magnetische felder. *Naturwissenschaften*, 12(37):741–743, 1924.

[82] F. Bloch. Nuclear induction. *Physical Review*, 70:460, 1946.

[83] F. Bloch, W. W. Hansen, and M. Packard. The nuclear induction experiment. *Physical Review*, 70:474, 1946.

[84] E. M. Purcell, E. C. Torrey, and R. V. Pound. Resonance absorption by nuclear magnetic moments in a solid. *Physical Review*, 69:37–38, 1946.

[85] P. C. Lauterbur. Image formation by induced local interactions: Examples employing nuclear magnetic resonance. *Nature*, 242:190–191, 1973.

[86] N. Bloembergen, E. M. Purcell, and R. V. Pound. Relaxation effects in nuclear magnetic resonance absorption. *Physical Review*, 73:679–712, 1948.

[87] M. Doi and S. F. Edwards. *The theory of polymer dynamics*. International series of monographs on physics. Oxford University Press Inc., New York, 1986.

[88] V. M. Litvinov and A. A. Dias. Analysis of network structure of uv-cured acrylates by h-1 nmr relaxation, c-13 nmr spectroscopy, and dynamic mechanical experiments. *Macromolecules*, 34(12):4051–4060, 2001.

[89] Y. Y. Gotlib. Proton magnetic relaxation in concentrated polymethylmethacrylate solutions. *Polymer Science U. S. S. R.*, 17(8):1850, 1975.

[90] Y. Y. Gotlib. Influence of the chemical cross-link network on spin-spin relaxation in swollen cross-linked polymer systems. *Polymer Science U. S. S. R.*, 18(10):2299–3003, 1976.

[91] R. Kimmich and H. W. Weber. Nuclear magnetic-relaxation spectroscopy of polymers and anomalous segment diffusion - reorientations mediated by translational displacements. *Journal of Chemical Physics*, 98(7):5847–5854, 1993.

[92] R. Kimmich and N. Fatkullin. Polymer chain dynamics and nmr. *Advances in Polymer Science*, 170:1–113, 2004.

[93] R. Kimmich, N. Fatkullin, C. Mattea, and E. Fischer. Polymer chain dynamics under nanoscopic confinements. *Magnetic Resonance Imaging*, 23(2):191–196, 2005.

[94] N. Fatkullin and R. Kimmich. Nuclear-spin-lattice relaxation dispersion and segment diffusion in entangled polymers - renormalized rouse formalism. *Journal of Chemical Physics*, 101(1):822–832, 1994.

[95] E. Fischer, R. Kimmich, and N. Fatkullin. Nmr field gradient diffusometry of segment displacements in melts of entangled polymers. *Journal of Chemical Physics*, 104(22):9174–9178, 1996.

[96] E. Fischer, R. Kimmich, and N. Fatkullin. Spin diffusion in melts of entangled polymers. *Journal of Chemical Physics*, 106(23):9883–9888, 1997.

[97] P. J. McDonald. Stray field magnetic resonance imaging. *Progress in Nuclear Magnetic Resonance Spectroscopy*, 30(1-2):69–99, 1997.

[98] B. Blumich, P. Blumler, G. Eidmann, A. Guthausen, R. Haken, U. Schmitz, K. Saito, and G. Zimmer. The nmr-mouse: Construction, excitation, and applications. *Magnetic Resonance Imaging*, 16(5-6):479–484, 1998.

[99] B. Blumich, V. Anferov, S. Anferova, M. Klein, R. Fechete, M. Adams, and F. Casanova. Simple nmr-mouse with a bar magnet. *Concepts in Magnetic Resonance*, 15(4):255–261, 2002.

[100] B. Blumich, V. Anferov, S. Anferova, M. Klein, and R. Fechete. An nmr-mouse (r) for analysis of thin objects. *Macromolecular Materials and Engineering*, 288(4): 312–317, 2003.

[101] B. Blumich, P. Blumler, A. Guthausen, C. Fulber, G. Eidmann, and R. Savelsberg. Spatially resolved analysis of crosslink densities by nmr. *Kautschuk Gummi Kunststoffe*, 50(7-8):560–563, 1997.

[102] B. Blumich and A. M. Bruder. Mobile nmr for quality of elastomer products. *Kautschuk Gummi Kunststoffe*, 56(3):90–94, 2003.

[103] B. Blumich, S. Anferova, K. Kremer, S. Sharma, V. Herrmann, and A. Segre. Unilateral nuclear magnetic resonance for quality control - the nmr-mouse. *Spectroscopy*, 18(2):18, 2003.

[104] A. Abragam. *Principles of Nuclear Magnetism*. Oxford Science Publications, New York, 1961.

[105] C. P. Slichter. *Principles of Magnetic Resonance*. Springer-Verlag, Berlin, third edition, 1963.

[106] M. T. Vlaardingerbroek and J. A. den Boer. *Magnetic Resonance Imaging*. Springer-Verlag, New York, third edition, 2003.

[107] P. T. Callaghan. *Principles of Nuclear Magnetic Resonance Microscopy*. Oxford University Press, 1993.

[108] E. M. Haacke, R. W. Brown, M. R. Thompson, and R. Venkatesan. *Magnetic Resonance Imaging*. John Wiley and Sons, 1999.

[109] E. D. Ostroff and J. S. Waugh. Multiple spin echoes and spin locking in solids. *Physical Review Letters*, 16(24):1097–1098, 1966.

[110] M. D. Hurlimann. Optimization of timing in the carr-purcell-meiboom-gill sequence. *Magnetic Resonance Imaging*, 19(3/4):375–378, 2001.

[111] K. Adamsons. Chemical surface characterization and depth profiling of automotive coating systems. *Progress in Polymer Science*, 25(9):1363–1409, 2000.

[112] M. D. Hurlimann. Diffusion and relaxation effects in general stray field nmr experiments. *Journal of Magnetic Resonance*, 148(2):367–378, 2001.

[113] S. W. Provencher. Contin: a general purpose constrained regularization program for inverting noisy linear algebraic and integral equations. *Computer Physics Communications*, 27(3):229–242, 1982.

[114] P. G. Klein and M. E. Ries. The dynamics and physical structure of polymers above the glass transition-transverse relaxation studies of linear chains, star polymers and networks. *Progress in Nuclear Magnetic Resonance Spectroscopy*, 42(1-2):31–52, 2003.

[115] A. C. Hellgren, M. Wallin, P. K. Weissenborn, P. J. McDonald, P. M. Glover, and J. L. Keddie. New techniques for determining the extent of crosslinking in coatings. *Progress in Organic Coatings*, 43(1-3):85–98, 2001.

[116] G. Bennett, J. P. Gorce, J. L. Keddie, P. J. McDonald, and H. Berglind. Magnetic resonance profiling studies of the drying of film-forming aqueous dispersions and glue layers. *Magnetic Resonance Imaging*, 21(3/4):235–241, 2003.

[117] S. J. F. Erich, J. Laven, L. Pel, H. P. Huinink, and K. Kopinga. Comparison of nmr and confocal raman microscopy as coatings research tools. *Progress in Organic Coatings*, 52(3):210–216, 2005.

[118] N. J. Everall. Confocal raman microscopy: Why the depth resolution and spatial accuracy can be much worse than you think. *Applied Spectroscopy*, 54(10):1515–1520, 2000.

[119] N. J. Everall. Raman spectroscopy coatings research and analysis: Part i. basic principles. *Journal of Coatings Technology*, 2(19):38–44, 2005.

[120] N. J. Everall. Raman spectroscopy in coatings research and analysis: Part ii. practical applications. *Journal of Coatings Technology*, 2(20):46–52, 2005.

[121] S. J. F. Erich, J. Laven, L. Pel, H. P. Huinink, and K. Kopinga. Dynamics of cross linking fronts in alkyd coatings. *Applied Physics Letters*, 86(13):134105, 2005.

[122] Z. O. Oyman. *Towards Environmentally Friendly Catalysts For Alkyd Coatings*. Ph.D. Thesis, Technische Universiteit Eindhoven, 2005.

[123] P. Mansfield and D. Ware. Nmr spin dynamics in solids. i. artificial line narrowing and zeeman spin-spin relaxation in the rotating frame. *Physical Review*, 168(2):318, 1968.

[124] B. Marton, L. G. J. van der Ven, C. Otto, N. Uzunbajakava, M. A. Hempenius, and G. J. Vancso. A depth-resolved look at the network development in alkyd coatings by confocal raman microspectroscopy. *Polymer*, 46(25):11330–11339, 2005.

[125] H. Landolt and R. Boernstein. *Zahlenwerte und Funktionen aus Physik, Chemie, Astronomie, Geophysik und Technik*, volume IV. Springer, Berlin, 6 edition, 1980.

[126] E. I. Hormats and F. C. Unterleitner. Measurement of the diffusion of oxygen in polymers by phosphorescent quenching. *Journal of Physical Chemistry*, 69(11): 3677–3681, 1965.

[127] L. Audouin, V. Langlois, J. Verdu, and J. C. M. Debruijn. Role of oxygen diffusion in polymer aging - kinetic and mechanical aspects. *Journal of Materials Science*, 29(3):569–583, 1994.

[128] M. de Meijer and H. Militz. Moisture transport in coated wood. part 1: Analysis of sorption rates and moisture content profiles in spruce during liquid water uptake. *Holz Als Roh-und Werkstoff*, 58(5):354–362, 2000.

[129] S. L. Bardage and J. Bjurman. Adhesion of waterborne paints to wood. *Journal of Coatings Technology*, 70(878):39–47, 1998.

[130] R. M. Nussbaum. Penetration of water-borne alkyd emulsions and solvent-borne alkyds into wood - autoradiographic and sem-edxa studies. *Holz Als Roh-und Werkstoff*, 52(6):389–393, 1994.

[131] R. M. Nussbaum, E. J. Sutcliffe, and A. C. Hellgren. Microautoradiographic studies of the penetration of alkyd, alkyd emulsion and linseed oil coatings into wood. *Journal of Coatings Technology*, 70(878):49–57, 1998.

[132] N. L. Thomas. The barrier properties of paint coatings. *Progress in Organic Coatings*, 19(2):101–121, 1991.

[133] G. K. van der Wel and O. C. G. Adan. Moisture in organic coatings - a review. *Progress in Organic Coatings*, 37(1-2):1–14, 1999.

[134] M. de Meijer and H. Militz. Moisture transport in coated wood. part 2: Influence of coating type, film thickness, wood species, temperature and moisture gradient on kinetics of sorption and dimensional change. *Holz Als Roh-und Werkstoff*, 58(6): 467–475, 2001.

[135] O. C. G. Adan. *On the fungal defacement of interior finishes*. Ph.D. Thesis, Eindhoven University of Technology, 1994.

[136] M. de Meijer, K. Thurich, and H. Militz. Comparative study on penetration characteristics of modern wood coatings. *Wood Science and Technology*, 32(5):347–365, 1998.

[137] S. J. F. Erich, L. G. J. ven der Ven, H. P. Huinink, L. Pel, and K. Kopinga. Curing processes in solvent-borne alkyd coatings with different drier combinations. *Journal of Physical Chemistry*, under review, 2006.

[138] S. J. F. Erich, J Laven, L. Pel, H. P. Huinink, and K. Kopinga. Nmr depth profiling of drying alkyd coatings with different catalysts. *Progress in Organic Coatings*, 55 (2):105–111, 2006.

[139] M. de Meijer. Review on the durability of exterior wood coatings with reduced voc-content. *Progress in Organic Coatings*, 43(4):217–225, 2001.

[140] A. J. J. van der Zanden and E. L. J. Goossens. The measurement of the diffusion coefficient and the sorption isotherm of water in paint films. *Chemical Engineering Science*, 58(8):1521–1530, 2003.

[141] G. K. van der Wel, O. C. G. Adan, and E. L. J. Bancken. Towards an ecofriendlier control of fungal growth on coated plasters? *Progress in Organic Coatings*, 36(3): 173–177, 1999.

[142] P. R. Laity, P. M. Glover, J. Godward, P. J. McDonald, and J. N. Hay. Structural studies and diffusion measurements of water-swollen cellophane by nmr imaging. *Cellulose*, 7(3):227–246, 2000.

[143] C. G. Fry and A. C. Lind. Determination of cross-link density in thermoset polymers by use of solid-state h-1-nmr techniques. *Macromolecules*, 21(5):1292–1297, 1988.

[144] T. G. Fox and S. Loshaek. Influence of molecular weight and degree of crosslinking on the specific volume and glass temperature of polymers. *Journal of Polymer Science*, 15:371–390, 1955.

[145] W. Posthumus. *UV-curable acrylate metal oxide nanocomposite coatings*. Ph.D. Thesis, Technische Universiteit Eindhoven, 2004.

[146] J. Ross. Novel hygienic solutions. *Polymers Paint Colour Journal*, 194(4479):18–20, 2004.

[147] D. L. Schmidt, C. E. Coburn, B. M. Dekoven, G. E. Potter, G. F. Meyers, and D. A. Fischer. Water-based nonstick hydrophobic coatings. *Nature*, 368(6466): 39–41, 1994.

[148] J. Scheerder, N. Visscher, T. Nabuurs, and A. Overbeek. Novel, water-based fluorinated polymers with excellent antigraffiti properties. *Journal of Coatings Technology*, 2(8):617–625, 2005.

[149] W. H. Ming, J. Laven, and R. van der Linde. Synthesis and surface properties of films based on solventless liquid fluorinated oligoester. *Macromolecules*, 33(18): 6886–6891, 2000.

[150] R. D. van de Grampel, W. Ming, W. J. H. van Gennip, F. van der Velden, J. Laven, J. W. Niemantsverdriet, and R. van der Linde. Thermally cured low surface-tension epoxy films. *Polymer*, 46(23):10531–10537, 2005.

[151] X. S. Hu, W. H. Zhang, M. Y. Si, M. Gelfer, B. Hsiao, M. Rafailovich, J. Sokolov, V. Zaitsev, and S. Schwarz. Dynamics of polymers in organosilicate nanocomposites. *Macromolecules*, 36(3):823–829, 2003.

Summary

Over the last decades, the concern regarding the effect of chemicals on the environment has increased considerably. Nowadays, technological developments in the coating industry are largely influenced by environmental issues and subsequent legislation. One of these issues is the restricted use of Volatile Organic Compounds (VOC) in coatings. Another example is the tendency to replace cobalt as a catalyst used in alkyd coatings by more environmental friendly alternatives, because studies have indicated possible carcinogenicity. As a result alternative catalyst are investigated, based on manganese or iron. The coating industry is a dynamic industry striving for environmental friendly coatings, while increasing the performance and durability of their products and decreasing the development time and costs. To produce high quality products, fundamental knowledge of the many interactions between coating ingredients is required.

In many of these products inhomogeneities exist, both during and after the drying process. However, most standard testing techniques lack the ability to asses these inhomogeneities, because they essentially measure bulk properties. Some techniques can obtain spatial information, e.g., confocal Raman microscopy (CRM), but these techniques are limited to optically transparent coatings. Fortunately, a new NMR setup has been developed that can probe the drying process of a coating (typically 100 μm) with a spatial resolution of approximately 5 μm as function of depth.

This thesis focusses on the chemical drying process (curing) of alkyd coatings, which has been investigated using this high resolution NMR imaging setup. Next to NMR imaging, and additional techniques, like CRM, differential scanning calorimetry (DSC), and mass measurements were used to distinguish the two different drying stages of alkyd coatings: evaporation and curing. The NMR profiles were compared with the disappearance of the double bonds of the unsaturated fatty acids observed with CRM. The results indicated that the disappearance of the double bonds in the fatty acid side chains of the alkyd molecules is directly connected with the formation of cross-links by these fatty acid entities. This oxidative cross-linking results in an increase of the viscosity and therefore in a faster decay of the NMR signal. As a result the curing becomes visible in the NMR profiles.

The curing of alkyd coatings with a cobalt based catalyst was found to be limited by diffusion of oxygen. This oxygen diffusion limitation results in a cross-linked layer (a skin), located on top of a still uncross-linked layer of the coating. At the interface of these two layers cross-linking takes place. The movement of this cross-linking front was modelled, resulting in an equation describing the observed $\sqrt{t}$ behavior of the front position. In solvent-borne alkyd coatings we found an additional effect, i.e., part of the NMR signal from the deeper layer below the cross-linking front decreases during the curing process.

This behavior was explained by diffusion of a low amount of reactive species generated at the location of the front into deeper layers, where they subsequently react. The resulting cross-linking gives rise to a decrease of the NMR signal. This process was described with a model, which predicts that the signal below the cross-linking front decreases proportional to $\sqrt{t}/L$. Subsequent measurements confirmed this prediction.

In our experiments the speed of the observed cross-linking front was found to depend on the catalyst concentration, and addition of secondary driers (Ca/Zr). The observed behavior can only be explained in terms of changes of the variables of the equation describing the front movement. These variables are diffusion of oxygen, oxygen solubility at the surface of the coating, and the amount of oxygen required to cross-link a specific coating volume.

Manganese is proposed as an alternative for cobalt, which is the most commonly used catalyst in commercial alkyd paints. In our experiments oxygen diffusion limitation and the resulting skin layer were only found for coatings with cobalt as a catalyst. When manganese was used a more homogeneous and faster curing behavior was observed. A reaction-diffusion model combined with equations describing the NMR signal as a function of the degree of cross-linking was used to simulate the observed behavior. The results show that manganese has a lower reaction constant and the cross-linked system has a higher diffusion constant for oxygen.

Also the effect of substrates on the curing of alkyd coatings was investigated. With NMR the curing reactions could be visualized, on or even inside a substrate. The front speed was found to be higher when the alkyd emulsion was applied on a gypsum substrate. This increased front speed might be attributed to the presence of Ca^{2+} in the coating functioning as a secondary drier. The Ca^{2+} is transported from the gypsum substrate to the coating during the evaporation stage. From the NMR profiles also the depth of penetration is visible, which allows the adhesion properties to be related to the penetration of the porous substrate.

Possible new application areas of high resolution NMR imaging were explored. One application area is probing the barrier properties of the coating. The NMR setup allows the water content to be measured as a function of position, even on a porous substrate like gypsum. Another application area is probing network properties as a function of position. Preliminary results show that the glass transition temperature can be determined as a function of position. The last application concerns the detection of fluorine, that is added to some coatings to reduce the adherence of all kinds of contaminants. We have demonstrated that with our NMR equipment the distribution of fluorine inside a coating can be determined, even for fluorine concentrations as low as 1.0 %.

Samenvatting

Gedurende de laatste decennia zijn de effecten van chemicaliën op het milieu steeds duidelijker geworden. De technologische ontwikkelingen op het gebied van coatings worden als gevolg hiervan sterk beïnvloed door deze milieueffecten en de strenger wordende regelgeving. Een voorbeeld hiervan is de strenge regelgeving omtrent het gebruik van organische oplosmiddelen in verf. Een ander voorbeeld is het gebruik van kobalt als katalysator in alkyd coatings. Recente studies hebben laten zien dat kobalt kankerverwekkend kan zijn. Vanwege dit feit worden alternatieven gezocht, zoals mangaan of ijzer. De coating industrie is een dynamische industrie die streeft naar hoogwaardige en milieuvriendelijke coatings, die doorgaans binnen een korte tijd ontwikkeld moeten worden. Om deze hoogwaardige kwaliteit te kunnen bereiken is fundamentele kennis noodzakelijk.

In veel situaties kunnen er in een coating inhomogeneiteiten bestaan, zowel gedurende het drogen alsook na het drogen. Helaas kunnen de meeste standaard meettechnieken niet plaatsopgelost meten, en worden alleen de bulk-eigenschappen bepaald. Enkele optische technieken, zoals confocal Raman microscopie (CRM), kunnen dit wel, maar hebben als nadeel dat alleen optisch transparante coatings bekeken kunnen worden. Met behulp van een nieuw ontwikkelde NMR opstelling kan deze beperking worden opgeheven. Met deze NMR opstelling kan een coating (met een typische dikte van 100 μm) met een resolutie van ongeveer 5 μm gemeten worden.

In dit proefschrift komt voornamelijk het chemische uitharden van alkyd coatings aan de orde, dat bestudeerd is met behulp van de bovengenoemde NMR opstelling. Naast deze NMR opstelling hebben wij ook andere technieken gebruikt, zoals CRM, differential scanning calorimetry (DSC) en massametingen, om de twee verschillende droogstadia van alkyd coatings te kunnen onderscheiden. De twee verschillende droogstadia van alkyd coatings bestaan uit het verdampen van het oplosmiddel en het chemische uitharden. De tijdens het droogproces verkregen NMR profielen zijn vergeleken met profielen verkregen met behulp van CRM. Met CRM kan het verdwijnen van de dubbele bindingen in de onverzadigde ketens van alkyd hars gemeten worden. De resultaten laten zien dat het verdwijnen van de dubbele bindingen direct resulteert in het vormen van cross-links. Dit oxidatieve proces zorgt voor een toename in de viscositeit van de coating, wat een sneller NMR signaalverval tot gevolg heeft. Het snelle signaalverval maakt dat het chemische uithardingsproces zichtbaar is in de NMR profielen.

Het uitharden van alkyd coatings met het veelgebruikte kobalt als katalysator is een proces dat gelimiteerd wordt door diffusie van zuurstof. Deze zuurstof limitering zorgt ervoor dat een dunne harde laag aan de bovenkant van de coating gevormd wordt. Onder deze laag is nog steeds onuitgeharde coating aanwezig. Op het grensvlak van deze twee lagen vind het proces van cross-linking plaats. Dit grensvlak, het cross-linking front,

verplaatst over een afstand evenredig met $\sqrt{t}$. Een fysisch model van het zojuist beschreven proces bevestigt deze observatie. Naast dit effect blijkt er in alkyd coatings met en organisch oplosmiddel nog een ander effect te zijn. In de dieper gelegen laag, onder het cross-linking front, blijkt het NMR signaal ook af te nemen. Dit effect hebben wij kunnen verklaren aan de hand van diffusie van reactieve stoffen in de diepere lagen. Deze reactieve stoffen worden gevormd op het front, diffunderen naar diepere lagen, en reageren daar alsnog. Het model dat dit proces beschrijft voorspelt een afname van het NMR signaal evenredig met $\sqrt{t}/L$. Additionele experimenten bevestigen deze voorspelling.

In onze experimenten hebben we geobserveerd dat de snelheid waarmee het front zich verplaatst afhankelijk is van de concentratie van de katalysator en het toevoegen van zogenaamde "secondary driers", zoals Ca en Zr. Een verandering van de snelheid van het front kan verklaard worden in termen van de variabelen die de beweging van dit front beschrijven. Deze variabelen zijn de zuurstofdiffusie door de uitgeharde toplaag, de zuurstofoplosbaarheid aan de bovenkant van de coating, en de hoeveelheid zuurstof die nodig is om een zeker volume van de coating volledig uit te laten harden.

Vanwege de bovengenoemde problematiek omtrent kobalt, is mangaan onderzocht als mogelijk alternatief. Uit onze experimenten blijkt dat het uitharden homogener verloopt dan wanneer kobalt wordt gebruikt. Een dun uitgehard laagje wordt niet geobserveerd en het uitharden als gehaal verloopt sneller. Met behulp van een reactie-diffusie model, in combinatie met vergelijkingen die het signaalverlies als functie van de graad van uitharding beschrijven, kon het proces beschreven worden. Uit simulaties blijkt dat in geval van mangaan als katalysator de reactieconstante lager is en de diffusie van zuurstof hoger.

Ook het effect van enkele poreuze ondergronden is onderzocht. Met NMR kan het uitharden ook gemeten worden op en zelfs in een poreuze ondergrond. Het cross-linking front blijkt sneller te bewegen als een watergedragen emulsie op gips wordt aangebracht. Dit kan verklaard worden door het feit dat een gedeelte van het in het gips aanwezige calcium als "secondary drier" gaat fungeren, nadat het naar de coating is getransporteerd tijdens het verdampingsproces. Bovendien kan de indringdiepte van een coating die op een poreuze ondergrond is aangebracht duidelijk zichtbaar gemaakt worden.

Tenslotte zijn een aantal andere toepassingsmogelijkheden van de NMR opstelling onderzocht. Een voorbeeld hiervan zijn de barrière eigenschappen van verf. Met de NMR opstelling is het mogelijk het vochtgehalte als een functie van de positie in de coating en in het substraat te bepalen. Een andere mogelijkheid is het onderzoeken van de netwerkeigenschappen van de coating als functie van positie. De resultaten laten zien dat bepaling van de glasovergangstemperatuur als functie van positie in de coating mogelijk is. De laatste toepassing is het meten van fluor in coatings. Fluor wordt in lage concentraties toegepast in coatings om adhesie van allerlei stoffen te voorkomen. We hebben laten zien dat met de NMR opstelling concentraties vanaf 1 % gemeten kunnen worden.

List of publications

- Comparison of NMR and confocal Raman microscopy as coatings research tools
  S.J.F. Erich, J. Laven, L. Pel, H.P. Huinink, and K. Kopinga
  Prog. Org. Coat. 52, 210-216 (2005)

- Dynamics of cross linking fronts in alkyd coatings
  S.J.F. Erich, J. Laven, L. Pel, H.P. Huinink, and K. Kopinga
  Appl. Phys. Lett. 86, 134105 (2005)

- Drying process of alkyd coatings studied using spatial resolving NMR
  S.J.F. Erich, L. Pel, H.P. Huinink, and K. Kopinga
  Conference proceedings of 8th Nürnberg congress, p. 467 (vol. II) (April 2005)

- NMR depth profiling of drying alkyd coatings with different catalysts
  S.J.F. Erich, J. Laven, L. Pel, H.P. Huinink, and K. Kopinga
  Prog. Org. Coat. 55, 105-111 (2006)

- Influence of catalyst type on the curing process and network structure of alkyd coatings
  S.J.F. Erich, J. Laven, L. Pel, H.P. Huinink, and K. Kopinga
  Polymer 47, 1141-1149 (2006)

- Curing processes in solvent-borne alkyd coatings with different drier combinations
  S.J.F. Erich, L.G.J. v.d. Ven, H.P. Huinink, L. Pel, and K. Kopinga
  accepted for publication in *The Journal of Physical Chemistry B (2006)*

Dankwoord

Veel mensen hebben mij geholpen gedurende mijn promotieonderzoek, sommige met raad en andere met daad. Een aantal daarvan zou ik met naam willen bedanken:

Zonder hulp van de mensen van de faculteitswerkplaats was het totstandkomen van mijn NMR opstelling niet gelukt. Frank, Henk, Han, Ginny, en Marius mijn dank hiervoor, ook bedankt dat jullie mij hebben laten werken achter de draaibanken en freesmachines. Bij twijfel over voldoende intelligentie werd zelfs mijn IQ nog eens getoetst.

Niet alleen mechanische onderdelen maar ook electronische onderdelen en software zijn van groot belang voor een NMR opstelling; Bedrijfsgroep BLN, bedankt.

Mijn dank gaat uit naar het kenniscentrum Building and Systems TNO - TU/e, voor de financiele steun van mijn promotie onderzoek en de uitstapjes waarvan een aantal samen met Myriam en Marija (de KCBS AIO commissie) zijn georganiseerd.

Gedurende mijn promotie hebben veel studenten hun bijdrage geleverd aan mijn werk of aan dat van de groep; Jan Kuchel, Paul Janssen, Olaf Janssen, Niels Lammers, Xander Janssen, Damien Daly, Bart Berghmans en Johan Gabriëls, bedankt!

Ik ben ook veel dank verschuldigd aan de mensen van de groep "Materials and interface chemistry" van de faculteit Scheikunde. José Brokken voor de vele discussies met mij en mijn afstudeerder Jan Kuchel. Jos Laven bedankt voor al jouw constructieve opmerkingen en discussies omtrent ons gezamenlijke werk, jouw hulp bij de confocal Raman metingen en de inwijding in de coatingtechnologie.

Ook de mensen van Akzo wil ik bedanken voor het leveren van samples, hun interesse en discussies. Ook DSM wil ik bedanken voor het leveren van samples en met name de mensen van Neoresins voor een aantal DMTA en GPC metingen.

Collega's van Natuurkunde en BMT, voor de gezellige momenten op het werk in de b-vleugel en ook gedurende allerlei activiteiten, zoals de AIO-etentjes na het werk.

Lourens Rijniers, bedankt voor het optreden als "woordvoerder", opbeurende woorden als het eventjes niet meezat, voor de IDOLS avondjes en nog veel meer!

Henk Huinink, bedankt voor alle nuttige discussies die wij gehad hebben en het zetten van vraagtekens bij iedere zin.

Hoewel jouw wijze van begeleiding uiterst onconventioneel is, en jouw ongekuiste mening wel eens tot wat "bijzondere situaties" heeft geleijd, was het uiterst leerzaam, Leo bedankt.

Beste Klaas, bedankt voor al jouw hulp gedurende mijn promotie, o.a. met het rood kleuren van mijn proefschrift en het relativeren van allerhande situaties.

Een groot deel van onderzoek moet de aandacht trekken alsook gepromoot worden, Olaf Adan heeft hierin een groot aandeel gehad. Olaf, bedankt!

Jef (Helmonder! Sorry, ik kon het weer niet laten.) en Hans, bedankt voor al jullie hulp gedurende mijn promotie. Ria, bedankt voor al het administratieve werk.

Verder wil ik mijn ouders en mijn zus bedanken voor hun steun. Mijn ouders met name gedurende mijn promotie als ik weer eens gezellig langskwam om bij te kletsen rond etenstijd. Noortje, bedankt voor het ontwerpen van de omslag van dit proefschrift.

Naast werk is ontspanning erg belangrijk. In mijn geval, waren de handbalwedstrijden die John en ik door heel Nederland gefloten hebben een welkome afwisseling. John, bedankt dat ik zo nu en dan eens eventjes kon uitblazen. Pim, bedankt voor jouw hulp en het invallen als ik door het promoveren niet in staat was om als trainer (of als coach) van het MB-1 team op te treden. Verder wil ik ESMG Quadrivium en met name de leden van Sambuca bedanken voor de gezellige momenten tijdens en na repetities, optredens, en andere activiteiten.

Curriculum vitae

Bart Erich werd geboren op 26 februari 1978 te Best. In 1996 haalde hij het VWO diploma aan het Heerbeeck College te Best. In dat zelfde jaar startte hij met zijn opleiding Technische Natuurkunde aan de Technische Universiteit Eindhoven. In het derde jaar van deze studie begon hij ook aan de Technische Universitaire Leraren Opleiding (TULO). Tijdens de externe stage bij Philips Medical systems op het Professor Holst Centrum for Training and Education, werkte hij mee aan het project "Distance Learning". Dit opleidingscentrum voor service engineers van Philips voor service aan MRI en Röntgen apparaten moest opleidingen mogelijk maken op alle locaties wereldwijd via multimedia toepassingen. Vanaf februari 2001 tot aan het einde van datzelfde schooljaar is hij als docent natuurkunde gaan vervangen in de onderbouw van het voortgezet onderwijs. Tijdens het laatste jaar van zijn studie heeft hij een Magnetic Resonance Imaging opstelling ten behoeve van onderzoek aan poreuze materialen gebouwd. Begin 2002 voltooide hij deze opstelling, evenals de vijfjarige opleiding Technische Natuurkunde en de opleiding tot eerstegraads docent Natuurkunde. Vervolgens heeft hij in de vakgroep Transport in Permeabele Media als promovendus gewerkt aan het in dit proefschrift beschreven onderzoek.